



Universidad de Navarra

Facultad de Ciencias

Large scales in a turbulent von Kármán swirling flow

Miguel López-Caballero



Universidad de Navarra
School of Science

Large scales in a turbulent von Kármán swirling flow

Submitted by **Miguel López-Caballero** in partial fulfillment of the requirements for the Doctoral Degree of the University of Navarra

This dissertation has been written under my supervision in the Doctoral Program in Complex Systems, and I approve its submission to the Defense Committee.

Signed on September 20, 2013

Dr. Javier Burguete Mas

Declaración:

Por la presente yo, **D. Miguel López-Caballero**, declaro que esta tesis es fruto de mi propio trabajo y que en mi conocimiento, no contiene ni material previamente publicado o escrito por otra persona, ni material que sustancialmente haya formado parte de los requerimientos para obtener cualquier otro título en cualquier centro de educación superior, excepto en los lugares del texto en los que se ha hecho referencia explícita a la fuente de la información.

(I hereby declare that this submission is my own work and that, to the best of my knowledge and belief, it contains no material previously published or written by another person nor material which to a substantial extent has been accepted for the award of any other degree of the university or other institute of higher learning, except where due acknowledgment has been made in the text.)

De igual manera, autorizo al Departamento de Física y Matemática Aplicada de la Universidad de Navarra, la distribución de esta tesis y, si procede, de la "fe de erratas" correspondiente por cualquier medio, sin perjuicio de los derechos de propiedad intelectual que me corresponden.

Signed on September 20, 2013

Miguel López-Caballero

© Miguel López-Caballero

Derechos de edición, divulgación y publicación:

© Departamento de Física y Matemática Aplicada, Universidad de Navarra

A mi esposa Ana, por darle alegría a mi vida
A mi familia, por quererme tal como soy.

Acknowledgements

La presente Tesis se genero gracias al esfuerzo de muchas personas, por lo que me gustaría agradecer a todos aquellos que he conocido durante mi estancia y que han ayudado a que este proyecto se concrete, ya sea opinando, leyendo, ayudando, corrigiendo, dando ánimo, etc.

A la Universidad de Navarra por generar el espacio para este trabajo, a la Asociación de Amigos por la beca para realizar esta investigación y a los proyectos de investigación (FIS2008-01126, FIS2011-24642) por dar los fondos para este proyecto.

A todos mis compañeros durante el doctorado, en especial a Moorthi, Josia, José, Manuel, Ana, Celia y LuisFer, por mostrar siempre una buena cara a la hora de llegar a trabajar. Igualmente a todas aquellas personas que he conocido dentro y fuera de la universidad durante estos cuatro años, ya que han ayudado a sentirme bajo un ambiente agradable.

A los profesores e investigadores del Departamento de Física y Matemática que tuvieron la amabilidad de generar un buen ambiente.

A mis profesores de la UNAM-Méjico Eduardo y Sergio, que gracias a lo que me enseñaron y su esfuerzo, pude desempeñar un buen trabajo fuera de mi país.

Merci beaucoup to the researchers of the ENS-Lyon Mickael Bourgoin, Romain Volk and Jean Francois Pinton, for give me the oportunity to learn from their experience.

Nire lagunei Piter, Mintxo, Ion eta José, eskerrik asko por toda la ayuda que me ofrecieron estos años y por darme la calidad de vida necesaria para sentirme motivado a querer estar aquí.

Agradecer a Javier Burguete por saber ser un buen tutor y enseñarme que cuando uno trabaja con una buena persona, es imposible que las cosas salgan mal.

Agradecer a mi familia por quererme tal como soy, por aguantar al igual que yo los largos periodos de tiempo sin vernos y principalmente por darme un buen ejemplo de vida.

Quiero agradecer y dedicar muy especialmente este trabajo a mi esposa Ana, ya que sin el cariño y el ejemplo de esta gran mujer, hubiera sido imposible terminar este trabajo.

Contents

Preface	xii
Glossary	xiii
1 Introduction	1
2 Small review of a large heritage	3
2.1 Fluid Dynamics	4
2.1.1 Navier-Stokes equations	5
2.2 Turbulence	7
2.2.1 Taylor hypothesis for closed flows	11
2.2.2 Large Scales – Coherent Structures	12
2.2.3 Inverse Cascades	13
2.3 Von Kármán swirling flows	14
2.3.1 Counter-rotation case	15
3 Experimental Setup and Data Acquisition Techniques	17
3.1 Experimental Setup	18
3.1.1 Cavity	19
3.1.2 Impellers	20
3.1.3 Motors	22
3.1.4 Computer control	23
3.2 Measurement devices	23
3.2.1 Image acquisition	23
3.2.2 Laser Doppler Velocimetry	24
3.2.3 Particle Image Velocimetry	28
3.3 System Features	33
3.3.1 Geometrical features	33
3.3.2 Working fluid	34
3.3.3 Control parameter	34
4 Mean Flow Characteristics	35
4.1 Mean flow, a bistable regime	36
4.1.1 Characterization of the N,S states	37
4.1.2 Comparison with other results	39
4.1.3 Discussion about the position of the shear layer	40

4.2	Inertial and viscous forces independence on the Re number	40
4.3	Modifying the experimental configuration: Mean-flow consequences	44
4.3.1	Velocity profiles	45
5	Description of the turbulence characteristics	47
5.1	Description of the turbulence characteristics	48
5.1.1	Experimental turbulent parameters	49
5.1.2	Spatial distribution of the energy dissipation	52
5.1.3	Intermittency: Does Kolomogorov need to be corrected?	53
5.1.4	Anisotropic and inhomogeneous flow	54
6	Relevant slow time scales	57
6.1	The whole picture	58
6.2	Reversals (-2 slope)	58
6.2.1	Reversal escape time as a function of Re	59
6.3	Equatorial vortices instability	60
6.4	Inverse cascade	62
6.4.1	Cospectrum of the torque	64
6.4.2	Spatial inverse cascade	65
6.5	The angular momentum as a conserved magnitude	67
6.6	Dimensional analysis	69
6.7	Large scale structures at the slow scales	71
6.8	Inertia and impeller stability	71
7	Lagrangian Particle	75
7.1	Slow dynamics	76
7.1.1	Escape times and preferential times	78
7.1.2	Propeller position independence	81
7.2	Stochastic behavior	82
	Conclusions and Outlook	87
	Bibliography	91
	Summary	97
	Resumen	98

Preface

La turbulencia es un fenómeno que aparece en un sinfín de aplicaciones y procesos naturales, por lo que su completo entendimiento mejoraría de manera incalculable la eficacia en la utilización de la energía. Esta es la principal motivación en la realización de este trabajo, ya que el problema energético –que es considerado como un problema de prioridad mundial– necesita del trabajo conjunto de muchas áreas y esperamos que este trabajo pueda contribuir en esa dirección.

El objetivo de esta tesis es estudiar la interacción de la *Turbulencia* y los movimientos lento (grandes escalas) que se producen debido a este fenómeno. En esta investigación nos hemos planteado explicar si no las causas, por lo menos identificar los tipos de procesos que corresponden a las frecuencias lentas y escalas grandes que aparecen en la evolución del flujo considerado. Ya desde hace algunos años se había detectado la importancia de este tipo de movimientos en configuraciones similares, pero sólo desde hace poco se ha tenido total certeza de su existencia. Por otra parte hemos centrado nuestra atención en caracterizar este flujo turbulento, con el objetivo de seguir aportando información para completar una sólida base sobre la fenomenología que aparece en este tipo de flujos en las escalas pequeñas y evoluciones temporales rápidas.

Para esto hemos utilizado un sistema experimental cerrado, capaz de mantener estables los parámetros de control del sistema. Con el objetivo de minimizar las fuentes de fluctuaciones ajenas al experimento, el sistema que se utilizó fue manufacturado con maquinaria de control numérico, logrando que las simetrías del sistema se conserven en un alto grado. Para poder estudiar estos movimientos, hemos utilizado equipos de velocimetría no invasivos, basados en técnicas ópticas como la PIV (velocimetría por imágenes de partículas) y LDV (velocimetría láser Doppler). Ambas se basan en medir la velocidad de partículas imbuidas en el seno del fluido iluminadas con fuentes láser, y actualmente constituyen las herramientas más comunes para estudiar fluidos transparentes en movimiento. El análisis de los datos fue hecho casi en su totalidad mediante rutinas escritas en el lenguaje de programación de MatLab, algunas de estas escritas en nuestro laboratorio y otras de acceso libre desarrolladas por otros grupos de investigadores.

Se ha comenzado este escrito dando una breve introducción sobre lo que es la turbulencia, su historia y cuáles fueron los puntos álgidos sobre su investigación. En esta breve descripción igualmente se aborda el tipo de dispositivo experimental y sistema de medición utilizado. En el capítulo dos, se ha intentado dar una base teórica sobre la evolución de la turbulencia, ademas se incluye un resumen de la historia sobre el equipo experimental utilizado, así como los conceptos necesarios para entender este trabajo. También se describen brevemente las ecuaciones necesarias tanto para entender el movimiento de un fluido, como para su análisis y por último se dan ejemplos de por qué se estudian estructuras coherentes y cascadas inversas. En el capítulo tres, se da una descripción detallada de los elementos mecánicos que componen el dispositivo experimental, así como un explicación de su funcionamiento. Igualmente se hace una revisión de todos los sistemas electrónicos involucrados, tanto para el funcionamiento del equipo como para su estudio. Se incluye de igual manera la descripción de las técnicas de medición utilizadas y se da una base

teórica de su funcionamiento. En el capítulo cuatro, describimos detalladamente el flujo medio encontrado en este dispositivo, se explican incluso las diferencias y similitudes con los flujos medios reportados en otros equipos y finalmente se intenta dar una explicación de por qué encontramos este tipo de flujos, evidenciando que es posible reproducir el flujo medio previamente reportado. En el capítulo cinco, se da una caracterización de los parámetros de la turbulencia para un flujo turbulento cerrado, aportando diversas mediciones que confirman las escalas que describen este flujo. En el capítulo seis, se discuten explícitamente cada una de las escalas lentas que aparecen en este sistema y se ofrecen evidencias cuantitativas, para dar validez a la principal conclusión de este trabajo. Igualmente se ofrece una explicación teórica , basada en la fenomenología observada en esta investigación, dándole aún mas peso a la conclusión final. En el capítulo final, se muestra la investigación realizada del seguimiento Lagrangiano para partículas de diferentes tamaños y se muestran igualmente resultados variando el número de Re .

Glossary

B_p	structure function of order p
C_p	Kolmogorov universal constants
C_D	drag coefficient
D	diameter
\mathbf{D}	distance
E	kinetic energy
\mathcal{E}	kinetic energy
$\hat{G}_j(\boldsymbol{\kappa}, t)$	nonlinear convective term in wavenumber space
H	height
I	image intensity field
\mathcal{I}	moment of inertia
L	characteristic length of the flow
$L_{N,S}$	distance from the propeller to the caps
\mathcal{L}	angular momentum
M_n	statistical moments of order n
N,S	north and south state
$P_{jk}(\boldsymbol{\kappa})$	projection tensor
R	radius of the cylinder
\mathcal{R}	characteristic length of the moment of inertia
R_λ	Taylor-scale Reynolds number
R_{II}	cross-correlation function for two interrogation areas
R_{xx}	longitudinal auto-correlation function
Re	Reynolds number
S	flux of kinetic energy
T	integral time scale
\mathcal{T}	torque
T_0	mean residence time
\mathcal{U}	characteristic velocity scale of the flow
U	velocity variable
\mathbf{U}	mean velocity vector
U^n	fluctuating velocity to the nth
$V_0(\mathbf{X}_i)$	transfer function
V_{prop}	rotation velocity of the propeller
\mathbf{X}	material coordinates
\mathbf{X}_i	first exposure location
a_I	interrogation area
d_p	tracer particle diameter

d	particle image displacement
<i>e</i>	internal energy
e_{pr}	energy emitted from the particle
f_r	frequency detected by the receiver
f	body forces
$f_{N,S}$	rotation frequency of the propeller
f_{prop}	rotation frequency of the propeller
f_{sh}	shifted frequency
l_{int}	integral scale
n_i	refraction index of material
<i>p</i>	pressure
q	heat flux
s	separation vector
t_n	normalized time
t_{int}	time scale of larger eddies
u^n	nth moment of fluctuating velocity
u'	r.m.s. velocity vector
v	Eulerian velocity vector
v_n	normalized velocity
\bar{v}	local advection velocity
$\hat{v}_j(\boldsymbol{\kappa}, t)$	velocity vector in wave number space
v_p	particle velocity
x	position in space
Γ	state of the ensemble
Γ	aspect ratio
Ω_{prop}	rotation injection frequency of the propeller
α	angle
ε	energy transfer rate
ϵ	control parameter
η	Kolmogorov lenght scale
θ	angle
κ	wavenumber
κ	wavenumber vector
κ_{int}	wavenumber that correspond to the integral scale
κ_λ	wavenumber that correspond to the taylor micro scale
λ	taylor micro scale
μ	dynamic viscosity
ν	kinematic viscosity
ξ	noise distribution
ρ	density
τ	time scale
τ_η	Kolmogorov time scale
σ	stress tensor
ψ	stream function

1 Introduction

We may wonder whether the scientific study of fluid flows was started either by its importance or just because of simple curiosity, however what is clear is its importance, as fluid mechanics is involved in a lot of natural processes and even in a great variety of technological applications. One of the earlier discovered characteristics of these flows was the existence of vortices, a fact that can be dated back even to Aristoteles. Their appearance modifies the global behavior of the considered flows, and from this point of view we can classify the flows as laminar and turbulent. Because of its implications, turbulence is currently considered one of the most important subjects in physics and due to its difficulty this subject remains as the last unsolved problem of classical physics.

Turbulence study has used different techniques to address many different questions, some very intuitive like the formation of large structures or more complex like the mechanisms that are in charge of the transfer of kinetic energy among different scales. The first step toward a categorization of these studies is to distinguish between small-scales turbulence and the large-scale motions in turbulent flows [1], since under some restrictions this approach allows to split the analysis and simplify the whole problem.

Over the last decades many groups have studied the inertial range of turbulent flows over a wide range of different configurations, and from these studies it has been possible to obtain a general characterization of the isotropic cases. In 1941 Andrei Kolmogorov[2, 3] gave us a phenomenological picture of the local structure of turbulence assuming an incompressible, homogeneous and isotropic flow. The interpretation of the transfer of energy between different scales until it is finally dissipated was a big step in the understanding of turbulent flows. These behavior can be understood through the ensemble average of different statistical magnitudes at different scales, as the second and third structure functions closely related to the corresponding statistical moments.

Kolmogorov not only give us a quantification of the idea of the Richardson cascade, rather, he gave the basic tools to start a whole new theory of turbulent flows, based in the ideas of Richardson, Batchelor, Taylor, Landau, Reynolds, Stokes and many others. However, his work does not solve the whole problem of turbulent flows, the partial failure of Kolmogorov's theory relies in the now called "*intermittency*"[4]. According to Landau, this variation in space and time of the dissipation rate depends of the large-scales characteristics, which always depends on the particular characteristics of the considered system. Nowadays researchers are focusing on this and on other types of problems of fully developed turbulent flows, as are the mechanisms that originate these dynamics.

Nevertheless, these studies do not provide any generic interpretation of the formation of large structures in turbulent flows, as tornadoes in the earth or hurricanes in the oceans, these two just to mention a few examples of large scales. As one could imagine the understanding of how these structures are formed, could lead to a plenty of useful applications, such as environmental disaster prevention, energy savings in transportation, a more efficient energy production, the

manufacturing of new materials, and so on. Nowadays certainly exists a wide range of numerical methods, experimental techniques and mathematical tools to face these problems in turbulence. But undoubtedly the experimental method is the most suitable for this branch of physics, since gives real information on how a fluid behaves.

The large number of experimental techniques also implies another choice, as it is the selection of the most suitable technique or techniques to investigate a given problem. We thought that the non invasive velocimetry techniques are the most adequate ones, because such techniques don't alter the flow and give enough spatial and temporal information on the evolution of the flow for the considered range of scales. The research presented here is based on three different classes of experimental techniques. The first one is the LDV technique that is capable to give you a very high temporal resolution of the velocity measurements, but at the cost of a coarse spatial resolution. The second technique is the PIV, that has a poor temporal resolution (for the setup used in this work), but a high spatial resolution compared to the LDV. And finally, the third one consists on qualitative visualizations of the flows using air bubbles, glass spheres or even neutrally buoyant large spheres. The experimental setup used in this work is an evolution of a simpler version where some of the characteristics of the flow were already determined. But based on these previous researches, some new features have been added to the experimental vessel in order to enhance some parameters as the total power injected and the inertia of the system. These improvements have enlarged the set of dynamical behaviors displayed by the system compared to previous results[5].

In this work we have analyzed the new dynamics that appear in a von Kármán flow, related with the existence of very slow time scales and very large spatial dimensions. The mechanisms that produce such large scales could be related with the mechanisms that produce large structures in nature. Our main goal was to understand these dynamics and propose an explanation of the possible mechanism behind these structures. As we will discuss in the following chapters, our interpretation of this behavior relays on the existence of an inverse cascade, i.e. a backwards transfer of angular momentum in the spectral space. Nonetheless there still much work to be done to really understand how the interaction of different elements of fluid are capable of generate this large scale dynamics.

2 Small review of a large heritage

Resumen

En este capítulo se repasan algunos conceptos generales que son necesarios para entender el comportamiento de los líquidos en movimiento. Para esto recurriremos a definiciones clásicas que aparecen en la literatura de la dinámica de fluidos y de la turbulencia. Una mejor descripción de este marco teórico se puede encontrar en las referencias citadas en este breve resumen. Esperamos facilitar una rápida revisión de las ideas fundamentales y con ello presentar algunos conceptos de la teoría que describe los flujos turbulentos totalmente desarrollados. Pretendemos también describir cualitativamente desde un punto de vista fenomenológico las estructuras coherentes y por último hablar sobre la existencia de mecanismos para transferir energía hacia las escalas grandes (cascada inversa) en el espacio de Fourier. También incluimos una revisión sobre configuraciones de sistemas experimentales similares al usado en este trabajo.

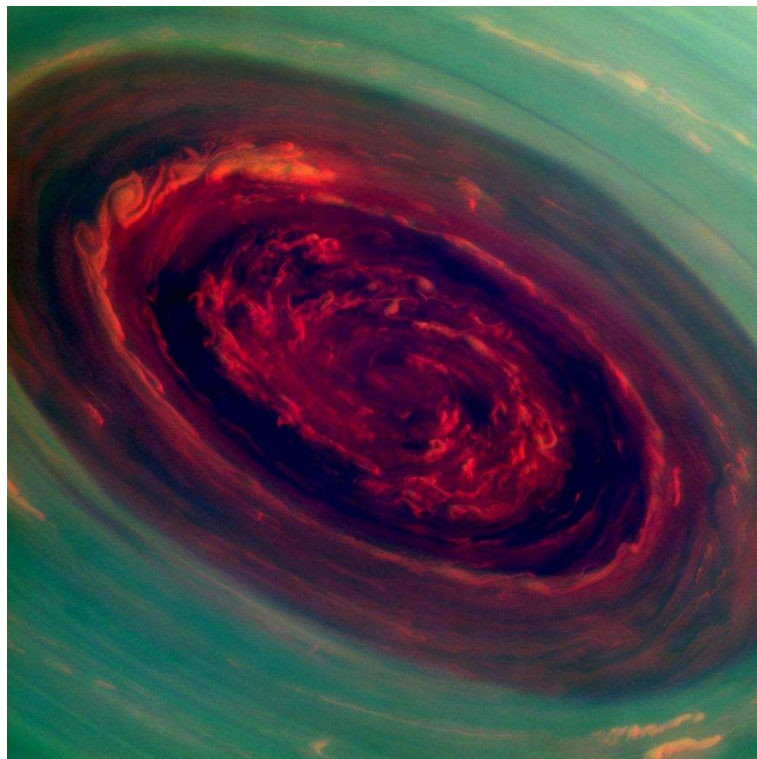


Figure 2.1: Large storm at the North pole of Saturn (Picture taken by NASA¹).

Abstract

In this chapter we will revise some general concepts that are necessary to understand the behavior of fluids in motion, evoking a few classical definitions that appear in the literature of fluid dynamics and turbulence. A deeper description of this background can be found in the references cited in this brief review. We expect to give a quick conceptual revision of fluid dynamics and thereby present some concepts of the theory that describes the fully developed turbulent flows. As well, we will introduce the phenomenological picture of coherent structures and finally talk about the existence of mechanisms able to transfer energy backwards (inverse cascade) in the Fourier space. Also, we include a summary about the different experimental configurations that have been analyzed by other groups, and that are closely related to the one used in this research.

2.1 Fluid Dynamics

From early times mankind had the hope to understand the motion of fluids, perhaps due to the importance of its applications or maybe for simple curiosity. Whatever is the reason, this has led to numerous efforts of different people to explain some questions about the dynamics of fluids. The first written observation was left by the Greeks: Aristoteles (384-322 a.c.) left two crucial ideas, one is the perception of the idea of continuum² and the second was the verification that an object moving on a fluid experiences a resistance to its displacement. These concepts were developed over the following centuries thanks to a lot of people involved in the evolution of fluid mechanics, a good historical resume can be found in this reference[6].

Nowadays, the continuous media concept constitutes the starting point for the present point of view of fluid dynamics. Under this assumption, the constitutive equations for fluid dynamics were derived. The peculiar characteristic of such equations is the advective term ($\mathbf{v} \cdot \nabla$) that translates the fact that a fluid can transport different magnitudes, as the temperature or the internal energy. This term has a great practical importance, since we know that fluids are in charge of descriptions like the thermal processes of the atmosphere, the pollutant concentration in the air, mixing of different substance, etc., and basically this attribute is what characterizes fluids.

The evolution of those physical properties can be described using two different approaches: the *Eulerian* and *Lagrangian* point of views[7, 8]. In the Eulerian reference framework the physical properties as the velocities, pressure, density, etc., will be expressed by a *spatial description* and will be functions of the position in space (\mathbf{x}) and time (t) referred to a fixed position, the laboratory reference frame. Instead, in the Lagrangian point of view the physical properties of an element of fluid are expressed in terms of the material coordinates (\mathbf{X}) and time (t) that follow the fluid elements, so we can say that such properties are given by the *referential* or *material description*. Knowing this, a set of conservation equations of mass, momentum and energy, were

²The continuous may be defined as something that is divisible into parts which are themselves divisible to infinity, as a body that can be divided in small parts in all directions. When this division can be applied in only one direction, the magnitude is continuous along a line, when they can be divided in three directions it is continuous in a volume. Magnitudes that are divisible in this way are continuous. Aristotle (384-322 a.c.)

derived for a Lagrangian coordinate system, nevertheless this equations needs to be reinterpreted in the Eulerian system, and the Reynolds' transport theorem allows us to do this[9]. However, those equations will be solved in most of the cases in the Eulerian reference frame.

The set of equations that describe the behavior of a fluid are the conservation of three magnitudes, Mass:

$$\frac{\partial \rho}{\partial t} + \nabla \cdot (\rho \mathbf{v}) = 0 \quad (2.1)$$

Energy:

$$\rho \frac{\partial e}{\partial t} + (\mathbf{v} \cdot \nabla) \rho e = (\boldsymbol{\sigma} \cdot \nabla) \mathbf{v} - \nabla \cdot \mathbf{q} \quad (2.2)$$

and Linear Momentum:

$$\frac{\partial \mathbf{v}}{\partial t} + (\mathbf{v} \cdot \nabla) \mathbf{v} = \frac{1}{\rho} (\nabla \cdot \boldsymbol{\sigma}) + \mathbf{f} \quad (2.3)$$

This set of equations plus two equations of state configures the so-called constitutive equations. They have a total of seventeen unknowns which are the density(ρ), the internal energy(e), the velocity(\mathbf{v}), the heat flux(\mathbf{q}) and the stress tensor($\boldsymbol{\sigma}$). These set of equation lack of an analytic solution, so it is currently impossible to predict the behavior of a fluid element.

2.1.1 Navier-Stokes equations

Two parameters of the constitutive equations, as the density and the viscosity, depend on other physical magnitudes, as pressure and temperature. This may have an important impact in the description on the fluid flows, but for a lot of applications these two parameters can be considered constants – Newtonian fluid³. This simplification of the equation that governs the fluid motion was proposed independently by Claude Louis Marie Henri Navier (1785-1836) and George Gabriel Stokes (1819-1903)[6].

Subsequently the Navier-Stokes equations[9] for an incompressible fluid of constant dynamic viscosity and density becomes

$$\frac{\partial \mathbf{v}}{\partial t} + (\mathbf{v} \cdot \nabla) \mathbf{v} = -\frac{1}{\rho} \nabla p + \nu \nabla^2 \mathbf{v} + \mathbf{f} \quad (2.4)$$

This equation basically represents the Newton's second law for a fluid element with constant density. Here \mathbf{f} (body force term) represents the external forces; in our case this term correspond to the forces that the impellers exerts over the fluid, \mathbf{v} corresponds to the velocity field, p is the pressure and ν the kinematic viscosity. The difficulty to solve analytically problems in fluid dynamics arise from the non-linearity in the $(\mathbf{v} \cdot \nabla) \mathbf{v}$ advective term and is for that reason that often the behavior of the fluids must be determined experimentally. This non-linear term where the velocity is quadratic makes the determination of the acceleration of a fluid element a tangled issue.

³The stress is directly proportional to the velocity gradient –a fluid with constant viscosity-[7].

To summarize, the physical laws that govern the behavior of the incompressible fluid elements can be condensed into the Navier-Stokes eqn (2.4) plus the continuity equation (2.1) that in this case takes the form:

$$\nabla \cdot \mathbf{v} = 0 \quad (2.5)$$

This pair of equations has an equal number of unknowns and equations, satisfying the basic laws of mechanics. A good description of this pair of equations can be found in [9, 10]. However, this approximation does not solve many of the practical applications that have the fluids in motion. Actually, nowadays only exist a few exact solutions of these equations, in where some are trivial (non-linear terms vanish) and others (with the non-linear terms) are simplified using some symmetry or similarity [11]. According with Uriel Frisch, maybe these equations contains everything to understand turbulent flows, “*yet it would be foolish to try to guess what its consequences are without looking at the experimental facts*”(Frisch[12].., 1995:1).

However the difficulties, there are some conclusions that can be extracted from these equations. Using the Fourier analysis, we can translate these equations onto the reciprocal space, in order to decompose the flow field into various length scales. The time derivative, the pressure term and the dissipative term, can be easily transposed in the Fourier space, nonetheless, for the nonlinear convective term the situation is more complex.

In Fourier space the Navier-Stokes terms are, the time derivative

$$\frac{\partial \mathbf{v}}{\partial t} \rightarrow \frac{d}{dt} \hat{v}_j(\boldsymbol{\kappa}, t), \quad (2.6)$$

the dissipation term

$$\nu \nabla^2 \mathbf{v} \rightarrow \nu \kappa^2 \hat{v}_j(\boldsymbol{\kappa}, t), \quad (2.7)$$

the pressure-gradient term

$$-\frac{1}{\rho} \nabla p \rightarrow -i \kappa_j \hat{p}, \quad (2.8)$$

and the nonlinear advective term

$$(\mathbf{v} \cdot \nabla) \mathbf{v} \rightarrow \hat{G}_j(\boldsymbol{\kappa}, t). \quad (2.9)$$

However, the pressure term can be eliminated using the incompressibility assumption and evoking the Poisson equation

$$\kappa^2 \hat{p} = i \kappa_j \hat{G}_j, \quad (2.10)$$

this relation couples the nonlinear term with the pressure term. This coupling permits the interaction between different modes in the wave number space, allowing the conservation of the nonlinear energy transfer between the modes, that is very useful for the interpretation of turbulence. Finally the Navier-Stokes equations (2.4 and 2.5) can be interpreted in the Fourier space as[1, 13]:

$$\frac{d}{dt} \hat{v}_j(\boldsymbol{\kappa}, t) + \nu \kappa^2 \hat{v}_j(\boldsymbol{\kappa}, t) = -i \kappa_l P_{jk}(\boldsymbol{\kappa}) \sum_{\boldsymbol{\kappa}'} \hat{v}_k(\boldsymbol{\kappa}', t) \hat{v}_l(\boldsymbol{\kappa} - \boldsymbol{\kappa}', t) \quad (2.11)$$

$$\boldsymbol{\kappa} \cdot \hat{v} = 0 \quad (2.12)$$

2.2 Turbulence

To talk about turbulence and its history, it is to invoke the work of many people during the past centuries (Reynolds, Prandtl, Kármán, Taylor, Richardson, Kolmogorov, Kraichnan, etc.). To cover all their contributions would be an impossible task, and so we would like to point out that there are many very good historical reviews of this evolution, as for example in [14]. This theoretical background was based on [1, 4, 12, 15, 16], and a more precisely information could be found in these books.

However we would like to present here the milestones of this development. The experimental work of Osborne Reynolds [17] can be denoted as the starting point of the modern approach to turbulence. He gave the basic idea of what the turbulence phenomenon is. He introduced the key idea of a direct competition between inertia and viscosity, in where this relation later became the famous *Reynolds number* (eqn 2.13) –a note about this dimensionless number can be found in [18] –.

$$Re = \frac{\mathcal{U}L}{\nu} \quad (2.13)$$

Nowadays, this parameter is commonly used to distinguish between a *laminar flow* and a *turbulent flow*. These regimes will depend on the forces that dominate the flow; for the case in where the viscosity dominates, the flow will remain in the laminar case, respectively when the inertia dominates, the flow will be in the turbulent regime. A good approach to understand what turbulence is and what are their building blocks, are the books of Van Dyke[19] and Samimy et al. [20]. Especially the book of Van Dyke, shows the experimental observations about what turbulence and transition to turbulence is –in Fig.2.2 we can seen an example of the transition from laminar to a turbulent flow–. Basically, a fluid flow will remain in the laminar case until an instability appears becoming spatio-temporally unstable its solution, the new solution reached, is where many magnitudes are time-dependent and only their statistical values can be considered stables. But according to Tsinober[21], to provide a definition of what is turbulence with the actual information, wouldn't be enough to clarify this concept and it is why many researchers began describing the characteristics of turbulence instead a definition.

The complex nature of the properties of turbulence lies in the fact that similar results describe different turbulent flows. Nevertheless, in those systems a common point is that the statistical properties of the flows shed the same values, and under this perspective the scientists have been using statistical tools to aboard the description of such quantities. A powerful tool to analyze the evolution of a zero-mean evolving variable U (as, for example, the velocity fluctuations) in turbulence is to evaluate its statistical moments defined as [1]

$$M_n \equiv \langle u^n \rangle = \int_{-\infty}^{\infty} U^n f(V) dV, \quad (2.14)$$

where $f(V)$ is the probability density function (PDF) of this variable U . The analysis of these moments will characterize, for example, the shape and asymmetry of different probability density functions, and can be easily extended to the analysis of correlations between different spatial points. This later analysis could determine if different samples are correlated or uncorrelated.

As have said before, the extensive range of scales that appear in turbulent flows and its interactions, comes from the non-linearity of the problem. These interactions show organized

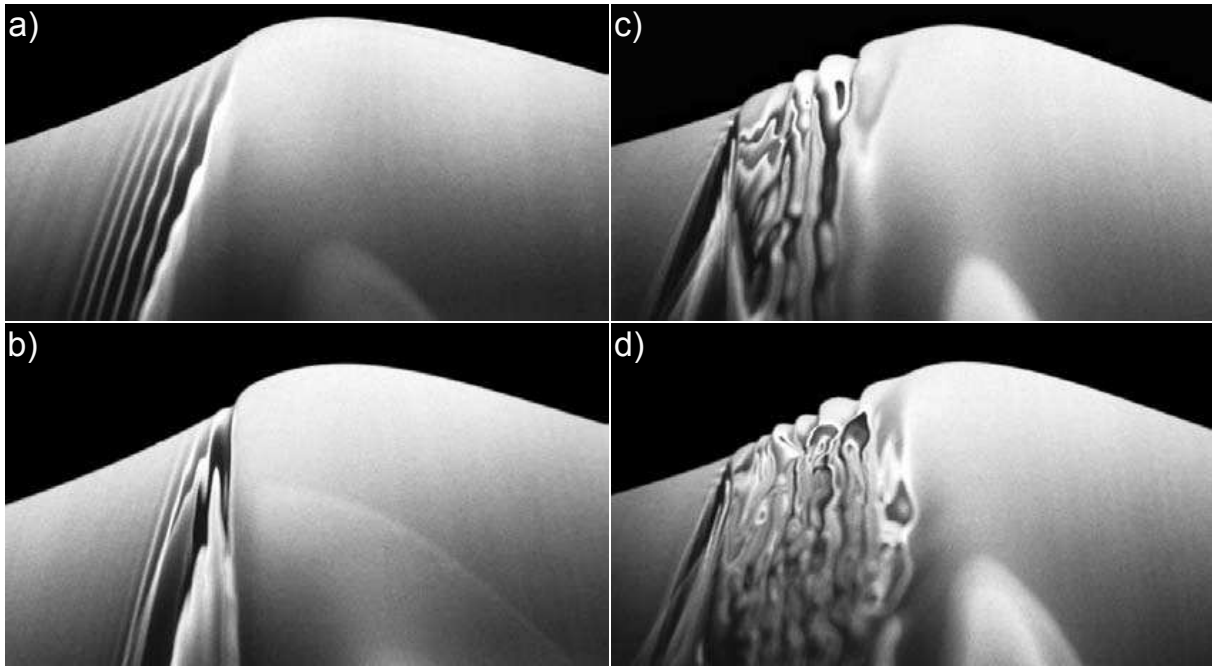


Figure 2.2: Unsteady spilling breaking water wave as example of transition from a laminar to a turbulent flow [20].

structures giving it more weight to the statistical description. The most famous definition – derived from a remix of ideas– of the physical mechanism of this scales interaction was given by Richardson, in his now known phrase:

"Big whirls have little whirls, that feed on their velocity, and little whirls have lesser whirls and so on to viscosity –in the molecular sense" (Richardson[22], 1922:66).

This qualitative idea of the mechanism that transfers the kinetic energy from large to smaller eddies, until the viscosity starts to play an important role dissipating its energy, lacked in that time of a proper mathematical interpretation. In order to give a mathematical description of this hierarchy of eddies, G.I. Taylor[23, 24] and many others developed statistical methods and ideas to be used in the turbulence theory. In his work Taylor introduced some basic concepts that nowadays are used to characterize the turbulent flows, he measured the average size of the larger eddies l_{int} using the auto-correlation function

$$l_{int} = \int_0^{\infty} R_{xx}(r) dr \quad (2.15)$$

$$R_{xx}(r) = \frac{\langle u'(x)u'(x+r) \rangle}{\langle u'^2 \rangle} \quad (2.16)$$

and also he gave an implicit measure of the average size of the smallest eddies that could be appear in a turbulent flow. Nowadays it's well known as an intermediate value, between the l_{int} and η and is called the Taylor microscale:

$$\lambda = (15\nu u'^2 / \varepsilon)^{1/2} \quad (2.17)$$

Also, further work gave the now well accepted rate of energy transfer ε from the large eddies into the smaller ones; that scales as

$$\varepsilon = \frac{1}{2} C_D \frac{\mathcal{U}^3}{L} \quad (2.18)$$

and a good derivation of this statement can be seen in [12].

Another parameter that is commonly used nowadays is the “Taylor-scale Reynolds number”(eqn.2.19), this parameter was used by Batchelor[25] in order to explain that the relation showed by Taylor[26] between λ/λ_p varies as $R_\lambda^{1/2}$ and actually is used to characterize the turbulence because it includes a local representation of the ratio between inertial and viscous forces.

$$R_\lambda = \frac{u' \lambda}{\nu} \quad (2.19)$$

In 1941 Kolmogorov [2, 3], using the concept of homogeneous and isotropic turbulence, gave a mathematical interpretation on how the energy injected at large scales is transferred to smaller scales until dissipates due to the viscosity. The basic idea was to introduce the universality assumption⁴ in the theory of turbulence. This assumption restricted the evolution of the statistical magnitudes to only three variables and had many consequences. This formulation introduced by Kolmogorov was the base to estimate some characteristics of the turbulent flows, now known as turbulence parameters or Kolmogorov scales[1], that show the spatial and temporal properties of the smallest eddies:

$$\eta = (\nu^3 / \varepsilon)^{1/4} \quad (2.20)$$

$$\tau_\eta = (\nu / \varepsilon)^{1/2} \quad (2.21)$$

where η is the Kolmogorov length, and is associated to the smallest eddy where the universality assumption can be applied (from that size, the viscosity becomes dominant) and τ_η is the characteristic time for this eddy, related with the turn-over time or the frequency of these smallest eddies.

These scales that characterize the eddies that are in charge of dissipate the energy injected into the system can also be obtained under a dimensional analysis. This universal statistical regime can be assumed for scales greater than the Kolmogorov scale η , but smaller than the scale of the whole flow L (“Inertial subrange”). The range of scales where this postulate applies, i.e. the difference between those scales large and small, can be derived using the dependence on the energy dissipation law in eqn 2.18:

$$\frac{\eta}{l_{int}} = Re^{-3/4} \quad (2.22)$$

$$\frac{\tau_\eta}{t_{int}} = Re^{-1/2} \quad (2.23)$$

⁴**Kolmogorov's first universality assumption.** At very high, but not infinite, Reynolds number, all the small-scale statistical properties are uniquely and universally determined by the length scale l , the mean dissipation rate (per unit mass) ε and the viscosity ν [27].

With these expressions we can see how at high Re the timescale τ_η is small compared with t_{int} , where t_{int} is the time scale of the larger eddies (resp. l_{int} is the length scale for the largest size of the eddies). Respectively, the ratio between the Kolmogorov scale η and the integral scale l_{int} decreases while Re increases. With these relations, we can now say that for the inertial subrange the viscosity ν will be almost negligible, and this regime will be determined only by the energy transfer rate ε and not by the viscosity⁵. A representative picture of these scales can be seen in Fig.2.3.

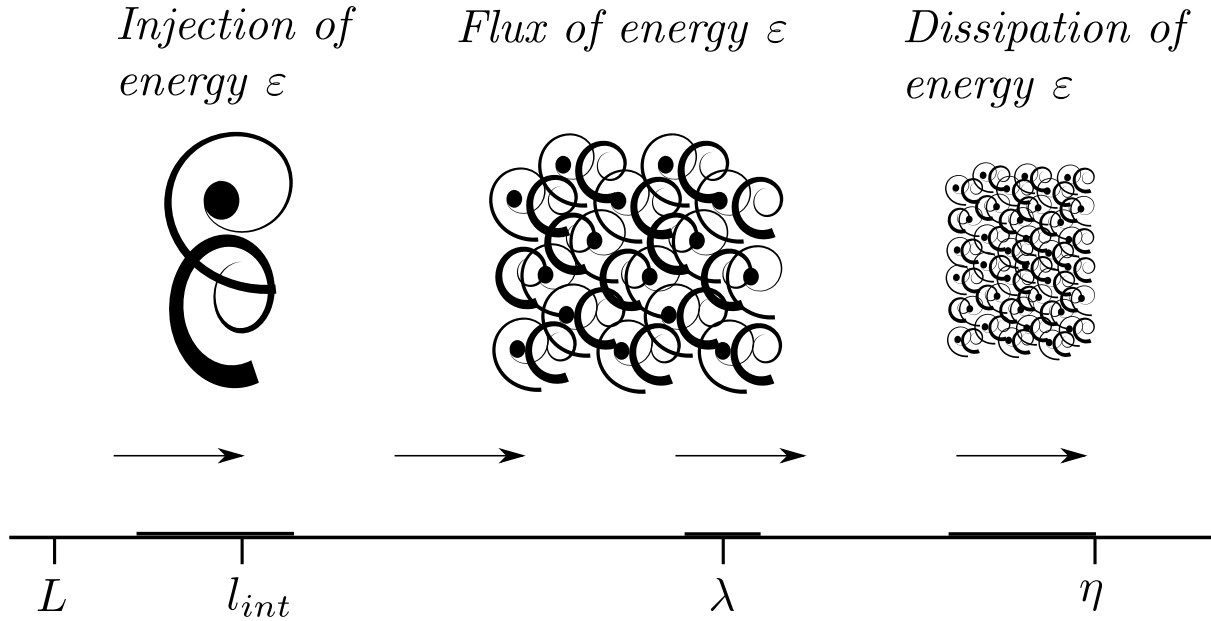


Figure 2.3: Schematic representation of the transfer of the kinetic energy at high Re .

The mathematical interpretation that Kolmogorov gave, considered the second and third moments of the spatial velocity fluctuations in an assumed local isotropic turbulence, plus the average dispersion of energy. Basically, what he considered was the evolution of the velocity on two different points separated a distance r , and obtained their statistical behavior:

$$B_p(r) = \langle [v(x+r) - v(x)]^p \rangle = \int_V [v(x+r) - v(x)]^p dx \quad (2.24)$$

These quantities are known as the velocity structure functions. For an inhomogeneous flow, these magnitudes may have a different behavior depending if they are computed along the mean flow (streamwise) or in a direction perpendicular to that average flow (spanwise).

From this theoretical point of view, he gave us the two most used equations to obtain the turbulence characteristics, the second and third structure functions in the longitudinal direction:

$$B_{dd}(r) = C\varepsilon^{2/3}r^{2/3} \quad (2.25)$$

$$B_{ddd}(r) = -\frac{4}{5}\varepsilon r \quad (2.26)$$

⁵**Kolmogorov's second universality assumption.** In the limit of infinite Reynolds number, all small-scale statistical properties are uniquely and universally determined by the length scale l and the mean dissipation rate ε [27].

In Fourier space, Obukhov[28] deduced the spectral density of the kinetic energy that is transferred along different wave numbers (eqn.2.27), giving it place to the now classical -5/3 power law.

$$E(\kappa) = C_1 \varepsilon^{2/3} \kappa^{-5/3} \quad (2.27)$$

The importance of the behavior of turbulence in Fourier space, is because it is very easy to interpret the conservation of kinetic energy along different wave numbers, or in other words, scales. And, from the second term in the equation 2.11, the dissipation won't take place until the scales are small enough compared with the integral scale.

2.2.1 Taylor hypothesis for closed flows

The transfer of energy for a local isotropic turbulent flow has a direct cascade –in the power spectrum– as $\kappa^{-5/3}$ when in the space domain $\mathbf{v}(t \text{ fixed}, \mathbf{x})$. This can be reinterpreted using the Taylor's hypothesis[23] for the temporal evolution of the velocity in a fixed spatial location $\mathbf{v}(t, \mathbf{x} \text{ fixed})$. But this assumption is only valid when the velocity of the fluid stream in charge of transport the eddies is much larger than the velocity of the turbulent eddies. In other words, the spatial structure of the flow is advected by the mean flow, and the spatial fluctuations become temporal fluctuations.

In our case most of the velocity measurements were done for fixed points, where the data were obtained for long time series. But, as we will see, the average flow considered in this configuration is not stable, but has a slow evolution. Therefore seems that in our case is not possible the direct use of the correspondence between the spatial structure with time measurements ($\mathbf{x} = \mathbf{v}'t$) [24], this can be valid only for regions in where the mean flow is stable. Nevertheless Pinton and Labbé[29] gave a correction to this hypothesis for local regions (local Taylor hypothesis), where they relate the velocity for a time t with a position x by:

$$v(t) \rightarrow v(x) \quad x = \int_0^t \bar{v}(\tau) d\tau \quad (2.28)$$

where \bar{v} is the local average velocity:

$$\bar{v}(\tau) = \frac{1}{T} \int_{\tau-T/2}^{\tau+T/2} v(t) dt \quad (2.29)$$

Basically they preserved the essence of the Taylor assumption, in where the small eddies are advected by the large scales. But in this case they defined the local advection in function of the time scale T , that comes from the rate at which energy is injected. With this, we can now be sure that our inertial range measured in the center of the cylinder could be re-scaled to the space domain and will be useful to determine the energy dissipation rate using LDV. This approach is only valid to scales smaller than the time scale T , so for larger scales does not exist a function that relates these two domains. For our case, the characteristic time for the temporal evolution of the average flow is larger than 1s, so we should take $T < 1s$, and in all the cases where this hypothesis has been used for the LDV series, the maximum time for which the hypothesis was used is around 0.1s.

2.2.2 Large Scales – Coherent Structures

Despite the numerous efforts of the scientists to find an heuristic description of turbulence, it seems that some natural aspects of turbulence remain unsolved. One of those features is the appearance of large (wave number larger than l_{int}) organized clusters of small swirls, with a qualitative periodic behavior. The quantitative way to detect such structures lacks of a methodology in the study of turbulence, however since many years ago flow visualization techniques have become a useful tool to detect such large structures, and many qualitative proofs like the Fig.2.4 have been published.

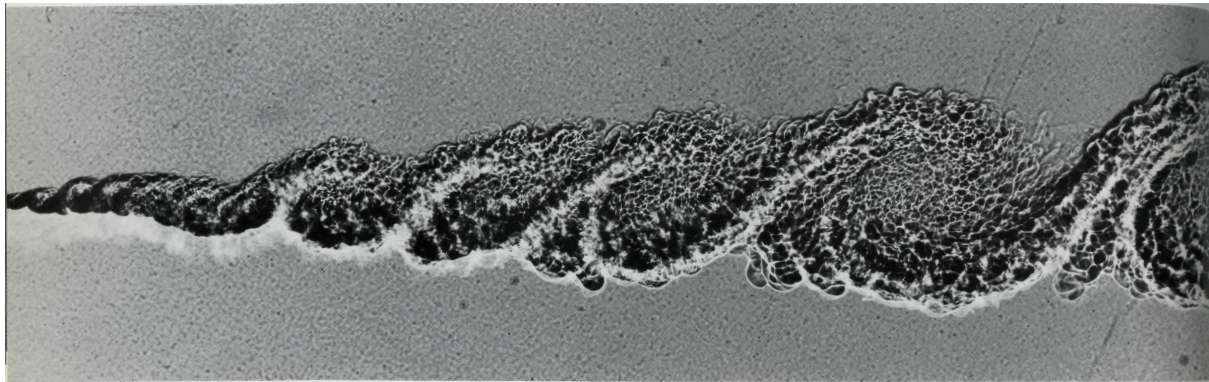


Figure 2.4: Coherent large structure in turbulent mixing layer[30].

Noteworthy that the mere observation of this type of structures using visualization techniques does not give relevant information about its origin, and it is because of this that some people has started to use the dynamical systems framework in order to detect this kind of structures.

The existence of large structures in turbulent flows is well known since the beginning of the study of turbulence. In the past thirty years there has been evidence [31] on how such structures affect the dynamics of the fluctuations at the small scales, with a direct impact on the study of turbulence and also in areas where turbulent flows are present as in magnetohydrodynamics[5]. A better description about this subject can be found in [11, 21].

This work points in this direction: we will provide with some explanations about which can be the mechanisms that originate the large structures in fully developed turbulent flows, and also some tools to reconstruct in a semi-qualitative way such structures. One might wonder why it is important to study these phenomena without a previous knowledge of the mechanisms at small-scales and the answer could be, because the impact of such structures in our daily live has. In geophysics one of the major misunderstood problems are the formation of tornadoes and hurricanes, the influence of such structures in our lives some times has a devastating impact and their understanding could minimize their effects.

Kelvin-Helmholtz Instabilities

One example of large scale structure which has been widely investigated, is the Kelvin-Helmholtz instability(KHI)[10]; this coherent structure appears when a shear velocity arises in a continuum medium. Nonetheless, the origin of this instability has been related to the perturbations at the small-scales that are occurring in the fluid, which in turn obtain kinetic energy from

the mean flow. The theory developed can describe the dynamics of such structures using the Taylor-Goldstein equation for quasi-2D flows and also covers a broad range of characterizations for fluids with different densities and speeds.

The existence of this instability is very common in turbulent shear flows, the most common case is the one that can observe in the atmosphere in which is possible observe the characteristic waves of the KHI. Nevertheless we must distinguish between them, since KHI is a phenomenon theoretically investigated in two dimensions and in laminar flows, and turbulence is a three dimensional phenomenon.

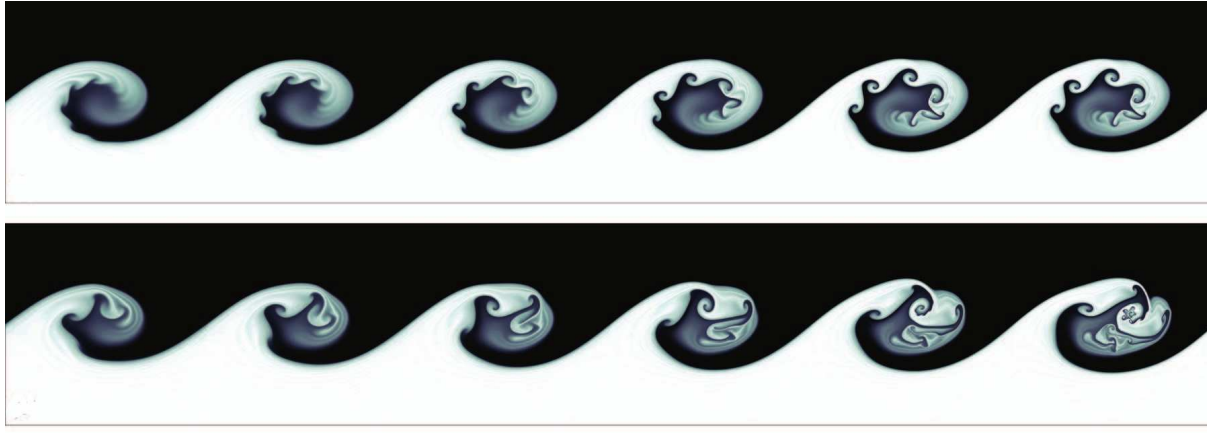


Figure 2.5: Numerical simulations of the Kelvin-Helmholtz instability[32].

2.2.3 Inverse Cascades

Turbulence is present in many aspects in our ordinary life, but in certain cases like weather prediction, attracts much more attention because of its consequences. An important point about the study of weather forecast, it's that this problem can be assumed as quasi 2D, due to the thin stratified layers where the geophysical flows evolve in the atmosphere. A pioneer and ground-breaking work was developed by R.H. Kraichnan in 1967[33] about the existence of two inertial ranges in 2D turbulence. He introduced the concept of the existence a backward energy cascade, in where the inertial range for the kinetic energy go towards the large scales and he obtains a direct inertial range for an enstrophy flux. Further, in the past years the prediction of Kraichnan of the existence of an inverse energy transfer has been validated by numerous works either numerical[34–36] or experimental[37, 38]. The flow structures in charge of the transfer either enstrophy or energy, were reported by C.-H Bruneau et al.[36] and its results are presented in Fig.2.6.

Some specific cases of inverse cascades have been found in different configurations, like in quantum fluids[39], wave turbulence[40–42], thick fluid layers[43], etc. Also various groups have tried to recover the appearance of inverse cascades, either numerical or analytically, keeping only the important points of the dynamics. One of these approaches[44] explored a Korteweg-de Vries model in a fully turbulent flow where the creation of self-organized states is produced by solitons with a small dissipation term. As well, another authors recovered a similar scaling law for an inverse cascade[45, 46] in inviscid fluids, where there is a transport of helicity in a flow with an averaged zero helicity and Gaussian distributions. Finally, in anisotropic flows lacking parity

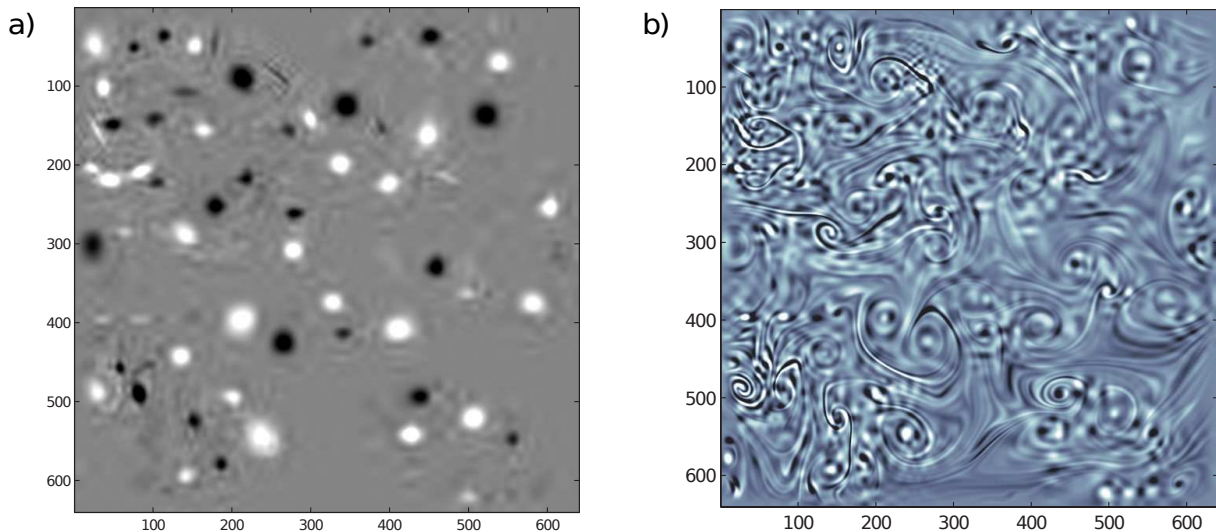


Figure 2.6: a) Vortical structures corresponding to the energy inverse cascade in 2D. b) Filamentary structures corresponding to the enstrophy in charge of the direct cascade in 2D.

invariance, another approach was proposed inspired on the magnetic field generation in turbulent flows in MHD[47], the AKA (anisotropic kinetic alpha) effect [12]. In this work we will present an evidence of an experimental inverse cascade in 3D turbulence, where the conservation of the angular momentum acts as the mechanism that sustains that cascade[48].

2.3 Von Kármán swirling flows

In 1921 Theodore von Kármán published a study called “Über laminare und turbulente Reibung” (On laminar and turbulent friction[49]), in this paper he discussed the case of an incompressible fluid moved by a uniformly rotating disk. Some time later G.K. Batchelor[7] (1951) studied the case of a viscous fluid pushed by two infinite coaxial rotating disks, where he also applied the similarity principle of von Kármán. Later, attracted by the work of von Kármán, several researchers started to address various generalizations of the problem and began to call them von Kármán (VK) swirling flows. A good theoretical review of swirling flows can be found in [50], in this review F. J. Zandbergen and D. Dijkstra face the problem of a flow between two disks enclosed in a cylindrical cavity (that was investigated before numerically and experimentally by D. Dijkstra [51]), stating that this type of problem should be considered due to its importance.

On the other side, the complexity of turbulence made hard to the researchers to find answers on the behavior of the non-understood turbulence ingredients (intermittency, large-scale anisotropy, deviation from the predicted exponents, etc.). They found in the von Kármán flow an excellent candidate to use as a turbulent generator instead of the classical grid. So since then significant advances on the characterization of different realizations of the von Kármán flows have appeared, one of them in 1991 when Douady et al.[52] reported the existence of intense vorticity filaments in the VK counter-rotation flow. Some years later J.-F Pinton and R. Labbe[29] proposed a correction to the Taylor hypothesis since in such types of flows (shrouded flows), the mean velocity lacks of a good definition. It was in that decade when most of the characterization of the co-

rotating case was published[53], where the observation of coherent structures in a co-rotating frame and even in those articles they appreciated a concavity on the temporal spectra, suggesting that it could be due to an inverse energy transfer.

This configuration was used as a test-bench for magnetohydrodynamics research using two conducting fluids as gallium (the VKG setup) and sodium (the VKS setup). It's noteworthy that von Kármán swirling flows has a direct application in the generation of the dynamo effect, in this area has been noted that the counter-rotation case is closely related to the s2t2 configuration studied in spherical geometry by Dudley and James[54], the one that had the lowest threshold for this instability. This interest triggered a broad range of studies in a close-to-one aspect ratio. From those works we would like to remark two contributions. First, the contribution made by L. Marie[55] about the characterization of the coherent structures in the counter-rotation case and the measure of the momentum transport and second, the extensive characterization of the transition to turbulence in the counter rotation case made by F. Ravelet[56].

Furthermore, some preliminary results about the characterization of the counter-rotation case[56, 57] made this configuration suitable as a basis for the study of Lagrangian turbulence. From here many others important advances were published (as Ref.[58–60], etc.). A good historical background about the history of von Kármán swirling flows until 2003 can be found in the thesis of F. Ravelet[61] and L. Marie [62].

After that, problems like intermittency were faced using the VK flow, where several groups addressed this question using the Eulerian and Lagrangian points of view. Also, other specific issues were addressed using this configuration: several new findings concerning the large scales appeared, as the work of de la Torre and Burguete[5] where they report for large Re the appearance of a bistable regimen where can appear random reversals between those solutions with very long residence times; mixing and transport[63] of particles were studied; and many others questions. A good review of some examples can be found in the thesis of R. Monchaux[64].

Relating to the study of large scales some pioneering works have appeared as Ref.[48, 65, 66], as well studies of the dynamics of particles in a turbulent flow as in Ref.[67, 68] and also novel results of the study of Lagrangian properties of particles in turbulence[69, 70] that have been shedding new ideas on the physics behind the mechanisms that produce turbulent flows.

2.3.1 Counter-rotation case

The mean flow scheme for the counter-rotation case showed in Fig.2.7 consists basically in two toroidal recirculations wherein the fluid is ejected radially by the impeller towards the cylindrical wall, there the fluid is redirected to the equatorial plane of the cylindrical vessel. Here the fluid coming from both impellers joins in an inflection point, where again the flow is diverted to the axis of the cavity. At the axis the fluid is absorbed because of the depression in the Ekman layers, thus completing a recirculation. This qualitative description of the flow corresponds to a laminar state, but also can be related to the average flow of the fluid when this remain in the fully development turbulent regime.

The transition from a laminar state to a fully developed turbulent regime, for the case of a von Kármán swirling counter-rotating flow, was widely documented by Ravelet et al.[56, 71]. For the characterization, they used the negative direction of rotation, which means that the concave face of the propellers will rotate clockwise. On our setup, we use the opposite sense of rotation. Based



Figure 2.7: Qualitative representation of the classical picture of the mean flow for a counter-rotating von Kármán flow. This is the classical representation of the VK flow, where the shear layer is situated at the mid plane.

on this study, we will explore the case where the fluid remains in the fully developed turbulent regime. In this case the average flow should be independent of the Re number and it is well known that large scale structures appear in this regime.

Some peculiar characteristics as the stability of the shear layer that describe the mean flow in the counter-rotation case of some von Kármán flows have been studied recently, but have not been able to give a solid explanation about the general character of this instability. Nevertheless in all cases, the VK flows share a lot of similarities as the sensibility of the hysteresis at the shear layer, where a small dissymmetry the layer tends to move it significantly to one side of the vessel[65, 72, 73].

3 Experimental Setup and Data Acquisition Techniques

Resumen

En este capítulo se describe el sistema experimental utilizado a lo largo de este proyecto, además se presentan las técnicas usadas para caracterizar el flujo. Para el estudio, hemos decidido utilizar el ahora clásico flujo de von Kármán en la configuración de cotrarotación. Con el fin de hacer más simple la referencia a esta configuración – debido a la gran cantidad de arreglos similares– hemos decidido llamar a nuestro dispositivo VKP (von Kármán Pamplona, ver la Fig.3.3). Nuestro dispositivo consiste de una cavidad cilíndrica cerrada, puesta horizontalmente dentro de un tanque cuadrado. La celda cilíndrica está cerrada en ambos extremos y dos propulsores independientes con palas curvadas son los responsables del arrastre del fluido. El tanque cuadrado tiene tres ventanas ópticas con el fin de permitir la visualización del fluido, al mismo tiempo estas ventanas nos permiten utilizar técnicas experimentales de velocimetría no invasiva. El fluido utilizado para todos los experimentos fue agua a $\sim 20^{\circ}C$.

Para caracterizar el flujo hemos utilizado tanto técnicas cualitativas como cuantitativas. La parte cualitativa de nuestra investigación básicamente consiste en la observación de burbujas de aire inyectadas en el flujo, o de partículas de vidrio huecas, usando su tendencia a concentrarse/alejarse de los vórtices, en función de su densidad. Para las medidas cuantitativas hemos utilizado dos técnicas de velocimetría, la primera es la Velocimetría Laser Doppler (LDV) y la segunda es la Velocimetría por Imágenes de Partículas (PIV). Ambas técnicas experimentales se complementan una a la otra, dandonos una buena resolución temporal y espacial respectivamente.

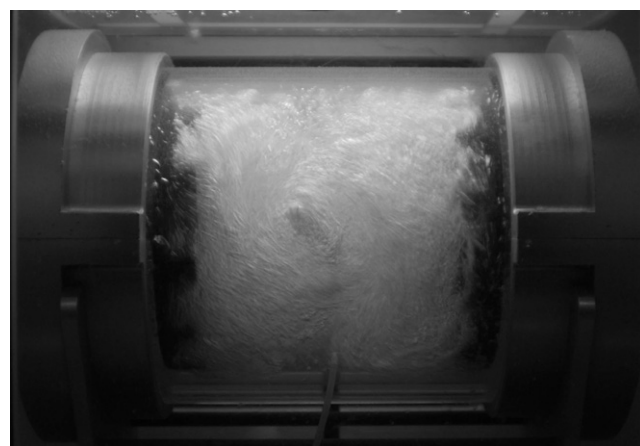


Figure 3.1: Front view of the experimental device.

Abstract

In this chapter we present the experimental setup that was used for this study and the techniques used to characterize the flow. We decided to use the now classical von Kármán flow in the counter rotation configuration. Due to the wide number of similar arrangements, and in order to facilitate the identification, we decide to call our device VKP (von Kármán de Pamplona, see Fig.3.3). Our device consists of a closed cylinder, placed horizontally inside of a square tank. The vessel is closed at both ends and two independent propellers with curved blades are responsible for the fluid drag. The square tank has three optical windows to allow the visualization of the motion of the fluid, at the same time these windows permit non-invasive velocimetry techniques. The working fluid used for all the experiments was water at $\sim 20^{\circ}\text{C}$.

To characterize the flow we have used both qualitative and quantitative techniques. The qualitative part of our research basically consists of observations of air bubbles or hollow-glass spheres injected in the flow, using their capability to stay or be ejected from the vortical structures. For the quantitative measurements we used two velocimetry techniques, the first one is the Laser Doppler Velocimetry (LDV) and the second one is the Particle image Velocimetry (PIV). Both experimental techniques are complementary, giving us good temporal and spatial resolution respectively.

3.1 Experimental Setup

Different types of configurations can be used to study turbulence, like grids in wind tunnels, jets in boxes, flows around cylinders, turbines, cylindrical cavities, etc. Some of them are generic, in the sense that can produce a homogeneous and isotropic turbulence, and some of them are for very specific situations. In our case we decided to use an experimental system that consist in a closed cylindrical cavity, where the fluid is moved by two propellers in counter-rotation. As it was explained in the previous chapter, at the beginning this device was proposed to study only the hydrodynamics due to its apparent simplicity. Later, it was used as a candidate flow to produce the dynamo effect. But novel non-understood features began to appear and the scientific community start to use this device to investigate turbulence or situations in where turbulent flows are involved. Nowadays maybe this device is one of the most used apparatus to investigate fluid dynamics due to its simplicity but at the same time because of its rich dynamics.

The aim of this setup is to explore a simple geometry where a turbulent shear flow will develop at a very high Reynolds number. Nevertheless this device has been designed with the capability of being easily modified, so different configurations can be analyzed and not only a closed cavity. For example, the cylinder could be taken out giving place to study open flows, or other types of geometries (i.e. square boxes), and also there is enough space to place larger impellers or experimental cells. Another peculiarity of this setup is that most of the manufactured parts of the system were made with a CNC machine (computer numeric control), so the symmetries are preserved in a high degree. In this way, we can reduce the instabilities generated because of the imperfections in the manufacture. As well, the power and inertia of the motors and impellers used to move the fluid were chosen to avoid fluctuations due to the drag that the fluid exerts on

the propeller.

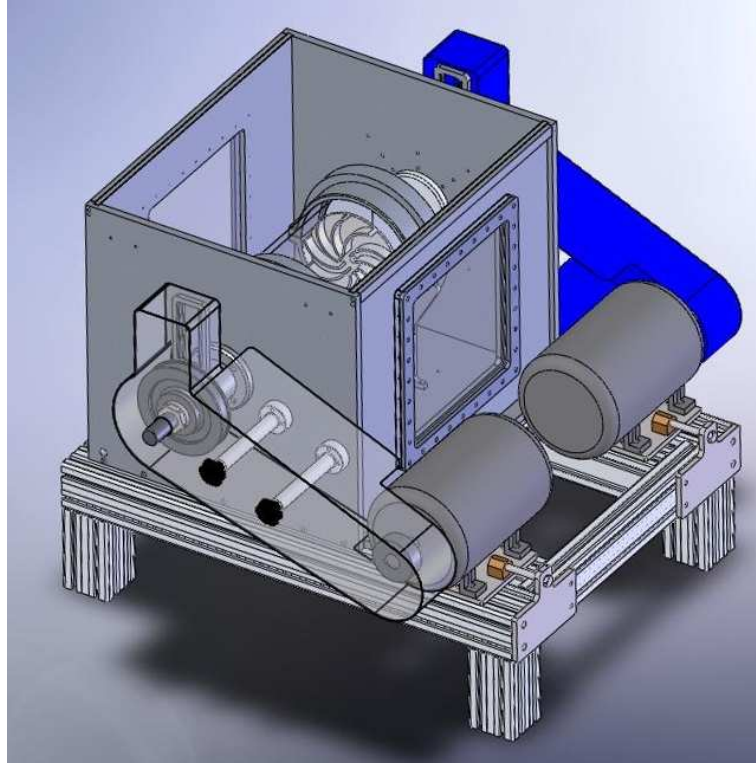


Figure 3.2: 3D view of the experimental setup, where the arrangement of the parts used to drag the fluid is presented.

3.1.1 Cavity

In the Fig.3.3 we present the used cavity, basically consists on a closed cylinder manufactured in Plexiglas with a diameter of $D = 20\text{cm}$ and a total length of $l = 32\text{cm}$. This cavity is held by two clamps located at the ends of the cylinder and both were attached to the bottom of an square tank. The clamps were made of aluminum and only the flat caps are of Plexiglas. This fastening system is located at the center of a square tank of $50\text{cm} \times 60\text{cm} \times 50\text{cm}$. The Plexiglas caps located at both ends, can be removed to let the turbulent flow interact with the surrounding fluid. It is noteworthy that the cylindrical vessel can be removed without affecting the location of the propellers.

The square tank was made of aluminum with three optical windows of polycarbonate. Two of them, located in two lateral walls parallel to the axis of the cylinder in order to have a visualization perpendicular to the axis of rotation and the third one was located in the top of the tank. The area of visualization for both parallel widows, is 900cm^2 ($30 \times 30\text{cm}$) and for the upper cover we used a plate that fits in the entire area of the tank. The function of the square cavity is to act like a cover to the inner cylinder, providing the necessary thermal insulation from the environment. Another attribute of this surrounding volume is to reduce the laser refractions that can affect the velocimetry measurements.

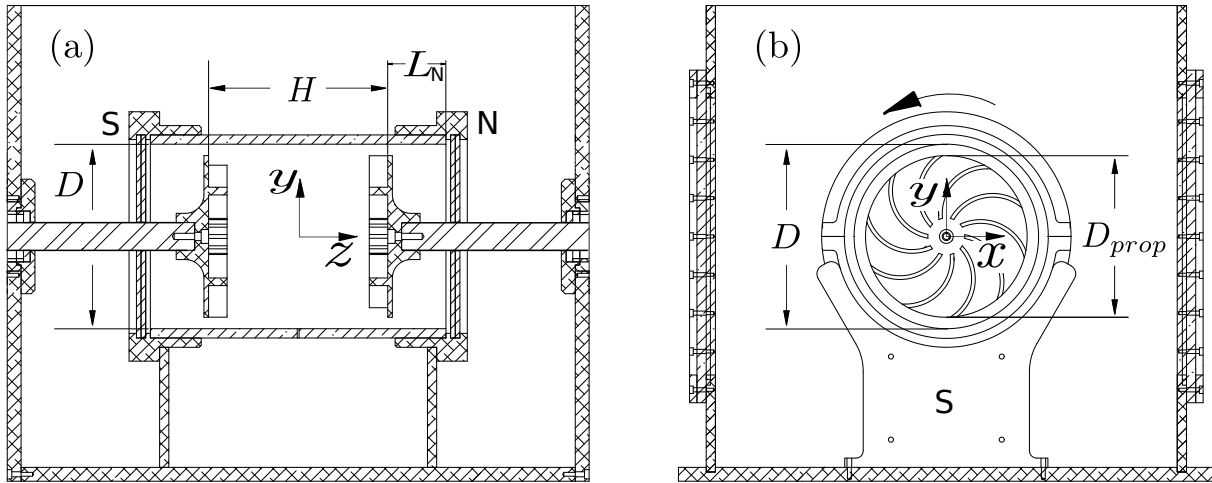


Figure 3.3: Experimental setup (a) Side view of the cylinder placed inside the square tank. The north propeller is located at $H/2$ and the south propeller is at $-H/2$. (b) Section of the cylinder where the rotation sense of the north propeller (counter clock wise) is indicated.

3.1.2 Impellers

During the past years, the propellers used to generate turbulence inside of a cylindrical cavity has been studied due to the interest in the dynamo action[61], and basically, these studies were based on the optimization of the ratio between the poloidal and toroidal recirculation's generated by the VK flow. The propellers used in this configuration are based on this study, since the characterization of the mean flow for this system was very well known and also because one of the original motivations of our research was to understand the effect of large scales on the dynamo action.

To drive the fluid we used two identical propellers of diameter $D_{prop} = 17.5\text{cm}$, with 10 curved blades 2cm high, each one of them has a curvature radius of 4.8cm and an angle between the blade and the impeller rim of $\theta = 30^\circ$ –see Fig.3.4. These pieces were manufactured with a control numeric machine, using as a material a solid piece of aluminum, giving us a tolerance of $5\mu\text{m}$. The impellers were anodized in black to avoid unwanted reflections of the laser beams used in the velocimetries. These pieces are screwed to an iron shaft of 47cm of length and 3cm in diameter.

Each one of the shaft is located perpendicular to the wall of the square tank, being retained with two slide bearings. The sealing is obtained using lip rubber seals. The setup has the capability of moving the propellers along the axis, using a screw system. The precision to fix the blades' position along z is of the order of 0.1mm and this precision is only possible when $L_{N,S} < 12\text{cm}$. For most of the experiments the propeller were located at $L_{N,S} = 6\text{cm}$ from both ends of the cylinder so the distance between the propellers is set at $H = 20\text{cm}$ for most of the experiments.

We used as gear system pulleys and belts from Optibelt. The pulleys at the impeller side is twice the size of the pulleys used in the motor, so we have a ratio $1 : 2$ between the frequencies in the impeller and the motor. These pulleys because of its size, weight and frequency ratio, give more inertia to the system and as we shall later will be a very important factor in our study. The

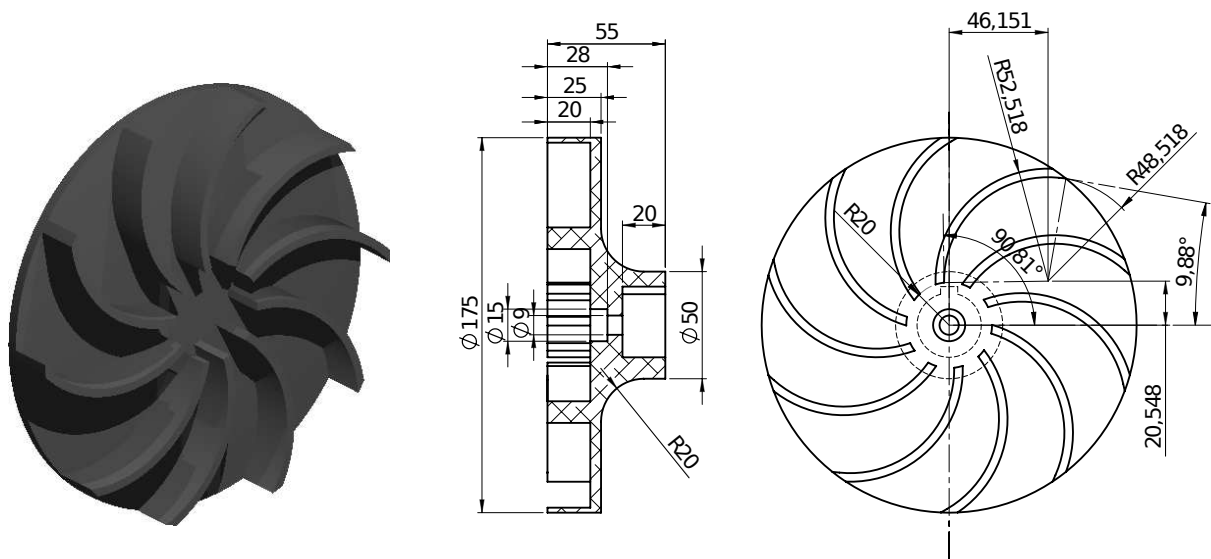


Figure 3.4: Scheme of the propeller used in the system; the units are in mm. These propellers were manufactured with a CNC machine from a block of aluminum, later were anodized in black.

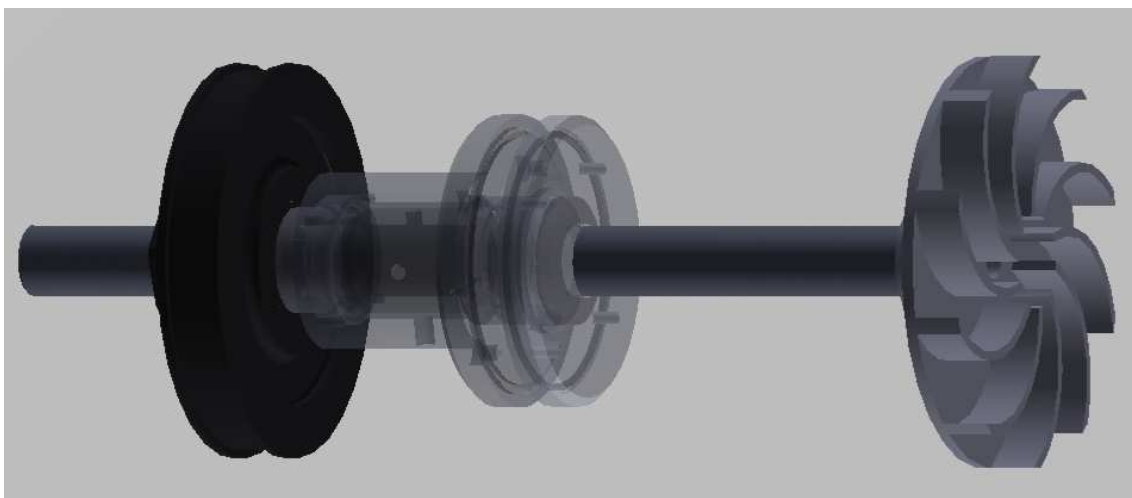


Figure 3.5: Representation of the pulley coupled to the propeller. The pieces presented as semi-transparent are the ones that fix the impeller to the wall of the tank.

total moment of inertia of this set-up (see Fig.3.5) is $I_{prop} = 15.92 \times 10^{-3} kg\ m^2$, this value was calculated by the manufacturer.

3.1.3 Motors

We have used two independent asynchronous motors ABB M3AA 100L (Fig.3.6.b), that can deliver a maximum power of $1.5\ kW$ each one. The maximum nominal rotation frequency that are capable to reach is $950\ rpm$, i.e. $15.83\ Hz$, but this value can be overcome if the torque needed is below its maximum value. The frequency of the motors can be adjusted at will between 0 and the maximum value. The total moment of inertia of the pulley and rotor parts is $I_{mot} = 9.84 \times 10^{-3} kg\ m^2$. Because of the ratio between the motor and impeller pulleys, the moment of inertia of the rotor is increased when it is transmitted to the impellers. The total moment of inertia for one of the whole impeller / shaft / rotor sets is $I_{tot} = I_{prop} + 4I_{mot} = 55.28 \times 10^{-3} kg\ m^2$. In the Tab.3.1 we present the principal characteristics of these motors.

Output (kW)	Motor Type	Current (A)	Speed (r/min)	Torque (Nm)
1.5	M3AA 100L	3.92	950	15

Table 3.1: Technical data of the motors.

The efficiency of the motor depends of the device that regulate the electrical current, the manufacturer recommends the use of a frequency converter – a variable speed drive (VSD) – to enhance the performance. In our case we used two VSD ABB ACS140 (Fig.3.6.a) which can be operated manual or remotely. The manual operation allows us a quick modification of the experimental setup, but the remote operation has a better resolution on the control of the VSD and in this case we can control it dynamically via a function generator.

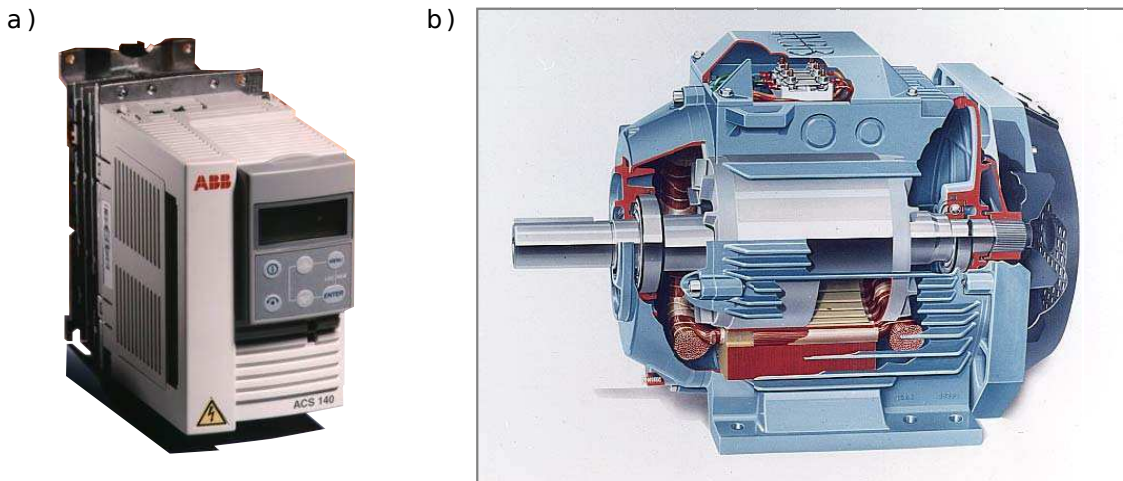


Figure 3.6: a) Variable speed drive used in the experimental setup. b) Section of the ABB 380V motor used.

3.1.4 Computer control

As we have said in the previous section, we used two waveform generators to control the rotation frequency of the motors. These two waveform generators are connect through a GPIB cable to a computer, where we control them through a home-made program (made by A. de la Torre and J. Burguete) using the Agilent VEE software, a graphical programming language similar to LabView. With this software we can introduce different types of signal to the motors, reaching the different configurations like: co-rotation, counter-rotation, $\Delta \neq 0$, random frequencies, sinusoidal modulations, and we can also use MatLab generated sequences, i.e. to produce random signals, uncorrelated or correlated in time.

The $20MHz$ function / arbitrary waveform generator used was the model Agilent 33220A, that offers operation for functions, pulses and arbitrary waveforms. The only difficulty with this system is when you want to synchronize some signals, the method to do this it is quite embarrassed. To do it more simple, we used an oscilloscope that can synchronize or put out of phase the signals.

Is worth mentioning that also were tried to improve the rotation stability of the propellers using a proportional-integral-derivative controller (PID controller), using an optical encoder Hegstler RI-32. Unfortunately, this approach does not improve the instantaneous stability that is quite below 1%

3.2 Measurement devices

During the last years the number of tools available to study turbulent flows has been growing, both statistical and experimental techniques. In the past, it was very popular the use of hot-wire anemometers. Although they are still used in many applications, the most used tools to study quantitatively turbulent flows are now the non invasive systems, as the optical velocimetry techniques. Nonetheless, the qualitative visualization techniques used since long time ago remain useful for the comprehension of the coherent structures in turbulent flows. Very good examples can be found in [19, 20]. In this research we have used three different techniques, each of them complementary to the others.

It should be noted that during the last decades the quality of the devices available to the experimentalists has been growing dramatically, either in speed of acquisition, resolution area, sensibility, quality, power, etc. Something similar happened with the computational power to analyze the data, either in faster processors, the amount of memory, the algorithms, etc. All this increased know-how obtained in the last times, is the reason about why now we have access to much more data on turbulent flows.

3.2.1 Image acquisition

The visualization techniques of turbulent flows are documented since long time ago, and even now are a very important tool in the design of cars, airplanes, buildings, ships, etc. Due to the very variety of techniques for visualizing turbulent flows, we choose one of the most simple, that consist in the injection of air bubbles and then track its evolution in time. We used this

technique because its simplicity, since the qualitative information obtained is very useful for the understanding of the structures that appear in the cylindrical cavity. Also, we use hollow glass spheres of $50\mu\text{m}$ of diameter, heavier than water, and larger spheres with different sizes (10, 20, 30, 40 and 50mm). In this late case the approach was totally different because the size of the particles was much larger than the integral length and their individual position was easily recorded.

For the visualization of the flow we use a monochrome CMOS firewire camera with a resolution area of $752 \times 480\text{px}$, the fast frame acquisition rate can go up to 60Hz . This camera was placed perpendicular to the axis of the cylinder, where the field of view correspond to the whole section of the cylinder. The air bubbles were injected via one hole placed at the equator of the cylinder; the rotational frequency of the impellers must be very high in order to split the air in a very small bubbles. After the injection of the bubbles, we must slow down the frequency of rotation in order to observe the dynamics at the wished rotation velocity.

In the following figures we show some examples of the acquired images:

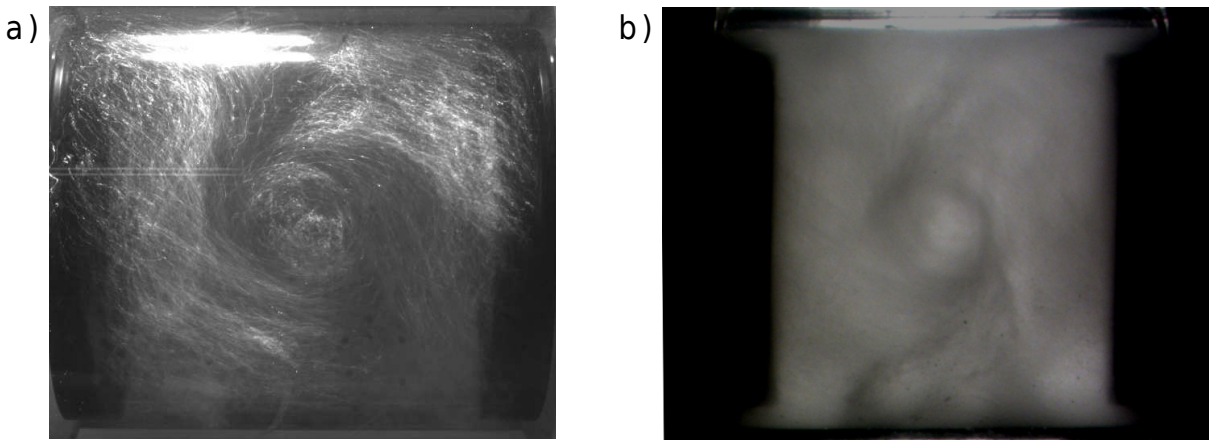


Figure 3.7: a) Illustration of the vortex appearing at the wall of the VK flow using air bubbles.
b) Similar picture obtained using hollow glass spheres.

3.2.2 Laser Doppler Velocimetry

In 1964 Cummins, Knable and Yeh were the pioneers to build an optical system which was presented as a laser Doppler instrument. Then, around 1969, the use of two crossed beams was introduced (Lehmann and von Stein and Pfeifer[74]) to create a volume where the light can be reflected by the tracers, and then recovered and measured by a photo-detector. These are the basic parts of any laser Doppler configuration available nowadays. During the past years many people has been perfecting this technique, where the use of monochromatic and coherent light sources (laser) plays an important role.

The general idea of this measurement technique is that in the intersection of two monochromatic and coherent light beams, a pattern of interference fringes is created in a measurement volume (called dual-beam configuration). When a particle crosses this volume, will traverse alternatively bright and dark regions, producing a characteristic oscillating scattered light that can be recorded with a detector. Therefore, the magnitude of the velocity perpendicular to the fringes can be obtained due the time that the particle takes to cross the fringes and the value will depend

of the movement of the tracers velocity[74].

Frequency Shift Method

The frequency shift method is based on the analysis of the burst signal emitted by the particles that cross the measurement volume. This method uses a Bragg cell that slightly shifts the frequency in one of the laser beams. As a consequence, these fringes moves constantly in a given direction, so we can recover not only the absolute value, but also the orientation of the velocity component. To obtain these values, it is possible to get a simple expression to know the Doppler frequency of the particle immersed in the flow related to the velocity and the shifted frequency that give us the direction, using the expression (a completed discussion can be found [74, 75]) :

$$f_r = f_{sh} + \frac{v_p}{\lambda_b} \cdot (\mathbf{e}_1 - \mathbf{e}_2) = f_{sh} \pm \frac{2\sin\theta/2}{\lambda_b} |v_{p\perp}| \quad (3.1)$$

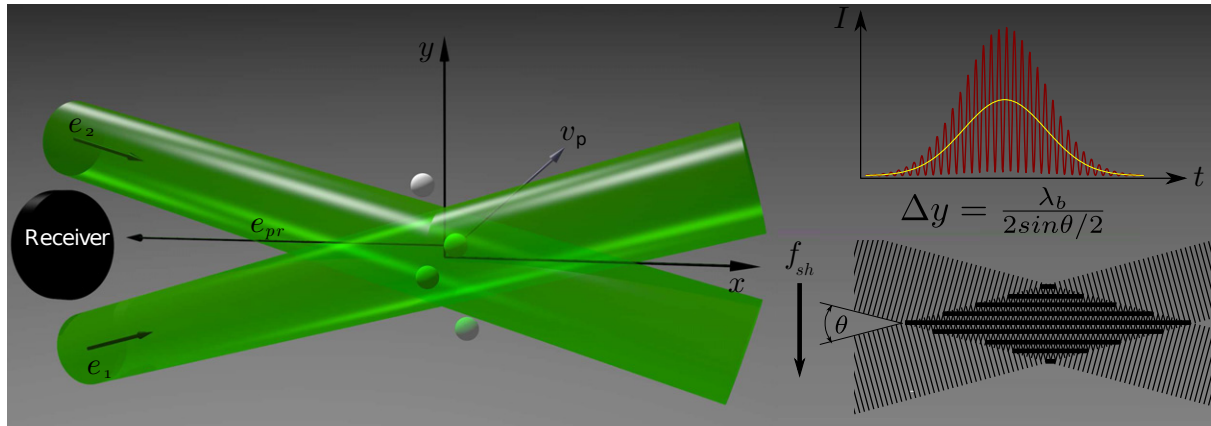


Figure 3.8: Dual-beam optical configuration for incident beam system. A schematic representation of the particles crossing the measurement volume is presented. On the right side we can see a reconstructed pattern of fringes (bottom) and the intensity burst produced by a single particle crossing this volume.

where f_r is the frequency detected by the receiver, Δy the distance between the fringes, f_{sh} the shifted frequency and $v_{p\perp}$ the velocity component perpendicular to the fringes and associated to the particle. An important peculiarity of LDV systems is that the particles are randomly distributed on the fluid causing a non-equally spaced sampling of the data, to avoid this problem in our results we follow a basic reconstruction method that consist to remap the randomly sampled into a evenly sampled signal.

Another common problem when this technique is applied in a non-stationary flow, is the biasing effect that influence the histograms obtained from measurements with LDV[76]. This biasing happens because the number of particles that cross the measurement volume is proportional to the fluid velocity; assuming that the particles are equally distributed in the fluid volume. In other

words, when the flow traversing the measurement volume has a velocity larger than the average, we will count more events of this fast flow than when the flow has a velocity below the average. So, the weight of the large velocities will be artificially higher than the real one in the histograms. This is a result that cannot be avoided, only it's possible stay aware and try to see if this fact has an influence on the dynamics, knowing this is clear that we can expect an overestimation for the weight of the large frequencies.

As it is our interest to investigate the large scales in turbulent flows, we follow a guideline proposal by Adrian and Yao[77]. They suggest that the mean data rate of acquisition should be at least twenty times the largest frequency at which measurements without distortion are required (Fig.3.9 shows a velocity series by LDV and its reconstruction). In our case we use a data rate at least one order of magnitude the larger frequency we are interested on the system, and then we perform a linear interpolation that highly fits to the recommendations by [77]. We would like to note that their recommendation cannot be fulfilled in a turbulent experiment, because very high frequencies are present.

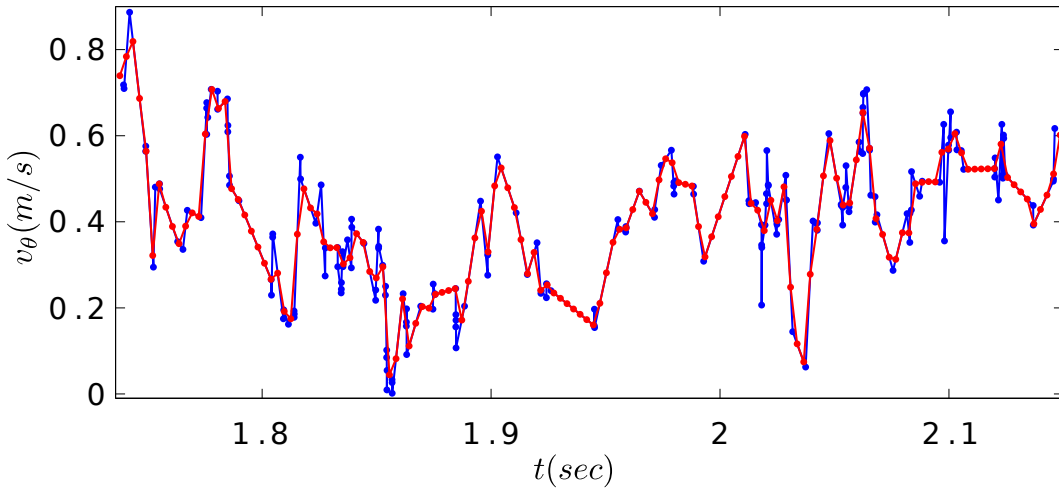


Figure 3.9: In blue sampled velocity via LDV and in red the reconstructed velocity signal.

Characteristics of the commercial system

For this research we used a commercial LDV system, the equipment was manufactured and assembled by the company *TSI Incorporated* and consists in a laser source, an optical interface, a photo detector, a spectrum analyzer and a computer for the analysis. Also, this system counts with a 2D traverse system that is able to displace the LDV probe remotely along the x and z axis with a good accuracy ($\pm 300\mu m$).

The source of light is an *Argon Laser Stellar-Pro-L*, that offers a few wavelengths between $457.9nm - 514.5nm$ with a total maximum output power of $300mW$. At the output of the laser, a fiberoptic multicolor beam generator was aligned to separate the wavelength of $514.5nm$, this device gives a pair of beams, one with and the other without the frequency shift (applying an offset of $40MHz$ to one of the laser beams as described above). These laser beams are conducted using optical fibers into the probe. The separation between the beams at the output of the probe is $50mm$, they converge at a focal distance of $363mm$ with an angle between them of $\theta = 7.9^\circ$.

The measurement volume according with the manufacturer is an ellipsoid of 1.31mm length by $90\mu\text{m}$ in the two other directions, where a set of 24 interference fringes is obtained. To convert the light into an electrical signal, the system uses a photodetector module (PDM) controlled by a computer and whose signal is sent to a spectrum analyzer (FSA) that processes the signal coming from the PDM selecting valid bursts that are sent to the computer. This device is capable to process the Doppler frequency up to 175MHz.

Correction due the different interfaces

The measurement of the velocity of a fluid flow inside in a cylindrical cavity using an optical device can be affected because of the geometrical properties of the cavity and by the different optical characteristics of the materials. This is due to the difference of the refraction index between the materials, as for example in air ($n = 1$), polycarbonate ($n_{pc} = 1.58$) and water ($n_{H_2O} = 1.33$). For the case in where we would want to measure different positions along the area of the cylinder, the displacement of the measurement volume should be corrected.

To correct the position that it is deviated because of the refraction of light, we invoke the Snell law given by:

$$n_1 \sin \alpha_1 = n_2 \sin \alpha_2 \quad (3.2)$$

In our measurements these corrections were done for the two interfaces and for the components v_θ , v_z , in where we can be sure that the mapping area for the velocity measurements was done equispaced.

Without the square tank, the corrections will be crucial because of the curved interface between the Plexiglas cylinder and the air. Depending on the measurement position the incident angle will vary, so a different correction will be needed in each position. Even more important, in equation 3.1 the numerator would depend on the position, whereas the denominator would have a constant correction, and so a correction of the velocity must be applied for each different position. Using a square tank this factor is constant, and the same happens for the measurement positions.

Mean velocity field via LDV

If we assume that the flow is axisymmetric, it is enough to measure the velocity components in a horizontal plane that contains the vessel's axis. To do this we generate an equispaced grid of 21 by 11 points of measure (radial and axial direction resp.) at $\theta = 0$, the coordinates for this spots were corrected avoiding the refraction problems. The measured time in every point of the grid was 120 seconds, with a mean data rate of 900 bursts per second. Noteworthy that, in some spots of the grid the LDV had troubles to make the velocity measurements, principally due the laser reflections at the boundaries and in other cases because the system was not transparent (inside the propellers' region). In order to solve these problems, we apply the same criteria that in numerical simulations, assuming a no-slip condition in the cylinder boundaries.

Also, because of the axisymmetry, the three components of the velocity fields in the continuity equation 3.3 are disconnected, so the poloidal and toroidal components behave independently. Actually, the v_θ term of the continuity equation vanishes, and we obtain that the radial and axial components are strongly coupled:

$$\nabla \cdot \mathbf{U} = \frac{1}{r} \partial_r(r U_r) + \partial_z U_z = 0 \quad (3.3)$$

Taking advantage of this, we can define a poloidal stream function $\psi(r, z)$, defined in the plane of measure, where:

$$\begin{aligned} U_r &= -\partial_z \psi \\ U_z &= \frac{1}{r} \partial_r(r \psi) \end{aligned} \quad (3.4)$$

So we can numerically recover ψ using the mean velocity value of U_z , to later recover the mean value U_r :

$$\psi = \frac{1}{r} \int_0^r (r' U_z) dr' \quad (3.5)$$

3.2.3 Particle Image Velocimetry

The PIV terminology has been used since about thirty years, and during this time has become one of the reference tools for the study of fluid dynamics. According to R. J. Adrian, “*PIV means the accurate, quantitative measurement of fluid velocity vectors at a very large number of points simultaneously*”(Adrian[78],,2005:1). The operating principle is quite simple, in a two step procedure: first, we illuminate the fluid flow previously seeded with tracer particles with a laser plane and then take a picture of the flow; after a small increment of time we take another picture, and then the velocity of the particles can be obtained computing the correlation between both images that informs us about the displacement of the particles. However, the output vector fields and the magnitude of the correlated velocity are very sensitive to the analysis –an example of this procedure is presented in the figure 3.10.

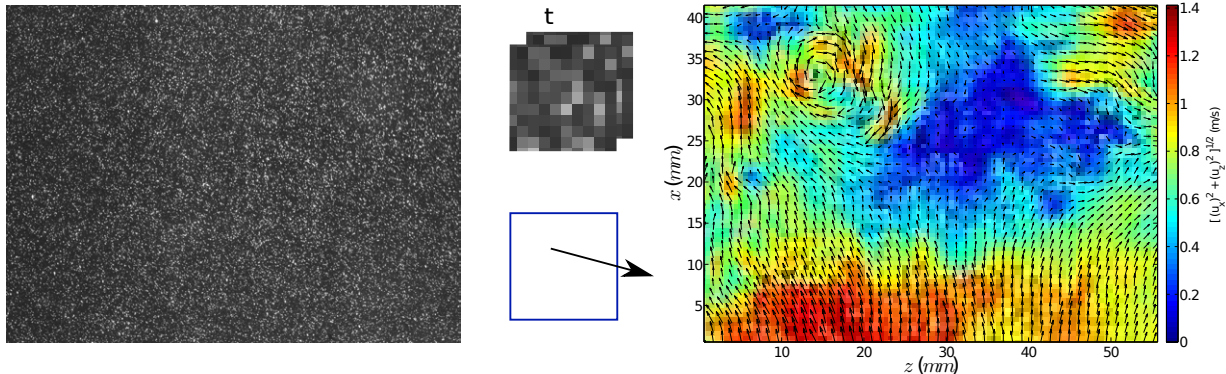


Figure 3.10: Simple scheme of a PIV analysis. On the left we present one image of the illuminated particles, on the middle a pair of interrogation areas before being correlated and its representative correlated vector. On the right the mean field obtained via two pair images.

The PIV technique can be split in two phases for a simpler interpretation, one is the acquisition of the images and the second one consists on the numerical tools that are used to correlate the data and the post-processing. In Fig.3.10 we present a simple scheme for these two phases, on the left

side we present the original image used for the PIV and on the right side the post processed fields.

Step.1 Image acquisition

The acquisition of images for the PIV analysis is the most important part of this technique, since any mistake in this phase could damage all the further analysis. This method basically uses three elements (Fig.3.11) that are, seeded particles in the fluid, one source of light (laser with light sheet optics) and a frame grabber. Each one of these components should be chosen depending on the characteristics of the system that we would like to analyze, because the specific characteristics of these items can increase the noise of the measured velocity fields.

The whole acquisition system is controlled by an external pulse generator, in order to synchronize the two light pulses with the acquisition of the images and the camera. This gave us the advantage of recording up to 4200 images in blocks of 300 images; that generate 2100 vector maps. For almost all the cases presented here, the acquisition rate (number of velocity fields per second) was 1Hz, 6Hz or 15HZ.

In the following we present a description of the different elements used in the image acquisition phase:

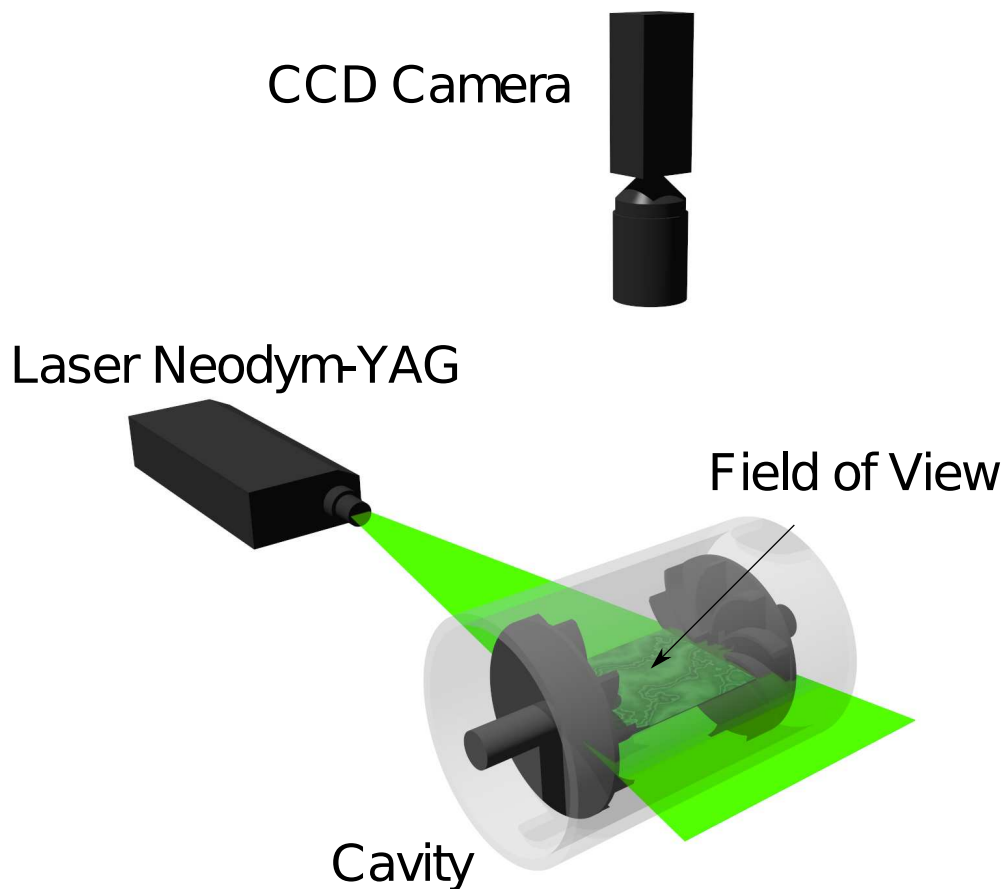


Figure 3.11: Scheme of the PIV elements used in this experimental setup.

Laser

In a PIV system the light source must be strong enough to illuminate the seeded particles and to produce a good contrast in the final image, but at the same time, the lighting must be very short (compared to the velocity of the flow) to produce clear images of the positions of the particles instead of blur. That means that the light source must be a high power during short periods of time and the simplest way to produce such bright source is using a laser source.

We used a solid state Neodymium-YAG (a neodymium-doped yttrium-aluminum-garnet crystal) pulsed laser, one of the most used laser for PIV [79]. This type of laser has good mechanical and thermal properties, moreover has a Q-switch that provides the possibility of increasing the power of the laser pulse and shorten the pulse duration. This laser uses a dual lamp-pumped Nd:YAG rod head, and produces infrared radiation with a wavelength of 1064nm . A nonlinear crystal produces a frequency doubling through a second harmonic generation, and in this way the laser changes the wavelength to the visible range $\lambda = 532\text{nm}$, without disturbing the beam quality. Right after the beam output from the laser system, a lens arrangement modifies the Gaussian beam into a laser sheet. This sheet can be focalized so in its narrower location has a thickness of 1mm and the light energy per pulse is around 15mJ . Noteworthy that the emitted laser sheet always diverge, here this effect was not taken into account because the variation of the thickness in the illuminated area is small enough compared to the field of view.

Camera

A digital monochrome 1" two megapixel progressive scan CCD camera was used, the effective area of the sensor is $1600 \times 1200\text{px}$. In the PIV mode operation the camera starts the first exposure $4\mu\text{s}$ after the trigger signal is received, the accumulation time for this frame is $4\mu\text{s}$; $1.5\mu\text{s}$ after, the camera will begin the second exposure and the accumulation time could go up to two seconds. The total time necessary to grab a pair of images and then store them on the memory of the computer is around $50\mu\text{s}$. Once the camera fills up the physical memory of the computer –around 300 full frame images–, the computer saves this information in the hard disk and starts a new acquisition.

Using this technique, the minimum time between two laser flashes can be adjusted to $2\mu\text{s}$. In our setup, the full frame covers in the most adverse situation around $16\text{cm} \times 12\text{cm}$, so the pixel size is approximately 0.1mm . Those values determine the value of the maximum velocity that can be measured. For an interrogation area of $16 \times 16\text{px}$, this maximum velocity would be $1.6\text{mm}/2\mu\text{s} = 400\text{m/s}$, quite above of the typical velocities present in our flow.

One disadvantage of this type of cameras is the so called “image blooming”, that occurs when the maximum charge that can be stored per pixel is reached, causing a saturation that produces small vertical white lines around some tracers.

Particle tracers

Two different types of particles were chosen: the first one and most commonly used were silver coated hollow glass spheres with a density of $\rho = 1.65\text{g/cm}^3$ and a diameter of $d_p = 14\mu\text{m}$. The second type of particles used was polyamide spheres with a diameter of $d_p = 50\mu\text{m}$ and a density of $\rho = 1.03\text{g/cm}^3$. We performed different measurements to test how the density matching / differences could affect to the results. As no differences were appreciated between the data obtained using both particles, we chose the particles that are more effective to scatter the light

and consequently allow better statistics for the same seeding density (number of particles per volume).

Anyway, both type of particles are small enough to not to affect the study of scales larger than the Taylor microscale in a turbulent flow. A good discussion on the effect of the size and density of the particles when dealing with turbulent flows can be found in [80–82].

Pulse generator

A 575 BNC pulse generator was used, the apparatus works as a timer function non-retriggerable, multi-vibrator pulse generator. In other words, when this device is activated, it produces a continuous series of pulses. It has four channels that we employed three of them to synchronize the camera trigger and the two laser pulses. We chose the necessary delay between the two laser pulses, that will control the time interval between the two images. Using an oscilloscope we can synchronize the laser pulse with the first acquired image, and then choose different delays between the pair of images depending on the characteristic velocity of the flow.

Step.2 Post-processing

Once the pictures were recorded, the velocity of the particles can be obtained using auto-correlation or cross-correlation methods. In our case we chose the cross-correlation method, as it is one of the most common methods to analyze two single exposures. Previously we first delimit the interrogation area in such a way that we have more than six particles inside them[83]. In our case the mean value of the quantity of particles per interrogation area was 14 and in the worst scenario 6.

Once these areas are defined, the correlation algorithm is applied to each one of these image elements, so we will get a velocity vector per interrogation area. The velocity field resolution will be determined by the size of the image divided by the size of the interrogation area. For an image of $1600 \times 1200\text{px}$ and an interrogation area of $16 \times 16\text{px}$, we will recover a velocity field of 100×75 values, i.e, approximately two orders of magnitude in the spatial Fourier space.

The displacement of a distance \mathbf{D} of the particles images in a dimensional space after a time increment $t' = t + \Delta t$, is given by:

$$\mathbf{X}'_i = \mathbf{X}_i + \mathbf{D} = \begin{pmatrix} X_i + D_X \\ Y_i + D_Y \\ Z_i + D_Z \end{pmatrix} \quad (3.6)$$

where \mathbf{X}_i was the initial position of a single particle i at a time t .

To detect where is situated a particle in an exposure, is commonly used the image intensity defined from the convolution product of $\tau(\mathbf{x})$ (point spread function, see[79]) and the geometric image of the tracer particle in the position \mathbf{x}_i . Then we can obtain the image intensity for the interrogation areas from:

$$I(\mathbf{x}, \Gamma) = \sum_{i=1}^N V_0(\mathbf{X}_i) \tau(\mathbf{x} - \mathbf{x}_i) \quad (3.7)$$

where $V_0(\mathbf{X}_i)$ is the transfer function giving the light energy of the integration volume and Γ describes the set at a given time t .

Finally knowing the intensity of the interrogation areas for the two exposures, we can use the cross-correlation function for two interrogation areas defined as:

$$R_{II}(\mathbf{s}, \boldsymbol{\Gamma}, \mathbf{D}) = \frac{1}{a_I} \sum_{i,j} V_0(\mathbf{X}_i) V_0(\mathbf{X}_j + \mathbf{D}) \int_{a_I} \tau(\mathbf{x} - \mathbf{x}_i) \tau(\mathbf{x} - \mathbf{x}_j + \mathbf{s} - \mathbf{d}) d\mathbf{x} \quad (3.8)$$

where a_I is the interrogation area, \mathbf{d} the particle image displacement and \mathbf{s} the separation vector in the correlation plan.

Once this processing is done, we need to identify the valid vectors obtained from the PIV from the spurious data, and in our case we made a validation based on the correlation peak (sharpness and existence of only one peak). For the worst scenario we get less than 10% of invalid vector and for most of the vector fields, the invalid vectors were less than 5%. Since the percentage of invalid vectors was reasonably low, we decided to substitute these vectors using a moving average scheme.

For the PIV measurements we used three different fields of view of: $156.6 \times 127\text{mm}$, $47.8 \times 35.6\text{mm}$ and $17.4 \times 13\text{mm}$. To compute the vector maps and the calibration, we used the Dantec Dynamics software *FlowManager 4.50.17*. The parameters of the post processing analysis used were: an overlapping of 50%, interrogation windows of 32×32 px, the particles density was ~ 14 ppia (particles per interrogation area) and a moving average for vectors less than the 6%. We based this parameters choice in a study made by Poelma et.al.[83] Some optimization treatments can be used to improve the correlation between the peaks; one method consists on using an offset between the exposures to reduce the in-plane loss. This treatment would be very useful to better define the correlation peaks.

Uncertainty on the measurements

Different factors can alter the velocity measurements in our experiment. Some of them are inherent to the equipment and others could come from the assumptions that we made. Here we would like to discuss briefly the influence of those that we consider the most important.

Effects of the size and density of the particles.- An important aspect that we would like to emphasize is the assumption that the particles that we introduced in the flow follow the same trajectories as the fluid elements do. Novel studies expose how the dynamics of inertial particles can be affected by turbulent flows because of their size and density[80–82]. Concerning the size, Qureshi et al. concluded that the decrease of the acceleration variance occurs in the range $5 < d_p/\eta < 15$. Based on this approach, seems that our particles ($d_p = 0.45\eta$, $f_{prop} = 3.16$) won't reflect the effects of intermittency or lift effect that large particles has, giving us the certainty that the characterization could be acceptable. Nonetheless, it has been recently noted that the use of particles with higher density than the fluid generate clusters (review paper [64]). In our case, where the particles are heavier than water but smaller than the Kolmogorov scale, there is not yet experimental evidence that shows the formation of these clusters. Anyway, taking into account all this information and knowing that our study is for large scales, we believe that density could affect to the estimation of the turbulent parameters, but not for the study of coherent structures.

Effects of the post-processing.- In the post processing phase, it is well known that the overlapping can alter the spectra, but this happens only in the range of the small scales and in

some specific situations [83, 84]. To avoid this effect, we introduce a sufficiently large number of tracer particles in the area of interrogation. In our system, typically we have 16-18 tracers for interrogation window, larger than the numbers proposed by Polema et. al[83]. Only for the small window (where the inertial range appears) we had about 6 tracers per interrogation area, but only in a 2 – 5% of regions.

Temporal Spectra.- For the case of the PIV measures it is impossible to recover the temporal power spectrum of the velocity, since the frequency acquisition rate not fulfill with the Nyquist sampling theorem, causing aliasing on the computation signal. The maximum acquisition data rate capable by the system is of $15Hz$, with a maximum period of time limited by the random-access memory that in this case is 1Gb. So, it is impossible to compare the details of the temporal behavior obtained using LDV and PIV systems. The only information that can be computed and compared is the mean value and other global descriptive statistics parameters.

3.3 System Features

Many features of the experimental setup were carefully established, so the system can be modified at will with a high degree of precision. Here we will discuss some aspects that can affect the measurements and will try to explain how we control such characteristics.

3.3.1 Geometrical features

The experimental cavity has been manufactured to be geometrically symmetric around the axis of the cylinder. We have used two different reference systems, one of them Cartesian, the other one a cylindrical coordinate system. In both cases the z -axis is aligned with the axis of the cylinder. In the case of the Cartesian axes, the y axis is parallel to the gravitational force and for the positioning system of the measurements seems the most adequate. On this framework different distances can be adjusted in order to explore other configurations.

We can define the aspect ratio, as the relationship between the diameter of the cylinder and the separation length between the propellers (eq. 3.9). For this research we kept fixed this parameter with a value of $\Gamma = 1$.

$$\Gamma = \frac{D}{H} \quad (3.9)$$

Nevertheless, we changed the distance ($L_{N,S}$) between the propeller and the closing ends of the cylinder in some cases. The distances $L_{N,S}$ can be modified at will so we can test the effect of the fluid behind the propellers on the dynamics.

In some cases, $L_N + L_S = constant$, so the only effect was to move the experimental volume inside the cylinder and the aspect ratio was always $\Gamma = 1$. In other cases we modified these distances conjointly, so we changed the aspect ratio Γ , without modifying the diameter of the setup that was always fixed to 20cm. The aspect ratio in those cases was modified in the range $0.5 < \Gamma < 1.5$.

3.3.2 Working fluid

Since our interest is the characterization of the dynamics of a turbulent flow, we chose as working fluid water at $20 \pm 2^\circ\text{C}$. The main reason is because there is no implicit risk associated to the fluid itself as could be the case with other chemical products, and it is very easy to maintain clean the experimental setup. Another advantage is that is easily available and transparent, so the optical techniques described above can be used. The only drawback is that the viscosity of water depends strongly with temperature, so we should be careful and maintain the setup temperature stable. The changes in the temperature of the fluid inside of the cylinder for the closure configuration were reported in [85]. Those changes in the temperature has been neglected due the regime explored.

Another important aspect is the volume of fluid stirred, this volume will depend on the dimensions of the used configuration. In our case for most of the measurements we decided to use a closed cylindrical cavity and only in a few cases we leave the cavity open. Finally, the container is open to the atmospheric pressure and it is not possible to avoid cavitation in some situations (i.e. high frequencies or rotation of the propellers with the opposite sense).

3.3.3 Control parameter

Once the geometry of the system and the working fluid have been fixed, the only parameter available is the frequency of the propeller. So, this will be our main control parameter, and is directly related to the Reynolds number defined as in eq.3.10. In this expression R and ν will remain unchanged and only V_{prop} will change.

$$Re = \frac{RV_{prop}}{\nu} \quad (3.10)$$

The control parameter of this study is the velocity and the direction of the propellers V_{prop} (eq.3.11), the adjusting of this parameter is how we reach different values for Re number.

$$V_{prop} = 2\pi R_{prop} f_{N,S} \quad (3.11)$$

In this expression, the velocity of the propeller should be the same for both propellers, but in order to impose a dissymmetry in the system, we can define a parameter of dissymmetry defined as:

$$\Delta = \frac{f_N - f_S}{f_N + f_S} \quad (3.12)$$

where f_N and f_S correspond to the frequencies of each one of the propellers.

4 Mean Flow Characteristics

Resumen

Durante las pasadas décadas se han construido diferentes tipos de configuraciones de von Kármán, ya sea para el estudio de la turbulencia o para aplicaciones magneto-hidrodinámicas. La representación clásica del flujo medio para este sistema, son dos flujos en rotación separados por una capa de cizalla en la mitad, ambos con la misma helicidad y con la mayoría de sus simetrías preservadas. En este capítulo reportamos los resultados que se obtuvieron para la caracterización del flujo medio que aparece en la cavidad experimental para un flujo en régimen turbulento. Mas adelante se discutirán algunas características que son similares con otros von Kármán y a su vez se discutirán algunas diferencias.

En nuestro caso podemos ilustrar este flujo en la Fig.4.1, usando una integración de la velocidad media para períodos de cuatro órdenes de magnitud mayores en comparación con el tiempo característico del flujo. Cabe notar que este flujo no representa el flujo medio utilizado para esta caracterización, pero sin embargo, lo podemos utilizar para comparar las diferencias que existen entre el flujo medio observado en este sistema experimental y los flujos medios previamente reportados.

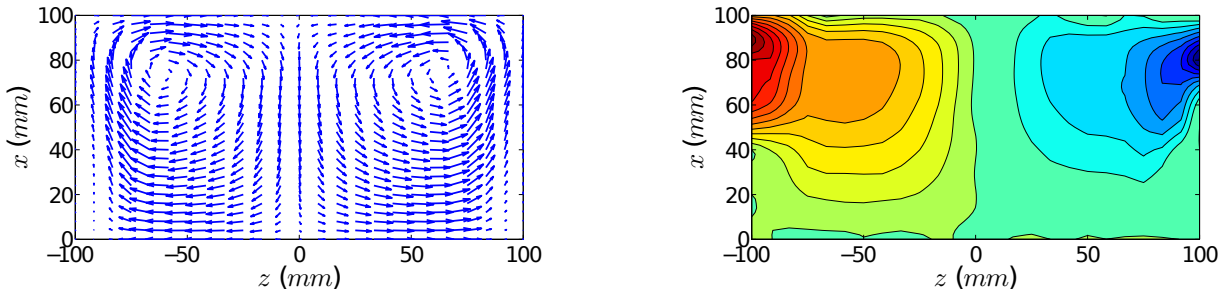


Figure 4.1: Representation of the mean vector field and contour map of the mean azimuthal component, where the shear layer stays at the midplane.

Abstract

Different types of von Kármán swirling flows were built during the past decades, either for the study of turbulence or for magnetohydrodynamics applications. The classical representation of the mean flow for this system, consists on two rotating flows separated by a shear layer at the mid plane, both with the same helicity and with most of its symmetries preserved. In this chapter we will report the results that we obtained for the characterization of the mean flow that appears in this peculiar experimental setup at the fully developed turbulent regime. Further we will discuss some characteristics that are similar with other von Kármán flows and also we will discuss the principal differences between similar setups.

In our case we can illustrate this flow as in Fig.4.1, using an integration of the mean velocity values for periods four orders of magnitude larger than the characteristic time of the flow. Noteworthy that this flow don't represent the mean field used for this characterization, but however, we can use it to compare the differences between the mean fields previously reported in other configurations and the mean field observed in this setup.

4.1 Mean flow, a bistable regime

In 2007 De la Torre et al [5] reported that the mean flow measured in an exactly counter-rotation von Kármán configuration spontaneously breaks the symmetry of the experimental set-up, showing that the shear layer in this device was not located at the mid plane as in other similar configurations –see FIG.4.2.a. They found two symmetrical mean velocity fields that can be obtained one from the other using the π -rotation symmetry around any diameter in the equatorial plane. This mean flow randomly jumps between both possible solutions, and remains in that state for long periods of time ($\sim 20\text{min}$) –we called to this observation a reversal between the states north(N) and south(S). The characterization of this bistable system was reported in [5, 85], in where A. de la Torre et al. described this slow behavior with a simple model based on a three-well potentials.

To have a better comprehension of these reversals, in FIG.4.2.b we plot the azimuthal velocity in function of time measured with the LDV technique at the position $x = 9\text{cm}$, $y = 0$ and $z = 0$, where we can observe how these reversals occur spontaneously and with a random periodicity. If we apply a low pass filter to the azimuthal velocity signal (blue line) and only preserve the modes that correspond to the low frequencies(yellow line), we can identify the time where the reversals happen and the times the system remains in one or in the other solution (red line). Noteworthy that in our experiment the shear layer never remain in the central region, however the time that spend in one or in other solution could be very short ($\sim 20\text{sec}$) or very large ($\sim 60\text{min}$), later we will discuss this more deeply.

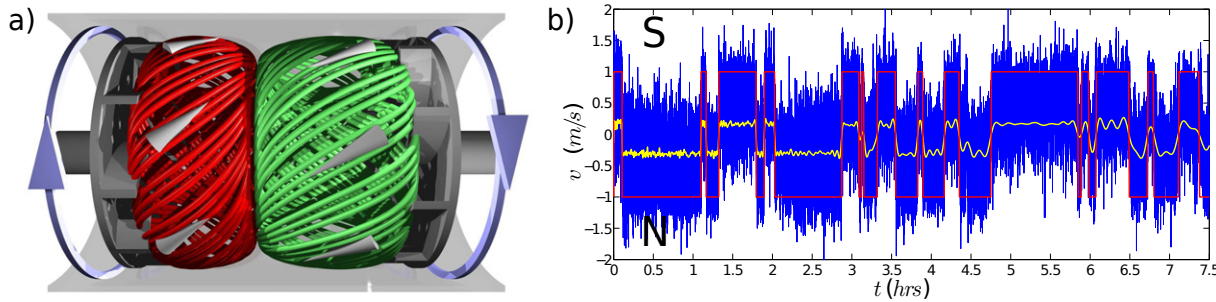


Figure 4.2: a) Reconstruction of the asymmetric mean flow using averaged trajectories. b) Azimuthal velocity near the wall ($x = 9\text{cm}$) at the equator ($z = 0$). The S (resp. N) indicates whether the south (resp. north) cell dominates.

4.1.1 Characterization of the N,S states

In this characterization we looked at the behavior of the large scales –slow frequencies– for each one of these solutions, since both solutions present identical statistical properties. In order to prevent the reversals we followed a detailed description given by Burguete et al[72], where a small dissymmetry applied to the system favors one of the states, and the reversals are suppressed. Therefore increasing the frequency of rotation in a 1% on one of the propellers, we can remove these reversals and in turn preserve the main characteristics of the flow for a single state.

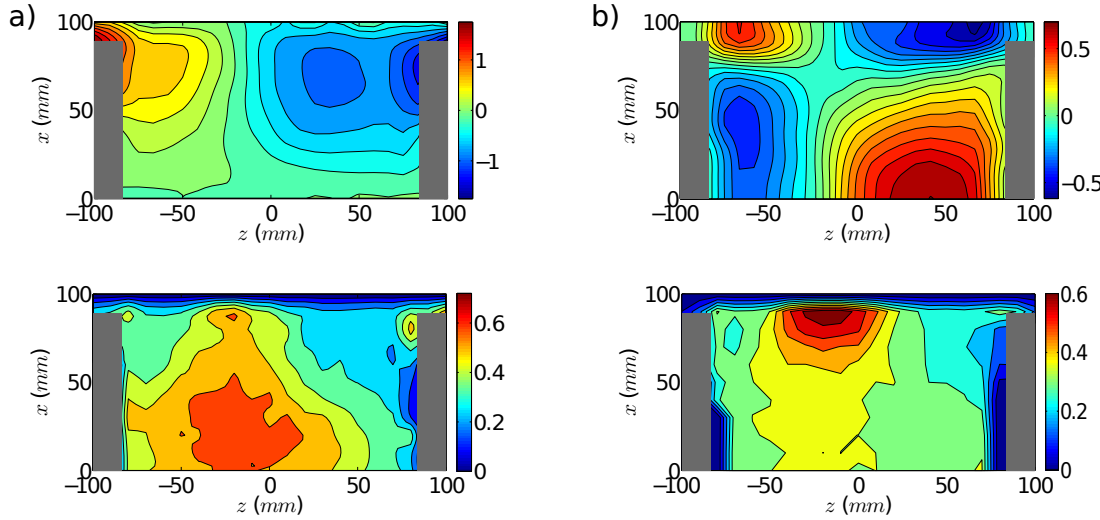


Figure 4.3: a) Average azimuthal velocity (U_θ) and fluctuations (u'_θ , bottom), color bar in m/s .
d) Average axial velocity (U_z) and fluctuations (u'_z , bottom), color bar in m/s .

To represent the flow through one of the states and in accordance with the Reynolds decomposition ($\mathbf{v} = \mathbf{U} + \mathbf{u}'$), we computed the mean field $\mathbf{U} = (U_r, U_\theta, U_z)$ and its fluctuations $\mathbf{u}' = (u'_r, u'_\theta, u'_z)$, through very long measurement series compared with the Kolmogorov time scale. In Fig.4.3 we show the mean flow measured via LDV in a half of the equatorial plane of the cylinder and its fluctuations, in this representation it can be observed basically two toroidal recirculation's, wherein the peculiar characteristic of this flow unlike others measured in similar

configurations, is that here the shear layer is displaced ($\sim 2\text{cm}$) to one of the impellers until a reversal occurs and goes to the opposite side. This instability is very sensitive to changes in Δ , or to another dissymmetry as the pressure gradients. In one experimental run a mistake was done during the assembling of the cell, and the caps were badly sealed, leaving a small hole between the joint on the clamps. In that case a pressure difference and a small global recirculation was created, and the system remained in only one state and non reversals were observed.

Once we have measured with the LDV the components v_θ , v_z , now we are capable to compute the v_r component using the continuity equation as described above. In Fig.4.4 we report the 2D mean field reconstructed with the LDV (blue vector). In this mean field the two toroidal recirculation's are more marked than in the single component contour map and here it is possible to observe the stagnation point in where should be the most isotropic zone in the flow. Also in this figure, we compare the results reconstructed using LDV against the 2D vector map measured with the PIV (red vectors) and a good agreement can be appreciated between both methods. In this figure the position of the shear layer where the toroidal flows collide, is in both cases displaced around 2cm to the left.

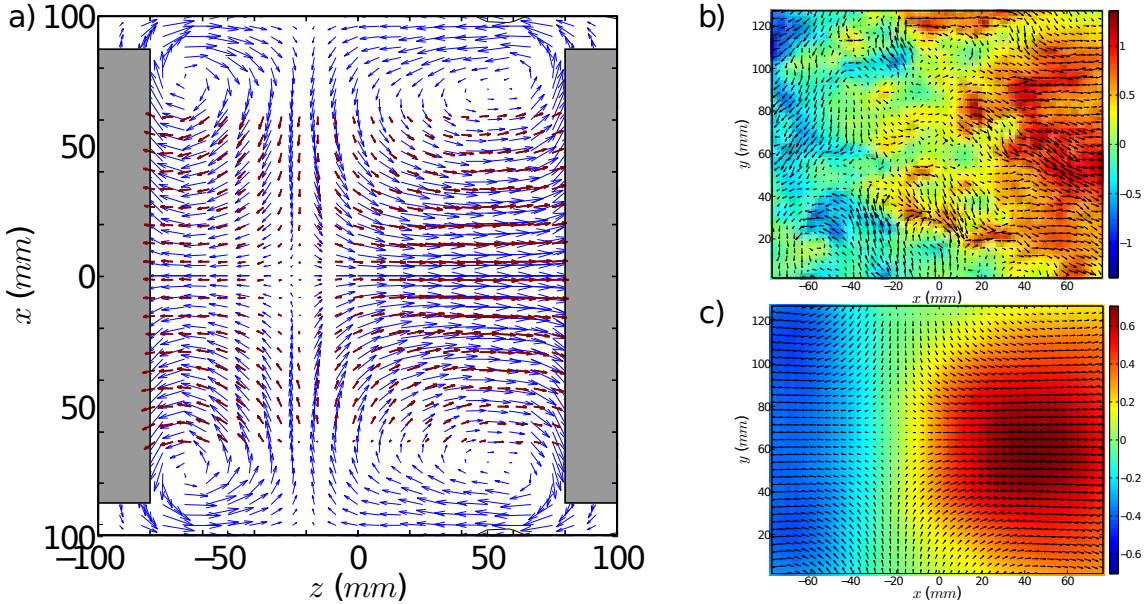


Figure 4.4: a)The blue vectors represent the mean field reconstructed from the LDV measures, respectively the red vectors represent the mean field measured using PIV. b) Single vector map obtained from the measured with PIV. c) Contour plot of the axial component.

As an example of the instantaneous behavior of this turbulent flows, we would like to present in Fig.4.4.b, how a single vector map looks taken from the flow using the PIV technique. We can see that large vortical structures are found, and no signal of the average flow can be appreciated. Also, to distinguish that for this case the shape of the shear layer is ambiguous. The data presented in fig.4.4.a is the average of 1500 instantaneous vector maps. From there we can see again the displacement of the position of the shear layer (see fig.4.4.c).

4.1.2 Comparison with other results

In order to compare our results, we can recall similar results that were reported by Marie et al.[62], where they showed that the shear layer was slightly displaced in the mean velocity fields, or at least their position was not clearly placed at the mid plane. To obtain the mean velocity fields, they used a vertical configuration with a “TM 51” propeller type and their measurements were done using a LDV system. Something similar happens with the mean velocity fields measured by F. Ravelet[71], also in this case, it can’t be appreciated a well defined shear layer at the middle. Nevertheless, these assumptions are highly debatable since there is not a procedure to evaluate the symmetry of the velocity field and on those propellers the deviation of the shear layer was very weak.

Moreover, in recent publications[65, 73] –based on a similar vertical setup– has been reported that at large Re numbers, time intermittencies between metastable states appear, breaking the symmetry of the system. They also observed residence times of the order of tens (in some cases, hundredths) of seconds, and during that time the shear layer should be displaced from the geometrical center.

In Fig.4.5 we compare their results and our mean field measured with a very similar set of fixed parameters. In both cases, a small dissymmetry was imposed ($\Delta \sim 0.005$), both are in the fully developed turbulent regime, although they have different aspect ratios and propellers. We can see that in both cases a displacement of the shear layer can be observed, but certainly both preserve the classical recirculation’s described above.

Finally just recall that also in the thesis of R. Monchaux[64] (the same setup as [65], with $\Delta = 0$) a displacement can be appreciated in a mean vector field averaging with 150 vector fields ($\sim 10sec$) in where the shear layer is not placed at mid plane, in its research the shear layer appear in the mid plane until a 5000 averaging vector fields ($\sim 5min$) was recorded.

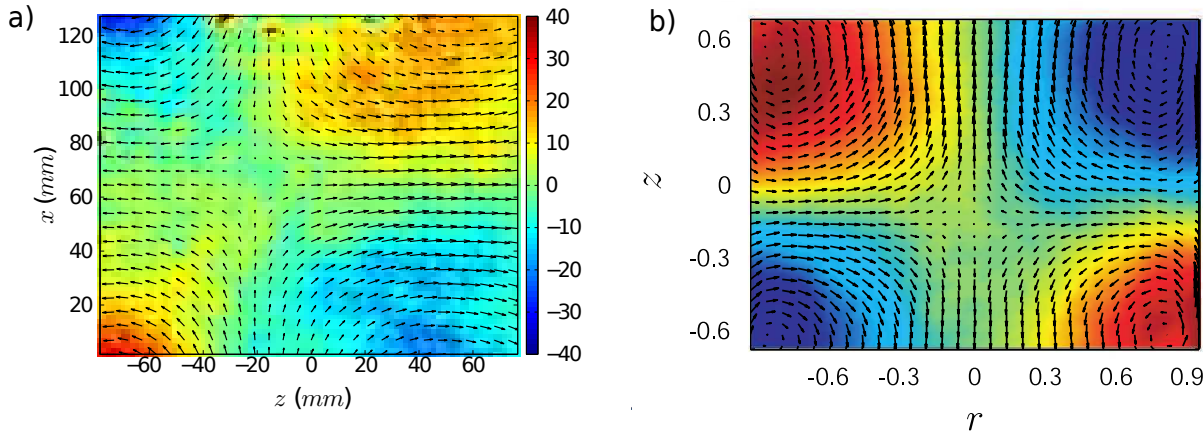


Figure 4.5: a) Mean vector field obtained with 1500 PIV vector maps (150sec), with $\Delta = 0.005$ and $Re = 1.74 \times 10^5$. b) Mean vector field obtained with PIV in a different setup (from reference [73]), with $\Delta = 0.0036$ and $Re = 8.9 \times 10^5$.

4.1.3 Discussion about the position of the shear layer

By definition, the average value of a random variable is computed taking the mean value over a large set of realizations. In the ideal case, this set of realizations will cover all the possible values of the variable. But the problem arises when we need to compute the average value of a variable where many different dynamical behaviors appear combined.

Here we have different dynamics: the reversals, the small scale turbulence, and other slow dynamics as the ones presented in chapter 6. We should be careful, because depending on the way this average is computed, we can recover a mean field that has not physical meaning, in the sense that the system never states in that situation. In the case of turbulence, this could have a very important impact for example at the moment of trying to describe a scale (temporal or spatial) that contains most of the kinetic energy involved in the flow.

In our case we have decided to use the average flow computed over a state with the displaced shear layer. In that way, our mean field averages all the small scale turbulent fluctuations, and also retains the symmetry breaking of the solution. The fluid remains for long periods in that situation, compared with the case where the layer stays on the middle that appear only as a transient and not as a stable solution.

Although the characteristic time of each one of these solutions will depend on the exact values of the experimental parameters, since the residence time will be always larger than the characteristic time of the injection and it would be possible to verify the appearance of slower frequencies on the system with these solutions.

In conclusion, we would like to define our mean field as the time average of a set of instantaneous solutions for a period of time larger than the injection time scale, but smaller than the reversal time. In fig.4.6 we show our interpretation of the mean flow, in where two possible real cases were obtained and other related to the transient between them.

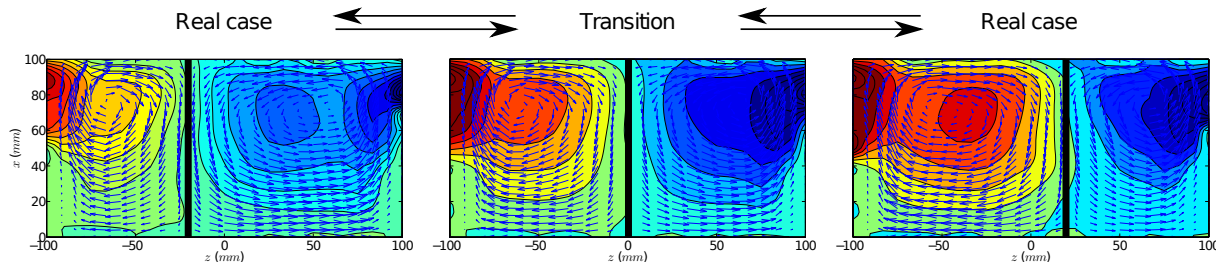


Figure 4.6: Scheme of the transition between the real cases.

4.2 Inertial and viscous forces independence on the Re number

It is well known that the behavior of the relationship between inertial and viscous forces is fundamental for the transition to turbulence. When these forces appear at different scales, i.e. the viscous forces become negligible for larger sizes whereas the inertial forces dominate, the flow is considered to be in the fully developed turbulent case. According to the Reynolds number

similarity, the flow will preserve its characteristics once the turbulent regime has been reached. In particular, we would expect that once this regime is reached, the flow should scale with the propeller's frequency, as this parameter governs the energy injection on the fluid. So, if the velocity scales with the Reynolds number, the energy injected in the system will be proportional to:

$$E \sim \frac{1}{2} M U^2 \sim \rho L^3 L^2 / T^2 \sim L^5 / T^2$$

and the dissipation rate (the energy dissipation rate per unit volume), proportional to the injected power:

$$\varepsilon \sim \frac{1}{L^3} \partial_t E \sim L^2 / T^3 \sim \Omega_{prop}^3$$

as the fluid velocity depends only on the propeller frequency, i.e, the Reynolds number. In Fig. 4.7 we present this behavior, and it can be observed how this magnitude evolves as Ω_{prop}^3 .

Coming back to the mean flows, their general characteristics should be independent from the Reynolds number, once they have been renormalized. In our case, we measured different mean velocity fields for Reynolds number from $Re = 8.7 \times 10^4$ to 4.35×10^5 to characterize the large scales in the VKP flow and no differences were appreciated. For isotropic turbulence the rate of change of the spectral function is [86]

$$\frac{\partial E(\kappa, t)}{\partial t} = -2\nu\kappa^2 E(\kappa, t) - \frac{\partial}{\partial \kappa} S(\kappa, t) \quad (4.1)$$

In this equation $\frac{3}{2}S(\kappa, t)$ is the flux of kinetic energy between the different scales, and the large eddies will contain the major of the kinetic energy, nevertheless they contribute less to the viscous dissipation. A term that is missing in this expression is the injection term, the power source that appears only for the large scales. This term will be independent on the Reynolds number, because it depends on the geometrical properties of the problem and not on the frequency of the propeller.

Now if analyze this expression in its a non-dimensional form, using as spatial dimension the Kolmogorov scale defined in eq. 2.20, the dissipation will appear in the same position, so the only effect in the spectrum will be the increment of the inertial range, and the energy injection will appear for lower values of the power spectra, but the overall dissipation will remain unchanged. To validate this assumption we measured the energy dissipation rate for different values of Ω_{prop} , this variable will be in our system the parameter that controls the Re number and the results for four Re numbers are plotted in Fig.4.7. Although the presented data have dimensions, according with energy dissipation law ε should vary like U^3 for a fixed length and U vary linearly with Ω_{prop} ($U = 2\pi l \Omega_{prop}$). This means that in our experimental setup for the used Re , the flow is independent of the Re parameter.

Furthermore, we measured the azimuthal velocity close to the wall for several Reynolds numbers and some of them are presented in its dimensionless spectrum form in the Fig.4.8. In the figure at the left we present the measurements that were made for low Re (Re not used for the characterization), where we can see how the spectral densities doesn't collapse, meaning that the behavior of the flow depends of the Re . However for large Re (Re used for the characterization, presented on the right), no differences were appreciated in the range of the large scales. Also, in this figure we can observe how the only part of the spectrum that differs is the tail of the spectrum

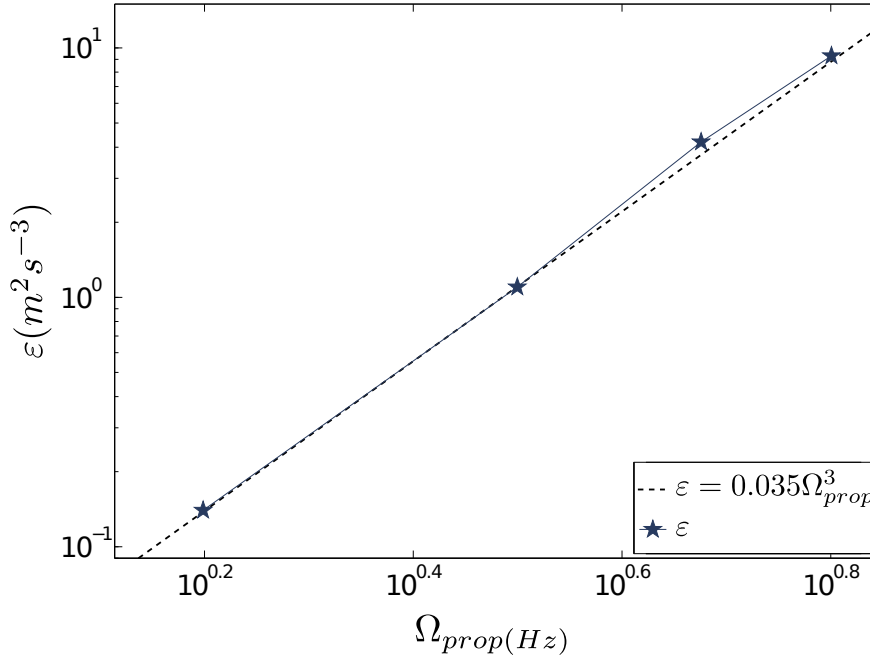


Figure 4.7: Log-log for energy dissipation rate in function of the injection frequency. The dash line represents a power law of the power dissipation versus the rotation frequency.

for large κ and for the lowest Re . In our research, this won't have a great impact, because the scales that we are interested in are the ones that are slower than the injection.

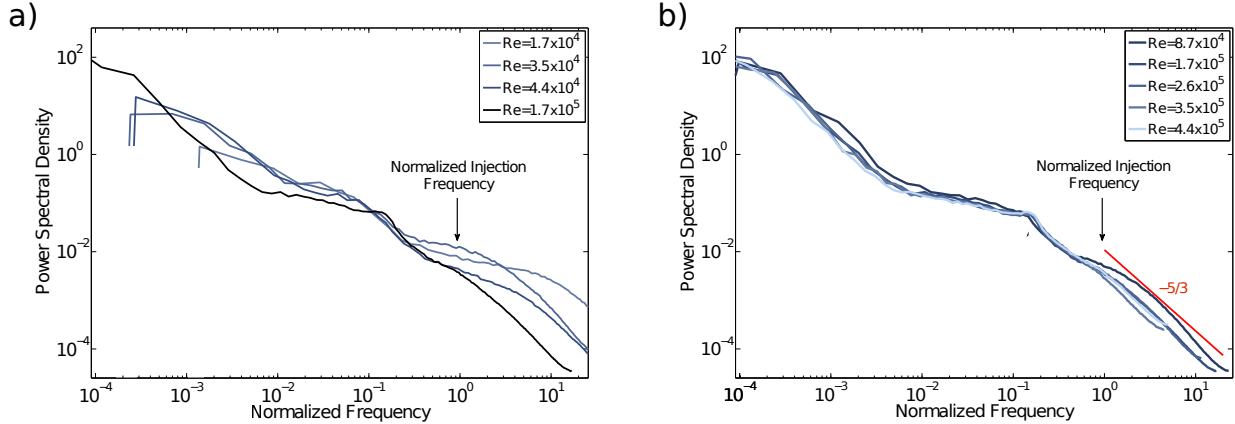


Figure 4.8: a)Normalized spectrum density for low Reynolds. In solid blue we present the PDF of the most used Re value b)Normalized spectrum density for large Reynolds.

We have plotted in Fig. 4.9 the PDF's of the velocity series whose spectra have been presented in Fig.4.8 (the blue histogram correspond to the Re used for the characterization of the large scales). The difference between the measurements at low Re and large Re can be appreciated in the strong dependence of the distribution in function of the Re . This figure shows that for low Re numbers the PDF is almost Gaussian and for larger Re numbers the PDF becomes asymmetric.

An study to recover the characteristics of the PDF's for large Re in the system was done by

[85]. In that work they showed how the system is jumping among three states (A_0, A_N, A_S). They suggested a toy model whose aim was to reproduce the behavior of the azimuthal component at the same position on the cylinder ($x = 0.9\text{cm}, y = 0, z = 0$). The model was based on a three well potential[5, 85]:

$$\dot{v}_\theta = \epsilon v_\theta + gv_\theta^3 - v_\theta^5 + \sqrt{2B}\xi(t) \quad (4.2)$$

Our contribution to this approach has been to improve the statistics that describes the dynamic of the reversals of the flow and increase the range of analyzed Re numbers. We present a wide study of the relative amplitudes in Fig.4.9.b. Here we explored a range of Re numbers between $2 \times 10^4 - 7 \times 10^5$ and no differences were appreciated.

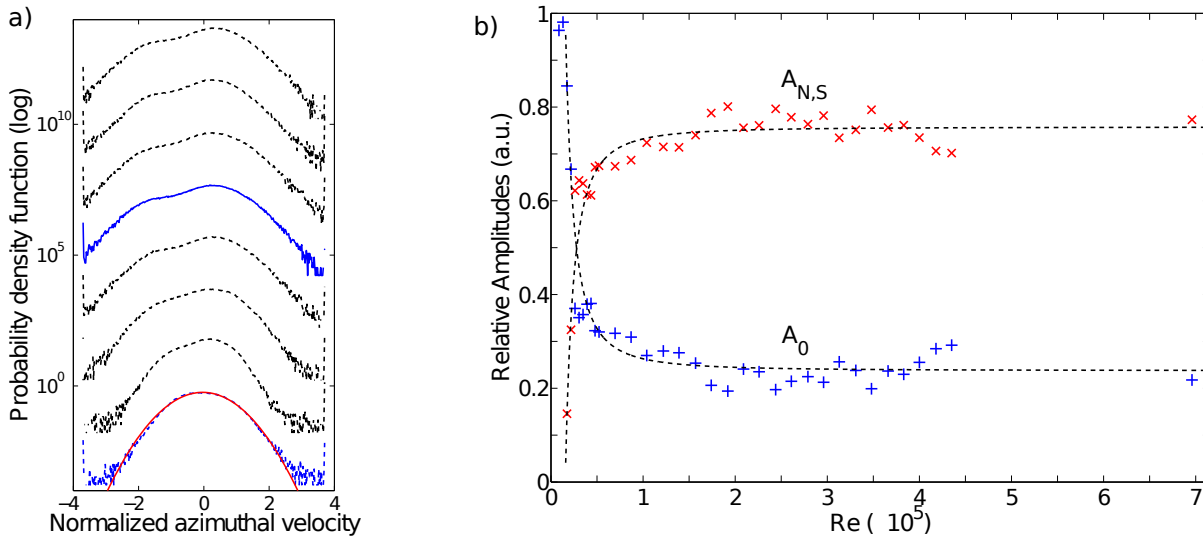


Figure 4.9: a)PDF of v_θ measured in $x = 0.9R$, $y = 0$, $z = 0$ for different Re . b)Experimental relative amplitudes versus Re .

We have talked about self-preservation (or similarity) from the spectral point of view, however the principal assumption of this statement refers when the dynamical behavior (or any other value) can scale using a single parameter. In other words, if we increase the rotation frequency (value of velocity) of the propellers, the mean profiles between the cases where the flow remains in a fully turbulent regimen won't change, only the profiles will re-scale. We tested this assumption, computing the mean profile for different Re number in the fully turbulent regime and no differences were appreciated. In Fig.4.10 we present the mean field and its fluctuations for a $Re = 4.23 \times 10^5$, in this figure we can observe that also the mean profiles doesn't change (comparing with Fig.4.3) for different Re and only the absolute values of the velocities need to be re-scaled.

Noteworthy that this proof of the self-preservation is only one evidence more to support the idea of the Re independence, since in some setups this simple picture has been demonstrated to not to be valid.

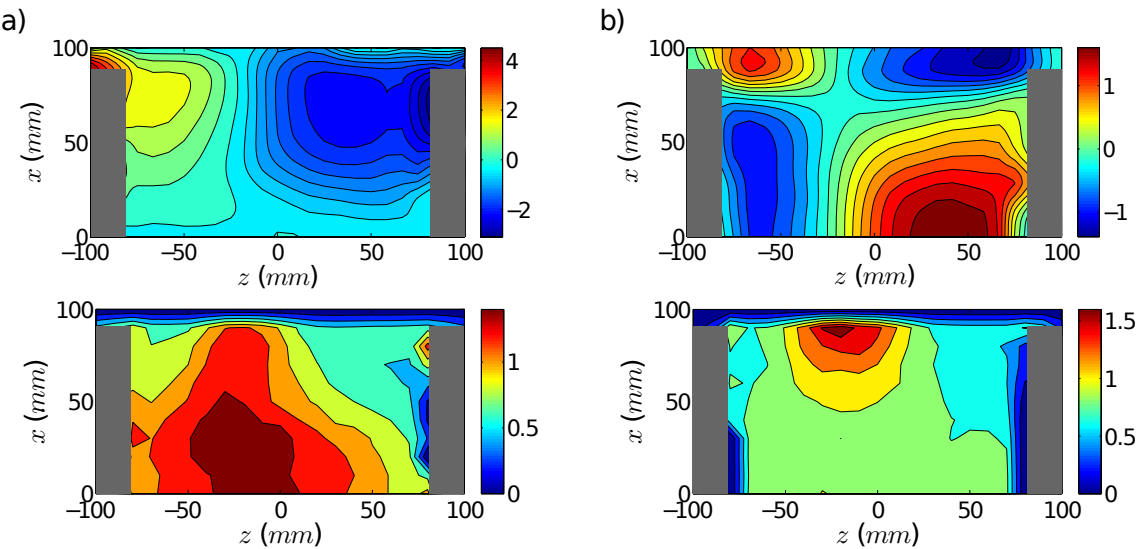


Figure 4.10: a) Average azimuthal velocity (U_θ) and fluctuations (u'_θ , bottom), color bar in m/s .
d) Average axial velocity (U_z) and fluctuations (u'_z , bottom), color bar in m/s .

4.3 Modifying the experimental configuration: Mean-flow consequences

During this research, some questions about the origin of the displacement of the shear layer far from the mid plane have lead us to think that this mechanism consists on the preservation of some magnitude that is transferred between the impellers. On the other side, a previous work on the same setup showed that the shear layer could be placed at the equator if a random but very small fluctuation of the impeller's velocity is artificially introduced [85]. All this evidence points to a very sensitive transfer of some magnitude that is placed in a unstable equilibrium, so the system has two meta-stable solutions. Any small disturbance will destroy this dynamics pushing the system to fluctuate around the mid plane.

These fast fluctuations of the shear layer should be observable in other magnitudes. For example in other configurations has been proved that the fluctuations in the power consumption of the propellers are quite strong[87], meaning that the fluid is braking and pushing the angular velocity of the propellers, which in turn means that the energy injected is not constant. To avoid this problem in our system, we over-designed both the total power delivered by the motors and the total inertia of the system, giving a high stability to the propellers (previously de la Torre et al.[85] reported for this set-up an standard deviation of the order of 0.1%).

Considering the ideal assumption that in our case (shrouded flow) the injected energy are not having losses because of the slow-down of the propellers or due the walls and the only mechanism involved in dissipate such energy are the small eddies. We thought that a way to release some energy would be open the caps in the cylinder leaving that the whole volume of fluid interact with the environment, approaching with this, to cases in where losses of energy are due the slow-down of the propellers.

The results are showed in the Fig.4.11 in where a clear shear layer situated at the mid plane is reported, this mean field is similar to the ones previously reported by other groups and serves as an argument to validate that the principal difference between the set-ups are either the stability

or the inertia. If we now compare the fluctuations between the two configurations (Fig.4.12), we can see that the extension of the fluctuations are more intense in the shrouded case than for the free case, meaning that the dynamics involved are more intense in one case than in the other. This result would be a good candidate to be studied deeply varying the volume to see the influence of the energy injection on the medium.

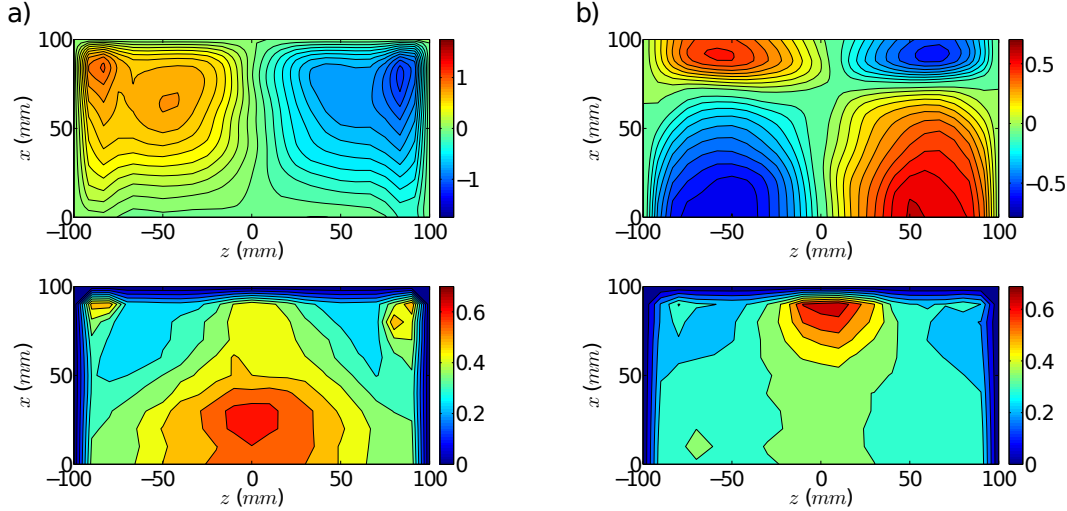


Figure 4.11: a) Average azimuthal velocity (U_θ) and fluctuations (u'_θ , bottom), color bar in m/s .
d) Average axial velocity (U_z) and fluctuations (u'_z , bottom), color bar in m/s .

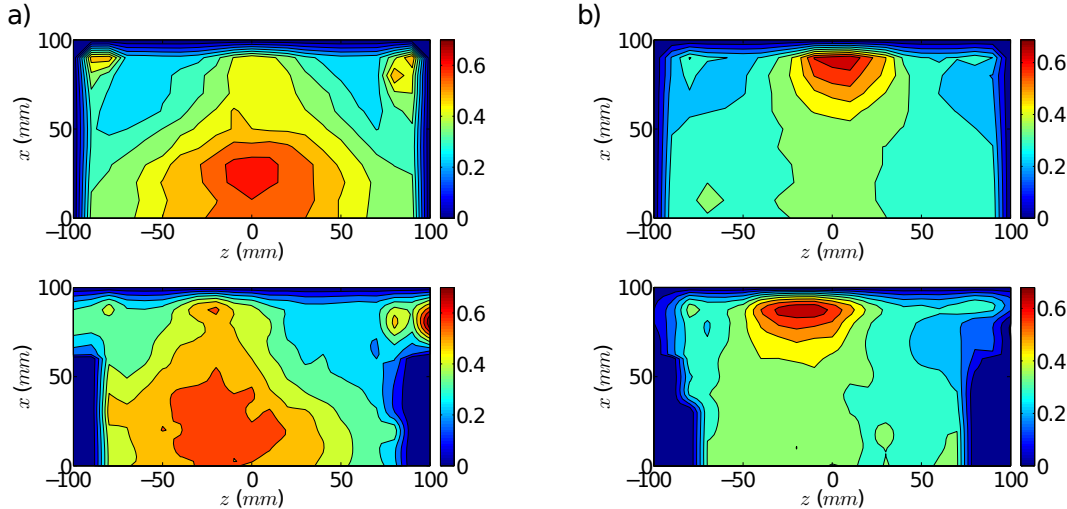


Figure 4.12: a) Comparison between the fluctuations of the azimuthal velocity for the cases with and without caps. b) Comparison between the fluctuations of the axial velocity for the cases with and without caps.

4.3.1 Velocity profiles

To give another perspective of the difference between these dynamics, we plot a short period of the normalized velocity signals at the center of the cylinder and close to the wall ($x = 0, y = 9cm$)

for the two symmetric cases (see Fig.4.13.a,b) where the cylinder is closed and for the free flow case (see Fig.4.13.c). In the symmetrical cases, the velocity values are fluctuating between the 0 and ± 0.5 –respectively the N and S cases. But for the free flow case the values are jumping from positive to negative values and in some intervals even remaining tens of seconds. This local difference are the direct responsible of the position of the shear layer and later we will discuss briefly the dynamics for the free flow.

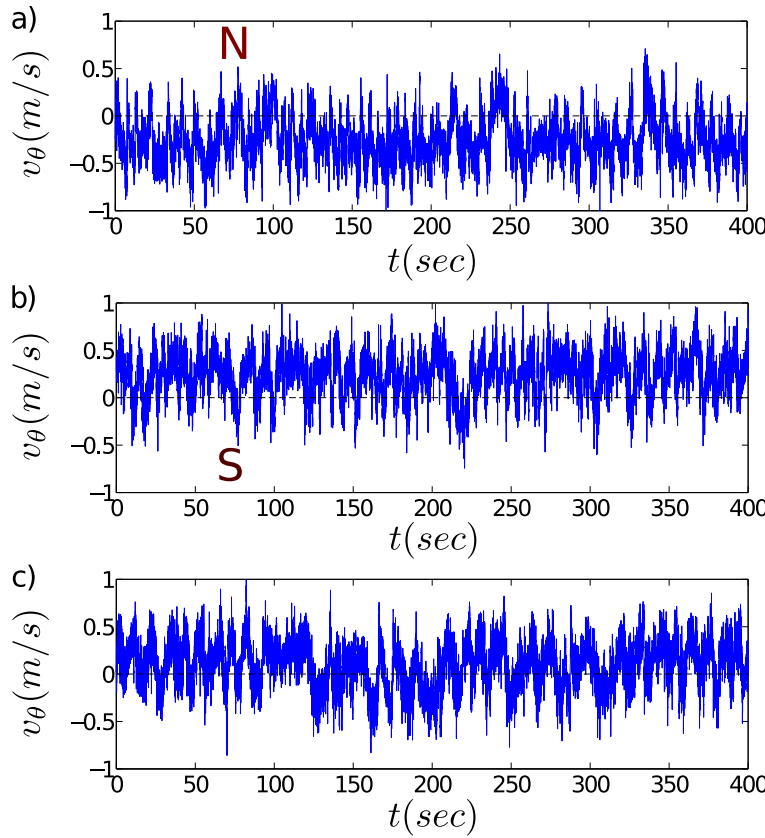


Figure 4.13: a,b)Normalized azimuthal velocity measured at $x = 0, y = 9\text{cm}$ for the N and S states. c)Normalized azimuthal velocity measured at $x = 0, y = 9\text{cm}$ for the free flow case.

5 Description of the turbulence characteristics

Resumen

Se ha mencionado que la imagen clásica de la turbulencia reúne un amplio rango de escalas, empezando con la escala en donde la energía es inyectada al flujo, hasta escalas en donde los elementos de fluido comienzan a convertir dicha energía en calor (escala de Kolmogorov). En este rango de escalas es en donde la teoría ha puesto casi toda su atención durante los últimos años, dejando abierta la pregunta de cuales son los mecanismos que acoplan las diferentes escalas. También ha intentado comprender los factores que afectan a los parámetros estadísticos de los flujos analizados, además de proporcionar algunas correcciones a su interpretación.

En este capítulo presentamos una imagen cuantitativa del flujo turbulento, intentando abarcar todas las dinámicas que están afectando esta caracterización. No obstante la teoría actual asume un comportamiento ideal de estos parámetros y quizá algunos otros factores que pueden afectar no hayan sido considerados y puedan dar lugar a discrepancias. Estos parámetros pueden permitirnos comparar nuestra investigación con otros sistemas experimentales y también para encontrar diferencias entre el flujo turbulento dentro de nuestro tanque con la turbulencia isotrópica y homogénea (turbulencia ideal).



Figure 5.1: Different scales and vortices in a drawing by Leonardo Da Vinci.

Abstract

It has been mentioned that the classical picture of turbulence gathers a wide range of scales, from the scale where the energy is injected in the flow, to the scale where the fluid elements dissipate such kinetic energy into heat (Kolmogorov scale). It is in this range of scales where most of the research has been focused during the past years, leaving unanswered the question about what is the mechanism that couples the different scales. Also, the current theory has tried to determine the different factors that affect the statistical parameters of the analyzed flows, as well to give some corrections to their interpretation.

In this chapter we will present a quantitative picture of the turbulent flow, trying to address all the dynamics that affect this characterization. Nonetheless most of the predictions of the present theory are valid for ideal situations (isotropy or homogeneity) and some other factors (as anisotropy or inhomogeneity) that can be at the origin of some discrepancies have not been considered. These parameters allow us to compare our research with other experimental set-ups and also to find differences between the turbulence inside our tank with an isotropic turbulent flow (ideal turbulence).

5.1 Description of the turbulence characteristics

As it has been explained above, the flow that is present in this experimental setup is in a fully developed turbulent regime, with Reynolds numbers (based on the experimental setup and the control parameters) as high as 10^6 . It is very well known that in this regime vortices with sizes ranging from tenths of centimeter to tenths of micrometers should appear. In other words, a broad range of wave numbers can be excited simultaneously. A correct analysis of the turbulent flow; with a complete description of their spatial statistics, will cover this whole range of wave numbers. For Reynolds numbers of 10^6 , we could expect at least two orders of magnitude in the inertial range in the spatial spectrum. That implies that using our experimental setup a simple PIV analysis won't be enough, as it is limited to less than two orders of magnitude (velocity fields of 100x75 vectors).

In the other side, we were also interested on the large-scale behavior of these velocity fields. We wanted to verify, whether the fluctuations had a long-time dynamics associated to a large spatial vortical structure. For a purely turbulent flow without slow dynamics, the average of the fluctuations should vanish when these mean values are obtained for times larger than the injection time.

With all these ideas in mind, we decided to measure PIV velocity fields with different fields of view. Using this approach, we could build a larger wave number range via overlapping these spectra. Our setup uses three different fields of view, in such a way that each spectrum overlaps the neighbor at least a 50% in logarithmic scale. Concerning the temporal behavior, these velocity fields were acquired for times much longer than the injection times.

Finally, we decided to quantify the scaling of the statistical magnitudes of the turbulent flows using different tools, in such a way that the results can be validated using data coming from other techniques, and so the potential sources of error can be avoided / removed. We used velocity

fields coming from PIV measurements, but also from LDV series using the Taylor hypothesis as described above.

The parameters were estimated according to the Kolmogorov's theory[2], which explains that the average dispersion of energy for an incompressible fluid can be obtained from the second order structure function (eq.2.25) –assuming that the flow is homogeneous and isotropic–. The two main variables that have been computed are the longitudinal second order structure function $B_{dd}(r)$ and the 1D auto-correlation function $R_{xx}(r)$. Each one of these variables was obtained using a set of PIV velocity fields (Eulerian measurements), wherein each set contains between 1500 and 2100 vector maps.

All the results presented in this chapter concern the ones obtained in the intermediate field of view and in some specific cases the smallest. These fields were measured in a meridional plane in a region centered around the axis. The position along the z -axis ($r = 0$) is fixed in such a way that the field of view contains the average position of the shear layer. In our case, this is the place where the more isotropic results are expected in this turbulent flow. Other regions would be affected by the propellers, and here the dynamics is dominated by the collision between the two helical flows.

These data are recorded with a field rate acquisition of 15 fps and a field of view of $48 \times 36\text{mm}$ (for the case in light blue, a supplementary and similar field of view was measured to improve the results). The turbulent parameters that we obtained are presented in the table 5.1.

The same results can be obtained from the third order structure function (eq.2.26) given by Kolmogorov[3]. In this case to obtain $B_{ddd}(r)$, the measurements were made with the LDV in different places. For these series a data acquisition rate of $0.9 - 2\text{kHz}$ was used during a period of almost five minutes. The difference between these two ways to obtain the average dissipation of energy for these simple cases is small, since both measurements bring very similar values of ε .

f_{prop}	u'_θ	Re	l_{int}	ε	η	τ_η	λ	R_λ
Hz	m/s		mm	$\frac{\text{m}^2}{\text{s}^3}$	μm	ms	mm	
1.58	0.24	8.70×10^4	17.8	0.1	51	2.60	2.5	596
3.16	0.5	1.75×10^5	16.4	1.1	31	0.98	1.9	923
4.74	0.8	2.61×10^5	15.5	4.2	22	0.48	1.5	1195
6.32	1.1	3.48×10^5	14.9	9.3	18	0.33	1.4	1537

Table 5.1: Turbulent parameters. f_{prop} :Propeller frequency rotation; u'_θ :Velocity fluctuations in the shear layer; L :Integral length; ε :Energy dissipation rate per unit mass; η :Kolmogorov length scale; τ_η :Kolmogorov time scale; λ :Taylor-microscale; R_λ :Taylor-microscale Reynolds number.

5.1.1 Experimental turbulent parameters

It is important to note that these values can be influenced by many external factors like the noise in the measurements, the absence of the third component, the possibility of low statistics, etc. However, we will try to give a brief explanation of how each turbulent parameter was obtained, with the purpose of giving the whole picture. Some algorithms used to obtain these values were taken from [88] and others were home made. When possible, we have compared the results of

both approaches.

The way how we determine experimentally the integral length of our system, was based on the correlation function, that according with Pope [1] can be defined as:

$$l_{int} = \int_0^{r_x} R_{xx}(r) dr \quad (5.1)$$

where R_{xx} was defined in chapter 2, eq. 2.16 and r_x is the maximum distance available to compute the auto-correlation from our measurements. For data correlated at large distances, the difference between the magnitude defined in this way compared to the one defined in eq. 2.15 can be important because of the different integration limits (∞ vs. r_x). But in our case; and even more important, if the auto-correlation decays exponentially, the computation of this integral scale becomes very easy because in that case:

$$l_{int} = \int_0^{\infty} R_{xx}(r) dr = \int_0^{\infty} e^{-r/l_{int}} dr \quad (5.2)$$

and the integral scale can be computed from the slope of the data in semi-logarithmic scale.

Using the mean fields, we obtained the correlation function for different Re and the data are presented in Fig.5.2. Using the above definition, we may increase the error because of the influence of the low statistics between at large distances. In order to improve the definition of the integral scale and to avoid the problem of low statistics, we use a Levenberg-Marquardt method to fit the correlation function obtained from the experimental data for different lengths and therefore, the integral length scale reported is the result of averaging all the integral lengths obtained from the fit.

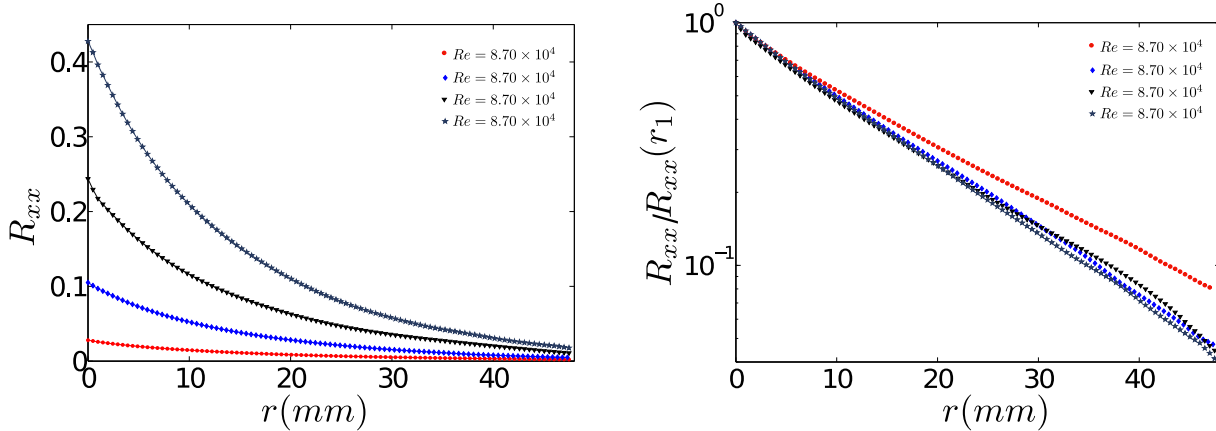


Figure 5.2: Left: raw correlation function for the experimental data reported in Table.5.1 without the rescaling of the u_{rms} as it is defined in 2.16. Right: the same data with $R_{xx}(0) = 1$ in semi-logarithmic scale.

It is important to note that in the right part of Fig.5.2, the auto correlation function for $Re = 8.7 \times 10^4$ (red dots) reveals that the system is not yet in the fully development regime as the other three are. In that regime we would expect an exponential decay, and it can be observed how the lowest Reynolds series deviates from that trend. A deeper analysis for that range of Reynolds numbers, close to the value where the instability described in the previous

chapter appears, remains as one of the open questions in this work. However, our aim was to explore the slow dynamics once this instability has appeared, and so we have explored Reynolds numbers larger than $Re \geq 1.75 \times 10^5$.

An important parameter in the theory of turbulence is the energy dissipation rate, that according to the Kolmogorov's theory for a homogeneous and isotropic fully developed turbulent flow, could be obtained from any of the different structure functions. Actually, from this theory we should expect a power law with different exponents on the spatial parameter r , being the prefactor a function of the dissipation rate. Nevertheless, it is well known that due to the intermittency that is a characteristic of turbulent flows; the real behavior of these parameters deviates from the prediction done by Kolmogorov. For that reason, the structure functions used to compute this parameter are those of second and third orders. And, of course, another reason to restrict the computations to the lowest orders is because the noise increases with the order of the structure function.

Nevertheless, it's important to note that in our case we don't have a region where the flow remains in the ideal case of homogeneous and isotropic turbulence, so basically the energy dissipation rate that we obtain from the data is just an estimation. Knowing this, we can now compute from the PIV velocity fields the second order structure function. These data are plotted in Fig.5.3.a. In the ideal case, and according to Kolmogorov's theory, the structure functions should evolve as[89].

$$\langle [v(x+r) - v(x)]^p \rangle \sim C_p (\varepsilon r)^{p/3} \quad (5.3)$$

The second order structure function would evolve as $r^{2/3}$ and the compensated variable $B_{dd}(r)/r^{2/3}$ should produce a plateau in the inertial range, the range where these expressions would remain valid. In our data this compensated plot is presented in Fig.5.3.b and from the maximum value of these data we obtain the value of the dissipation rate presented in the table 5.1, that is attained for a distance comparable to the integral scale.

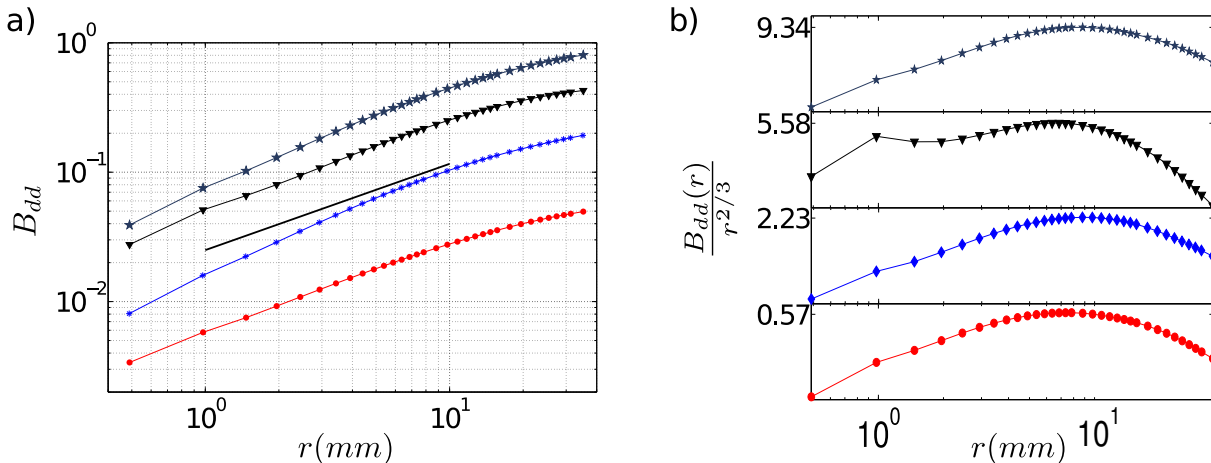


Figure 5.3: a) Log-log plot of the longitudinal second order structure function ($B_{dd} = \langle [v_z(z+r) - v_z(r)]^2 \rangle$) for different Re . The line in black represent a $2/3$ guide slope. b) The same data plotted in (a), compensated with the expected power law $r^{2/3}$.

We wanted to validate these data obtaining the dissipation rate from a different source. So

we follow an approach similar to the one proposed by Poelma *et al.*[90] to interpret the turbulent parameters using LDV. As in their case, we have found a good agreement between the results with PIV and LDV. The third order structure function was obtained using the LDV measurements at the shear layer, close to the lateral wall of the cavity. We must consider the local Taylor hypothesis to relate the temporal variation of the velocity with the spatial velocity differences. Assuming this, with a high data rate LDV acquisition, we can compute the third order function showed in Fig.5.4.a. From the expression eqn.2.26 deduced by Kolmogorov, we can obtain an estimation of the energy dissipation rate at the center of the set-up which is $\varepsilon = 1.09 m^2/s^3$. Furthermore, if we plot the normalized 3th order structure function displayed in the Fig.5.4.b we can observe the region in where the energy dissipation rate remains stable, this zone is localized almost in all the center of the graphic and only the extremes are influenced.

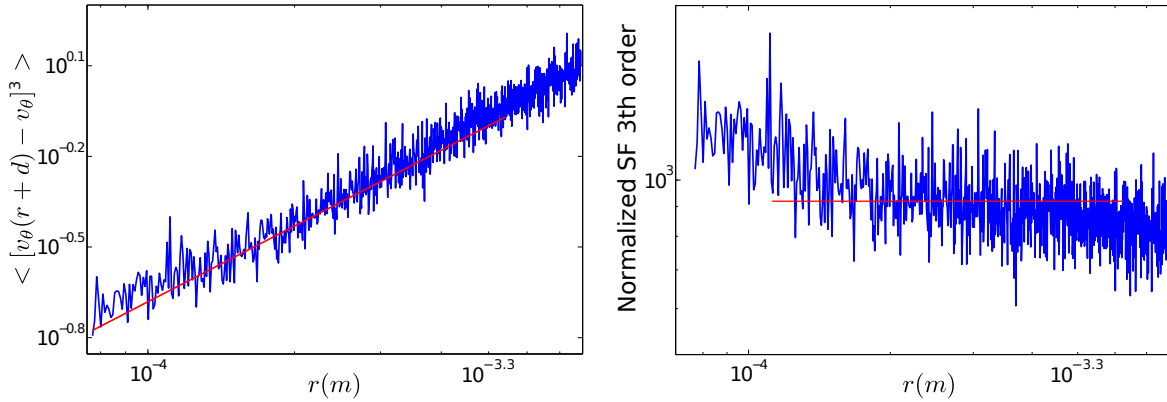


Figure 5.4: a)Log-log plot of the 3th order structure function ($B_{ddd} = \langle [v_z(z+r) - v_z(r)]^3 \rangle$) for $Re = 1.65 \times 10^5$. b)Normalized 3th order structure function.

5.1.2 Spatial distribution of the energy dissipation

As it can be seen from our results, the energy dissipation can be determined from the behavior of the variance of the spatial modulations at different scales. But, from the auto-correlation function we know that the integral scale is limited to roughly 15mm, so one question that arises is if this energy dissipation is spatially homogeneous in this turbulent flow. The answer to this question is clearly positive in the case of a homogeneous and isotropic flow, but in our case the flow is strongly inhomogeneous and anisotropic, and maybe the fluctuations behave similarly.

We could have obtained this spatial distribution of the energy dissipation using two different tools, the PIV and the LDV techniques. The best choice from the definition of the energy dissipation rate is the PIV, because from a direct measurement of the spatial fluctuations of the flow we can recover the value of ε . Nevertheless the experimental difficulties on implementing an accurate system to obtain the PIV vector maps in fields of approximately 20×20 mm, for different positions around the xz plane, were very important. On the other side, the measurement of the velocity series at different locations using the LDV tool was very accurate. In that case, the problem arises on the necessity of using some kind of Taylor hypothesis. Finally we favored this second option.

In fig. 5.5 we plot the third structure function (compensated, i.e. B_{ddd}/r) obtained for different z positions along a line parallel to the axis at $r = 9cm$. Two conclusions can be obtained from

this graph. First, close to the shear layer, were the flow is expected to be less affected by the propellers, we get a flat plateau, with a value of the dissipation rate ($\varepsilon = 1.1 \text{m}^2/\text{s}^3$) similar to those obtained for the same Reynolds. And second, close to the propellers the behavior of the fluctuations is strongly affected by the presence of this forcing. In that case the third order structure function does not growth so fast, and so the compensated plot has a negative slope.

In conclusion, we obtained a homogeneous value of the dissipation rate close to the shear layer, and no conclusions can be obtained about the behavior in the region near the propellers. A deeper study of these regions is necessary, and probably a PIV study of these regions will be compulsory.

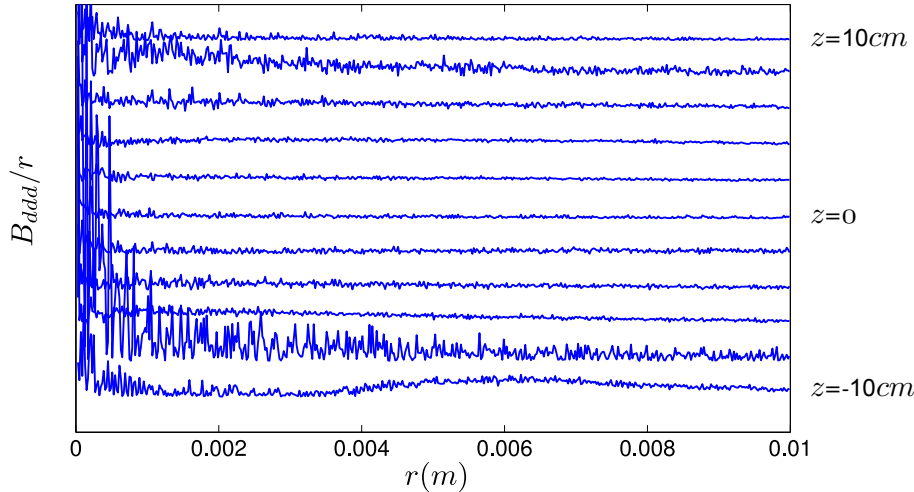


Figure 5.5: Third order structure function compensated (B_{ddd}/r) for different positions along the z axis and at a fixed radius ($r = 9\text{cm}$).

5.1.3 Intermittency: Does Kolmogorov need to be corrected?

From the LDV data obtained at the shear layer (the region where the turbulence seem to be close to the homogeneous and isotropic case) we can compute different structure functions. It is well known that, when Kolmogorov theory can be applied, all these functions should be power functions of the distance r , and their exponent should increase linearly with the order p of the corresponding structure function:

$$\text{exponent} \sim p/3$$

These exponents can be computed using the structure function defined as in eq.2.24, or a slightly different version:

$$\langle |v(x+r) - v(x)| \rangle^p = \int_V |v(x+r) - v(x)|^p dx \quad (5.4)$$

where the moments are computed using the absolute value. The advantage in this later case is that the noise is dramatically reduced, but the correspondence between both expressions can be done only in the case of homogeneous and isotropic turbulence [89].

When we compute these expressions (eq. 5.4) of the structure functions for different p orders (shown in Fig.5.6, left) we see how the exponents (Fig.5.6, right, red diamonds) deviate from the ideal case (Fig.5.6, right, blue straight line). These measurements were done close to the lateral

wall, but at the shear layer. The same computations were done at the axis ($r = 0$), but in that case the data set size is much smaller and consequently the statistics is not very good for structure functions of order larger than $p \leq 3$.

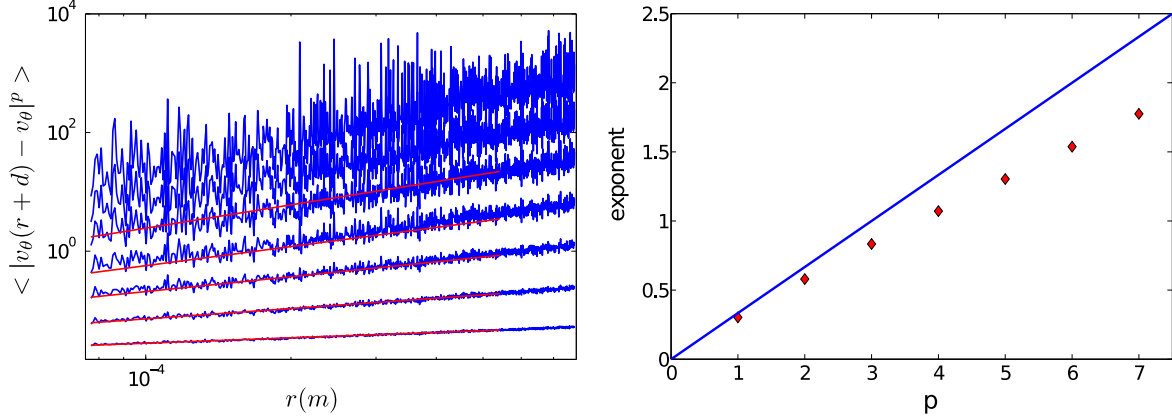


Figure 5.6: a) Log-log plot of the “p” order structure function ($B_p = \langle |v_z(z+r) - v_z(r)|^p \rangle$) for $Re = 1.65 \times 10^5$. b) Variation of the exponent of the order structure function.

Recent studies[91] in a similar configuration, show that the statistical values of small scales may be affected by the asymmetry of the large scales. For this reason, Ouellette et al. propose a correction for the Lagrangian structure scaling constant C_2 in which the anisotropy takes place. In our case, for the interpretation of the turbulence parameters shown in Table5.1, we decided to assume that the region where the measurements were made is isotropic and homogeneous. Therefore, we have taken the well accepted value –giving by Sreenivasan[92]– of $C_2 = 2.1$, leaving the question of the level of uncertainty, in the calculation of these values.

Usually the difference presented in Fig.5.6 is explained because of the “intermittent” behavior of turbulent flows, that introduces some corrections on the prefactors k_p that appear in eq. 5.3. A deeper study of the dependence of this deviation remains to be done. Finally, we would like to signal that the exponents obtained for orders larger than 3 are different whether the absolute value is taken into account or not. This could be due to the fact that the flow is not completely isotropic nor homogeneous.

5.1.4 Anisotropic and inhomogeneous flow

Almost all of the theory of turbulence has been designed to explain the properties of turbulence in a homogeneous and isotropic perspective, but this ideal case can only be achieved in a few real cases and in very specific zones. In this specific von Kármán experimental set-up was demonstrated some years ago that large scales fluctuations are important, and as a consequence the flow at small-scales becomes anisotropic [91]. These inherent characteristics of the flow alter directly the expected parameters of turbulence, since in the classical theory these effects are not taken into account.

With this idea in mind, we looked for any anisotropy that we may find in our flow. Using the PIV measurements, we recovered the spectra of the different velocity components along different directions. If the systems can be considered isotropic at some scale range, we should recover the same spectra whatever the component and the direction is considered. On the other side, if

the system is anisotropic, we should recover this anisotropy when computing the corresponding spectra.

In Fig.5.7.a we show a contour plot of the logarithm of the spatial power spectra in 2D for the velocity components v_r, v_z . If the flow is isotropic, the contour lines should be parts of circumferences. We can distinguish two regions: the large scales, where the fluctuations are anisotropic, and the small scales, where the fluctuations are isotropic. The two black lines correspond to the wave number associated to the integral scale (the one that is close to $\kappa \sim 0.3$) and the Taylor microscale (around $\kappa \sim 3.5$). We may consider that the system is anisotropic until the Taylor microscale, and then becomes isotropic.

We can now compare the scales for which the system can be considered isotropic and homogeneous. From the spectra presented in Fig. 5.7.a, we conclude that the system is isotropic for scales smaller than 1.8mm. From the homogeneity of the fluctuations, we can consider that the system is homogeneous in a scale comparable to the integral scale (around 10-15mm) –see Fig.5.7.b. The map (Fig.5.7.b) correspond to the fluctuations that comes from the largest area measured, from where the large wave numbers are obtained revealing a great spatial inhomogeneity in the turbulence.

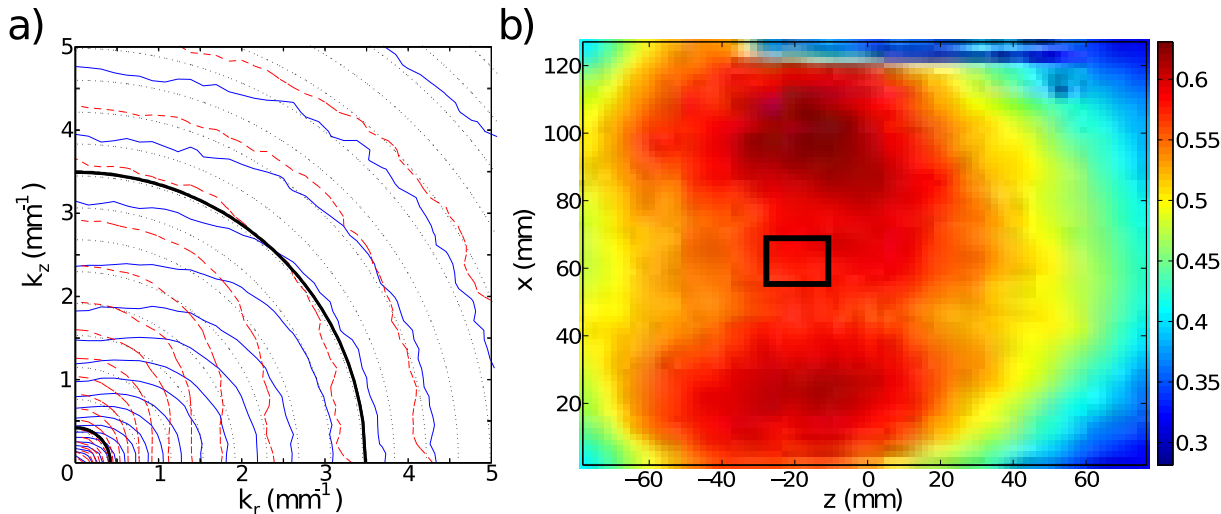


Figure 5.7: a) Contour plot of the logarithm of the power spectra of two velocity components v_r, v_z in a 2D plane. b) Fluctuations of the larger spatial plane acquired with the PIV.

6 Relevant slow time scales

Resumen

La aparición de grandes estructuras en flujos turbulentos y los mecanismos que generan estas estructuras no han recibido mucha atención en el pasado y la única certidumbre que tenemos acerca de estos fenómenos es su existencia. En la configuración VKP observamos en el dominio espectral diferentes escalas temporales mas lentas que la frecuencia de inyección. Estas escalas están asociadas a comportamientos bien definidos del flujo que aparecen para números de Reynolds muy altos ($Re = 8 \times 10^4 - Re = 7 \times 10^5$). Hemos identificado que estas escalas se corresponden con la aparición de estructuras tipo vórtices[56], inversiones del flujo [5] y al transporte del momento angular en un flujo turbulento de cizalla [48]. En este capítulo presentamos los resultados obtenidos para caracterizar estas escalas temporales lentas tanto cualitativamente en el flujo de von Kármán como cuantitativamente por medio de análisis espectral.

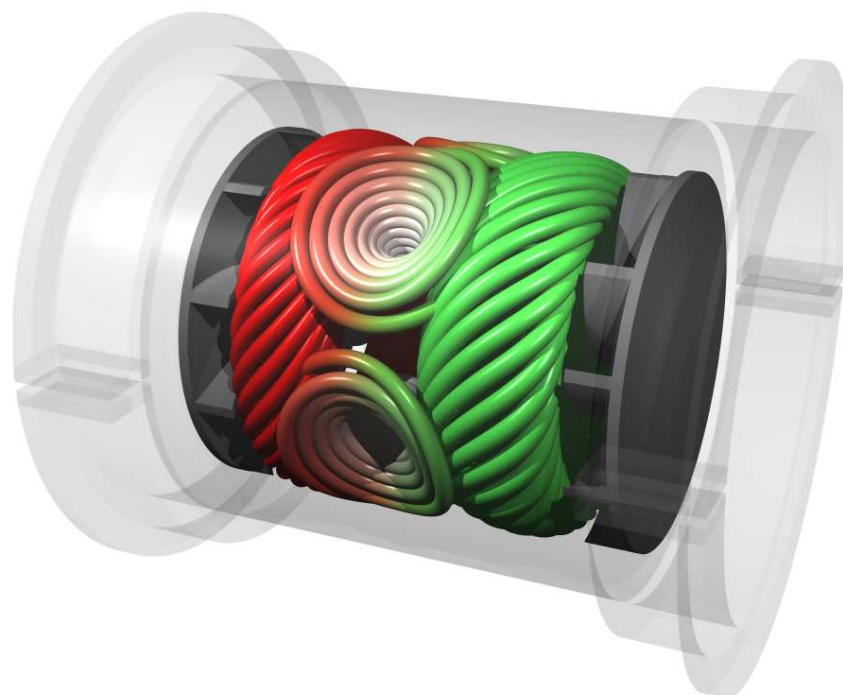


Figure 6.1: Representation of large vortical structures in a counter-rotating von Kármán swirling flow.

Abstract

The creation of large structures on turbulent flows and the mechanisms that cause such structures have not received much attention in the past, the only certainty about these phenomena is their existence. In the VKP configuration we observed different time scales in the spectral domain lower than the injection frequency. These scales can be associated to well defined behaviors of the flow that appear for large Reynolds numbers ($Re = 8 \times 10^4 - Re = 7 \times 10^5$). We identified that these scales correspond directly to the appearance of vortical structures[56], reversals in the flow[5] and the transport of angular momentum in a turbulent shear flow[48]. In this chapter we present the results obtained to characterize these slow temporal scales both qualitatively in the von Kármán flow and quantitatively via a spectral analysis.

6.1 The whole picture

First of all we would like to introduce the power spectral density of the azimuthal velocity – see Fig.6.2–, where different slow behaviors can be identified. These spectra were obtained from the azimuthal velocity (u_θ) close to the wall ($x = 9\text{cm}, y = 0, z = 0$) for time series at least two hours long. This position was selected because all the large scales present in the flow appear in this region.

To ensure that all these scales remain independent from any external control parameter in the fully developed turbulent case, we normalized the power spectral density for $Re = 8.7 \times 10^4$ up to $Re = 4.4 \times 10^5$ and the result is that all the lines collapsed. The spectra were normalized using the frequency of rotation and the azimuthal velocity of the propeller –see eq.6.1.

$$t_n = t \cdot f_{prop} \quad , \quad v_n = \frac{v}{v_{prop}} \quad (6.1)$$

We have said that this study is based on the slow behaviors, this means that we will focus on frequencies lower than the injection one. In Fig.6.2 we present five normalized power spectra for different Re numbers. An important observation between these experiments is that the features of the scales involved for slow frequencies are preserved whatever the value of the Reynolds number. So we decided to use a $Re = 1.7 \times 10^5$ for the characterization of the large scales.

In this chapter we will focus on the description of the different slow behaviors that appear on the VKP flow. In most of the cases we will analyze one of the states(N,S) suppressing the reversals, in order to simplify the study of the scales below the injection. It is in this region where the equatorial vortices appear and so does a $-1/3$ slope related with the slow movement of the shear layer.

6.2 Reversals (-2 slope)

It has been reported previously the existence of two symmetrical solutions that remain for long periods of time[5, 85]. In Fig.6.2 we show a clear -2 slope, that corresponds to the random reversals between these two flows previously reported by de la Torre *et al.*[5]. Also they studied the

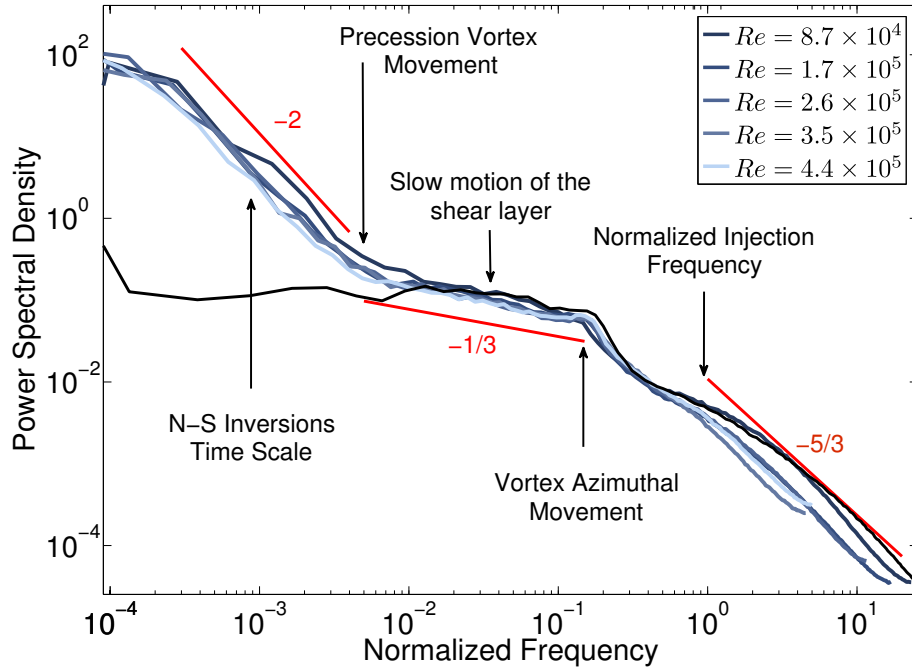


Figure 6.2: Power spectral density of v_θ at $x = 9\text{cm}$, $y = 0$, $z = 0$. The spectra are plotted for different Re .

hysteresis of the system[72] and they found that a very small dissymmetry between the frequency of propellers prevents the reversals of the average flow. To confirm the assumption that the -2 slope corresponds to the reversals, we imposed a dissymmetry in the propellers ($\Delta = 0.005$) and then we measured the azimuthal velocity. A comparison between the spectra with and without dissymmetry reveals how the reversals fade in the power spectrum (black line).

6.2.1 Reversal escape time as a function of Re

To complement the characterization of the random reversals that occur in the flow, we studied how these residence times vary as a function of Re . An exponential law was proposed to define this dynamics as[85]:

$$\rho(t) = \frac{1}{T_0} e^{(-t/T_0)} \quad (6.2)$$

where ρ is the probability density function associated to suffer a reversal after a time t and T_0 is the mean residence time. In Fig.6.3.a,b we present the velocity data series for two different Re numbers: we can observe how the system remains less time in each solution (the reversals are more frequent) as we increase the Re . So, if we compute the mean residence time for various Re we should recover a decreasing mean residence time when Re increases. In Fig.6.3.c we present these data, and although the data are not conclusive, it seems that the mean residence time follows an exponential decay law.

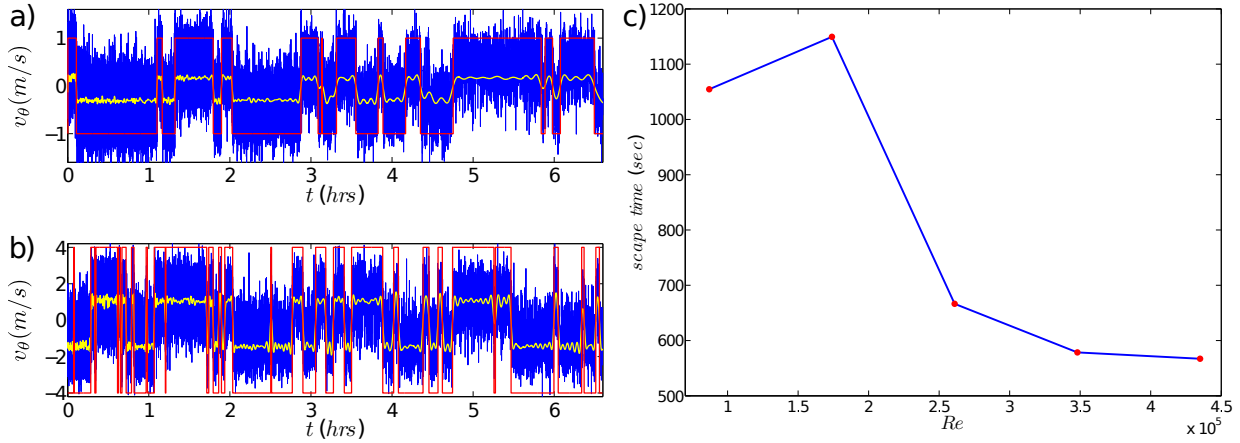


Figure 6.3: a)Azimuthal velocity measured at $z = 0, x = 9cm$, for $Re = 1.75 \times 10^5$. b)Azimuthal velocity measured at $z = 0, x = 9cm$, for $Re = 4.35 \times 10^5$. c)Mean residence time T_0 in function of Re numbers, measured in $z = 0, x = 9cm$.

6.3 Equatorial vortices instability

The appearance of vortices in shear flows has been previously reported for this and for similar configurations [5, 52, 53, 55, 93]. These vortices have two peculiar movements that have been investigated qualitatively or semi-quantitatively. One of them is the slight random vacillation of the vortex position along the z-axis, this movement corresponds in the power spectrum to frequencies at the end of the -2 slope. The second is an azimuthal rotation of the vortex along the wall of the cylinder and is clearly observed in a peak on the power spectrum of the axial velocity(see Fig.6.4.b).

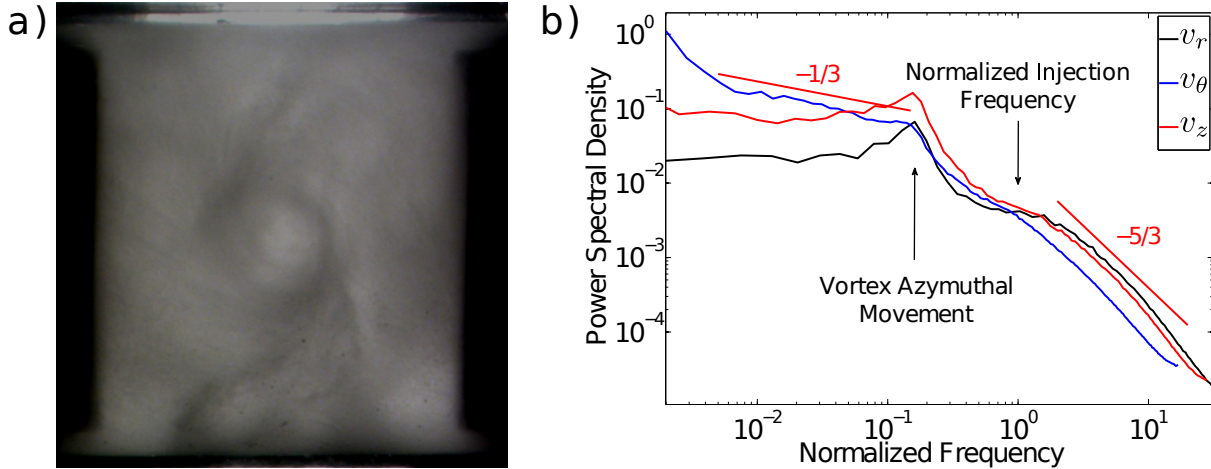


Figure 6.4: a) Lateral view of the experimental cell, using air bubbles as tracers. Large coherent vortices can be observed that rotate jointly with the dominant cell either with positive or negative azimuthal velocity. b)Power spectrum density for v_r , v_θ and v_z , for $Re = 1.7 \times 10^5$ in $r = 9cm$ and $z = 0$.

Since light particles tend to form clusters in regions where the vorticity is high we used air

bubbles as tracer particles for the visualization, and in this way we removed the very fast fluctuations. Using a camera located in front of the experimental set-up, we have determined that the number of vortices deployed along the perimeter fluctuates, is not constant, usually in the range between two to four. The typical size of one of these vortices is around 1/4 the diameter of the cell. In the visualization, the vortices show an azimuthal rotation movement in the shear layer linked to the largest global. This method of visualization seems valid only for the large structures, since the turbulence is highly distorted by the presence of preferential concentration[94].

To validate these results and to prevent any alteration of the flow, we obtained a semi-quantitative picture (a 2D reconstruction of the vortices) of the behavior of these structures based in measurements with the LDA. From the axial velocity fluctuations (Fig.6.4.b and Fig.6.5.b), we can capture the extension of these vortices in the radial and axial directions. Additionally, we can recover the mean vector field for the components \bar{v}_θ , \bar{v}_z , where the shear takes place and where the vortical instability appears. Then we filtered the axial velocity measured in the center of the cavity ($x = 9\text{cm}$, $z = 0$) with a 6th butterworth low-pass filter to obtain only the scales lower than the injection frequency. Introducing this variation into the mean vector field –along the cylindrical wall– and introducing empirically the extensions of the vortices in the radial and axial directions obtained from the fluctuations, what we observed is a semi-quantitative reconstruction of the vortices as it is shown in Fig.6.5.a. This reconstruction of the instability also provides the data of the number of vortices that appear in the azimuthal direction, the shape of them and their inherent movements. Finally, we would like to emphasize that the analysis of these coherent structures using two different approaches have led us to the same results.

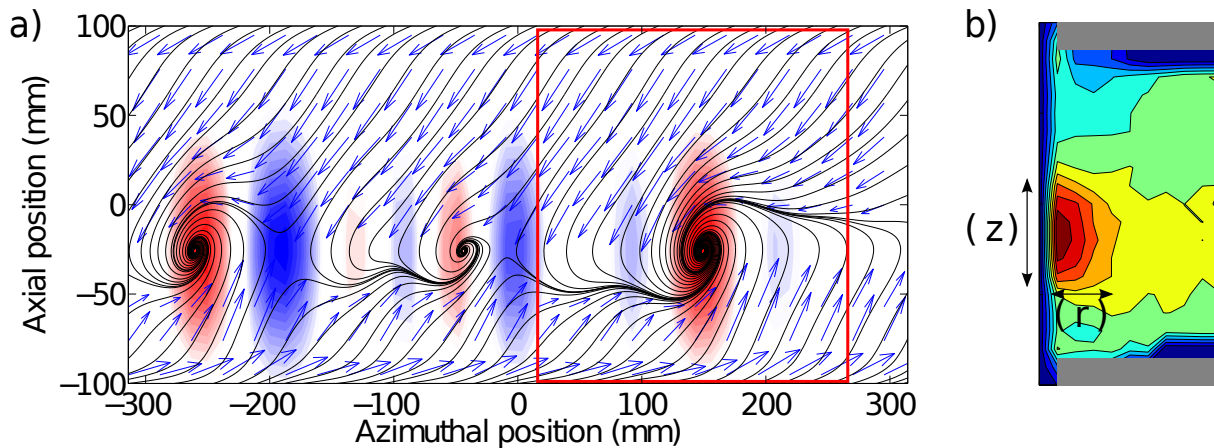


Figure 6.5: a) Reconstruction of the vortices. The observation window present in Fig.6.4.a is marked with a red box. The blue (resp. red) regions correspond to positive (resp. negative) vorticity. b) Fluctuations of the axial component.

A peculiar aspect of these vortices is that they are not stable, their size and number fluctuates in time and they can even disappear. As we can see in Fig.6.5 the vortices distribution along the wall is not homogeneous, i.e. the number of vortices and their form is changing. To better describe this distribution we can measure the time between the appearance of two vortices from the axial velocity. In Fig.6.6 we present the distribution of these times, and we have marked the situations associated to the times for regular patterns of two or three vortices. From this graph we

can explain that in an instantaneous picture of the flow the typical wave number obtained for this structures should be more than two. From the other side, when the time between two consecutive vortices is very small, the intensity of these vortices is very weak and they can be easily gone unremarked. This is the reason about why typically is reported a wavenumber between two and four. This analysis also shows that the distribution of times is not a simple exponential decaying law, but has a slower decay. Also, from the intensity of the axial component of the vortex, we can interpret the vacillation that can be appreciated in the qualitative visualizations.

However, this reconstruction of the vortices and their intensity along the wall shows only a small part of the complete dynamics of these large structures, since in the qualitative observations another phenomena as the instantaneous fading and the short backward movement, are difficult to analyze or quantify.

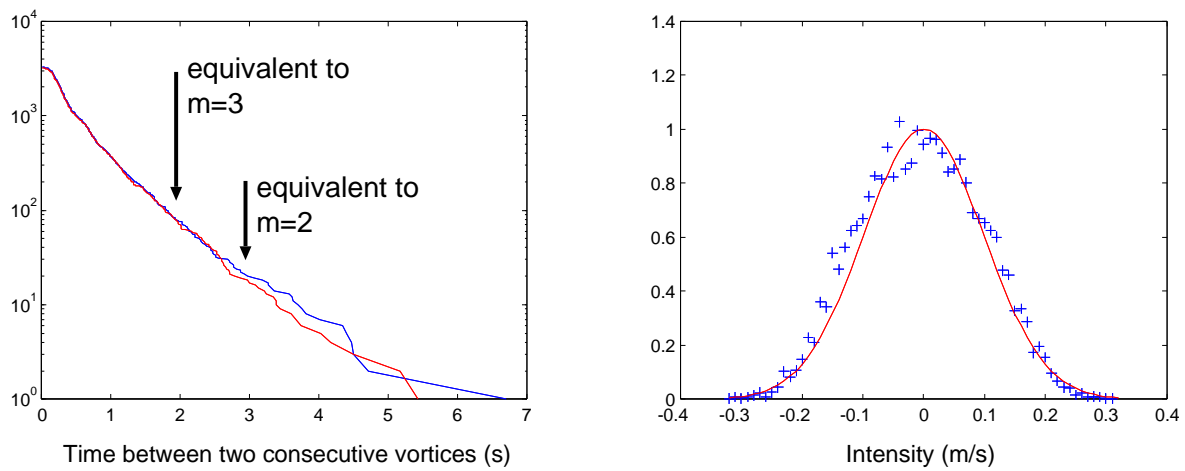


Figure 6.6: a)Distribution times of the vortices appearance, recovered from the LDA measurement of the axial component b)Intensity variation of axial component of the vortices

6.4 Inverse cascade

The concept of an inverse cascade was introduced by Kraichnan[33] in 1967. He predicted that in 2D turbulence the energy was transported towards the large scales and there should be a direct cascade that transports mean square vorticity to small scales. The principal mechanism to extract energy from turbulent flows for several decades has been attributed to the viscous dissipation. But this idea would lead us to assume that the evolution of the temperature of an enclosed turbulent flow, should be faster than it actually is. Cadot et al. [95] studied the energy injected in closed flows and they mentioned that the energy injected in the system is larger ($\sim 25\%$) than the energy dissipated by viscosity. Labé et al.[53] thought that the viscous dissipation is not the only way to extract energy from turbulent flows. They noted a concavity in the power spectra for a co-rotating von Kármán flow and they proposed that it might be due an inverse cascade. Also it is well known[60] that non trivial fluctuations could be attributed to the appearance of coherent structures in closed turbulent flows. A manifestation of the existence of these large structures is reflected in the exponential tails in the PDF of the power delivered to

the fluid and has been shown that this distribution are limited only by the system size[59]. So the idea that there is another magnitude (limited by the system) that can remove energy from the inertial range in turbulent flows could answer these questions.

In Fig.6.4.b a clear $-1/3$ slope appears, from the azimuthal vortex movement to the beginning of the reversals –slightly larger than one order of magnitude. We related these frequencies to slow changes of the position of the shear flow –slower than the injection. To understand this movement, we measured the components v_θ and v_z of the velocity along the shear layer located in $z = -2$ and what we found is an *inverse cascade* (a $-1/3$ slope appear in Fig.6.7.a, measured in the center of the cylinder $x = 0, y = 0, z = 0$). In this case the range of the frequencies where this slope appears, is from the injection frequency up to more than one order of magnitude backwards. In this graph three different slopes can be identified, one slope of $-5/3$ that represents the conservation of energy, the $-1/3$ inverse cascade and a region with slope 0 that is consistent with a random behavior. An important fact is that this cascade doesn't continue indefinitely towards the slow scales, this cascade ends at the minimum frequency that appears in the measurements at the center of the vessel, and it is the same scale that appears with or without reversals.

This cascade can be better defined increasing the Re number or measuring the position of the displaced shear layer and the center of the vessel. Noteworthy that this cascade appears only well defined in a thin section at both sides of the displaced shear layer, covering around 30% of the total length between the propellers. In this region there are no vortices and the evolution of the flow is not affected by the presence of this coherent structures (see Fig.6.7.a, no peaks are visible that may correspond to the presence of vortices). The evolution of the shear layer can be confirmed applying a low pass filter to the data series (Fig.6.7.b) for frequencies below the injection time. Here we can assume that this imaginary frontier separates both toroidal flows, so when the shear layer moves will affect the sign of the axial component and that movement is represented in Fig.6.7.b. This layer oscillates with very long times, and the case presented reaches ~ 100 turnover times that corresponds to a non-dimensional frequency of 10^{-2} which means a very slow movement.

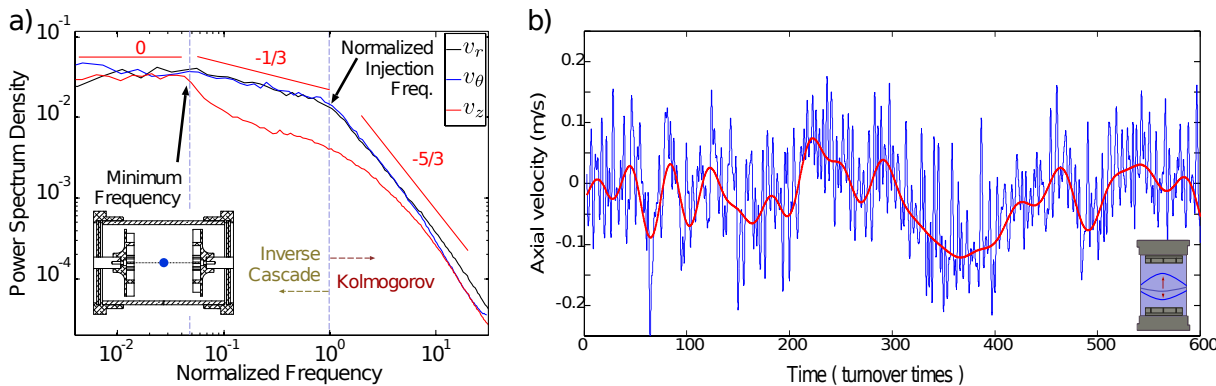


Figure 6.7: Behaviour of the flow at the centre. a) Spectrum at the centre of the shear layer ($r = 0, z = 2\text{cm}$). The direct and inverse cascades are visible.

6.4.1 Cospectrum of the torque

The magnitude of the turbulent torque in this configuration would be defined as $\mathcal{T}(r, z) = rv_\theta v_z$, that is the average turning force applied to the fluid per unit area along the axis. To obtain this magnitude, it is necessary to make very long measurements of the temporal evolution of this term $v_\theta v_z$ and with this measurements we could recover the corresponding cospectrum showed in Fig.6.8 for two different positions in the cavity. Due to our inability to measure at the same time the correlation between v_θ and v_z , we must first introduce the relation that exist between v_θ , v_z and v_{45} (defining v_{45} as the velocity component at 45 degrees in the plane v_θ, v_z), as:

$$\begin{aligned} v_{45} &= v_\theta \sin(45^\circ) + v_z \cos(45^\circ) \\ &\Downarrow \\ v_\theta v_z &= v_{45}^2 - \frac{v_\theta^2}{2} - \frac{v_z^2}{2} \end{aligned} \quad (6.3)$$

Once we have been defined the term $v_\theta v_z$ in the eq.6.3, our objective is to recover the power spectrum from the 1D LDV measurements. From the temporal evolution of these magnitudes, and being careful with the correct scaling that we must accomplish from different series with different number of data, we can compute the DFT (discrete Fourier transform) of the term $v_\theta v_z$. In Fig.6.8 we present the power spectrum of the torque in the VK flow for the positions at $x = 9cm, z = 0$ and $x = 0, z = 0$. In this spectrum we can observe at both positions similar cascades, with almost the same slopes that those observed in the power spectra for a single component and also for the case close to the wall it can be appreciated the influence of the vortices in the spectrum. Nevertheless in these cases, another difference could be that the cascades went further than in the case of a single component.

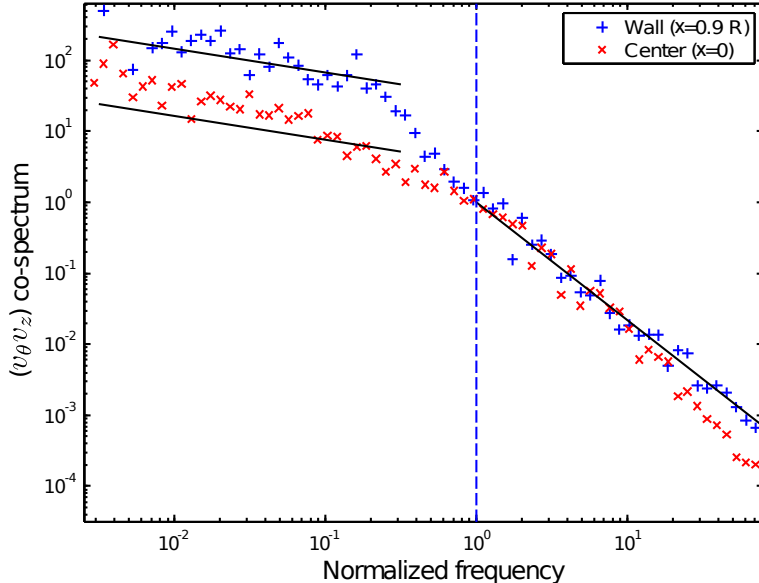


Figure 6.8: Cospectrum of $v_\theta v_z$ computed using LDA data from series 10³ seconds long at two different spatial positions $r = 0$ and $r = 0.9R$.

6.4.2 Spatial inverse cascade

In the previous temporal spectra it has been showed that slow frequencies appear in the flow. But the question is how these frequencies relate to spatial scales or wavenumbers. In those spectra the frequencies that correspond to the inertial range can be related to wave numbers due to the local Taylor hypothesis. This is not the case for the large scales, since this hypothesis could not be valid. In order to obtain the corresponding power law in the space domain, we directly measured the spatial distribution of the velocity fields using PIV. In order to have access to a broad range of wavenumbers, we used the three different field of views presented in the Fig.6.9. The dimensions of this fields were, $F_1 = 155 \times 125\text{mm}$, $F_2 = 55 \times 41\text{mm}$ (red box), and $F_3 = 17.5 \times 13\text{mm}$ (green box). For the computation of all the field of views, it was used an interrogation window size of $32 \times 32\text{ px}$ with a 50% of overlapping and no offset was used. Each of those field of view were taken in the region of the displaced shear layer (2cm away from the geometrical center), with the objective to recover the scales that are important in this thin space. To afford a good statistics on the measurements we computed at least 1500 vector maps for each one of these areas, with this approach we can cover the range of wave numbers necessary to encompass at least one order of magnitude larger than the integral length and one order of magnitude smaller.

It is well known that the computing of the vectors obtained from the PIV can alter or smooth much of the spatial and spectral properties, but this always happens in the high frequency range and only for very specific situations. The required analysis of the data from the experiments can prevent this type of noisy effects like the overlapping. Nevertheless these effects have been exhaustively tested and corrected by diverse groups [83, 84]. Based in the conclusions of these works, we tested by ourselves the impact of the overlapping and the offset width, computing the vector maps using different strategies. In both of the cited papers, the effect of the overlapping has been widely discussed by testing different configurations, even reaching the limit of 87% of overlapping and always the effects were altering the high spatial frequencies (small scales), but never on the low frequencies (large scales). In this research we placed good enough tracer particles with the objective to avoid the oversampling that are the principal cause of alteration of the spectra. In our system, we have typically 16-18 tracers per interrogation window, reaching a larger number than the value proposed by these authors. Only for the small field of view F_3 (where the inertial range appears), we had about 6 tracers per interrogation area, but only in less than a 5% of regions.

In Fig.6.10 we plotted a spatial power spectrum obtained with three different field of views, in this graph two clear slopes appear, one for the inertial range where the slope is close to $-5/3$ and an inverse cascade due the conservation of the angular momentum (as we will see in the next section) where the value of the slope is around $-7/3$. It should be mentioned that different post processing analysis were made for the three windows, and the scales larger than the integral scale were almost the same (slightly variation in the slope, but always close to $-7/3$) in all the cases. For the small scales the effect was more noticeable, because the analysis could change the small scales, an example on how to deal with these problems can be found in [84]. However, it is clear that two slopes appear in the spatial power spectrum and the change of its slope can be better seen in the inset of the Fig.6.10, where the spectra are compensated by $\kappa^{7/3}$.

We present in this research the first evidence of an spatial inverse cascade in a fully developed 3D experimental turbulent flow, where the experimental evidence suggests that the magnitude

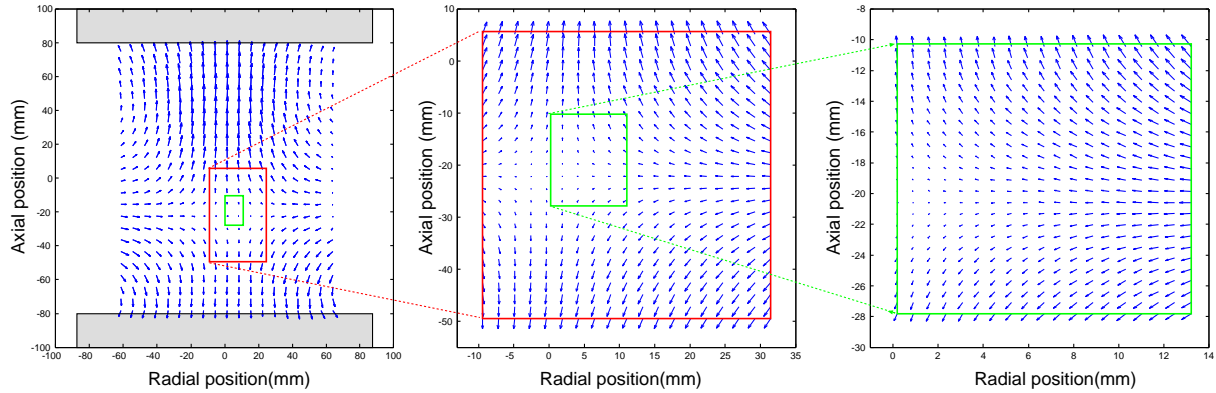


Figure 6.9: Mean fields obtained with different sizes in order to recover a wide range of wave numbers.

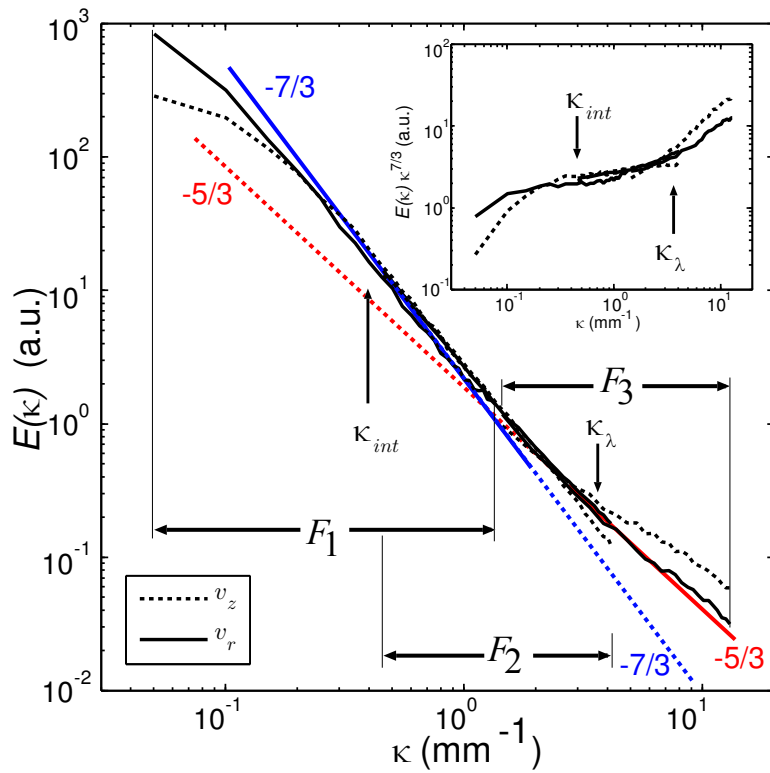


Figure 6.10: Spatial spectra computed from PIV measurements in a slice at the shear layer. Inset: Spectra compensated by $\kappa^{7/3}$. κ_{int} and κ_λ correspond to the integral scale and the Taylor microscale.

that is conserved is the angular momentum.

6.5 The angular momentum as a conserved magnitude

Any cascade that appears in Fourier space can be the signature of a conserved magnitude and this magnitude should be related to the conserved properties of an stirred flow, as its energy, mass or momentum. In the scenario conceived by Kolmogorov, the energy injected at the flow scale is not dissipated, but is transmitted over different range of scales until at the small scales the viscosity starts to plays its role of dissipation of such energy. In two-dimensional turbulence the vortices cannot be stretched, so in this perspective appears another conserved magnitude, the vorticity, and consequently two cascades appear, one direct (where the conserved magnitude is the enstrophy) and an inverse that transfers the energy.

Some years ago was proposed the conservation of the square of the total angular momentum for a fluid in a state of homogeneous and isotropic turbulence[96], and very recently different groups using a similar experimental configuration have validated that the angular momentum is a conserved magnitude in a turbulent flow[55, 70]. In our case, we follow a similar approach using in Ref.[55], to calculate the conservation of the angular momentum. Under that approach, the balance of the axial component of the angular momentum \mathcal{L} can be obtained, for a slender layer of the cross section of the cylinder of thickness ΔZ , as the difference of the drag between the upper and bottom slices (here we neglect the contribution or losses on the lateral wall). In this way we can obtain the rate of change for the angular momentum as:

$$\begin{aligned} \partial_t \langle \mathcal{L}_V(z_0) \rangle &= \left[\int_V \partial_t \langle \mathcal{L} \rangle dV \right] = \left[\int_V \rho \langle rv_z \partial_z v_\theta \rangle dV \right]_{z_0} = \\ &= \left[\int_A \rho \langle ru_\theta u_z \rangle dA + \int_A \rho r U_\theta U_z dA \right]_{z_0 + \Delta z/2} \\ &\quad - \left[\int_A \rho \langle ru_\theta u_z \rangle dA + \int_A \rho r U_\theta U_z dA \right]_{z_0 - \Delta z/2} \end{aligned} \quad (6.4)$$

where $\mathcal{L}_V(z_0)$ measures the z -component of the angular momentum per unit mass in the considered volume $V = A \Delta z$ between $z_0 - \Delta z/2$ and $z_0 + \Delta z/2$ and where $A = \pi R^2$. The velocities have been splitted in two terms, $v = u' + U$, U is the mean value, and u' are the zero-mean fluctuations. In these fluctuations the slow and fast evolutions appear combined, but only the slow evolution plays an important role as it contains most of the energy on the power spectrum.

In order to measure the correlated term $\langle u'_\theta u'_z \rangle$ involved in the eqn.6.4, we follow the same approach as Ref.[55]. Several measurements were done at different directions (u'_θ , u'_z , u'_{45} and u'_{135}) and then using the expressions $u'_{135} \simeq (u'_\theta - u'_z)/\sqrt{2}$ and its variance $2\langle u'^2_{135} \rangle = \langle u'^2_\theta \rangle + \langle u'^2_z \rangle - 2\langle u'_\theta u'_z \rangle$, the term $\langle u'_\theta u'_z \rangle$ can be recovered. Now we can define the total torque applied of an slice of a surface A , as $\mathcal{T}_A = \int_A \mathcal{T} dA$, this parameter can be measured for different values of z and its integration in time is presented in the Fig6.11. If this magnitude remained constant along z , that would mean that the torque balance across a fluid slice would be zero conserving the angular momentum. It is noteworthy that in our case it was not possible to measure the

total torque delivered by the propellers to compare it with the velocity measurements, since in our experimental device there are not torquemeters.

In Fig.6.11 we can see that the total angular momentum along the z axis remains almost the same (black inverse triangles), also we can see how the fluctuations (\mathbf{v}' , red diamonds) are responsible of the angular momentum flux in the central region and the mean flow (\mathbf{U} , blue triangles) is in charge for this flux close to the impellers. Until here, our results shows the same behavior to the previous results reported by Marie et al.[55], with the difference that the position of the shear layer is different.

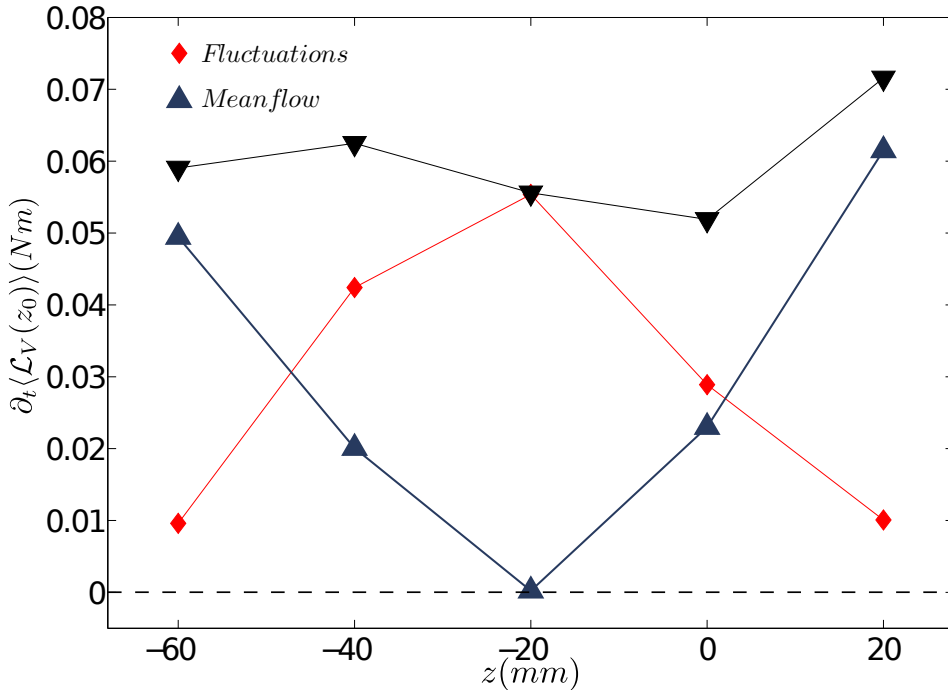


Figure 6.11: Angular momentum flux for different slices along the axial direction. In black inverse triangles we present the total angular momentum flux($\partial_t\langle\mathcal{L}\rangle$), in dark blue triangles the contribution of the mean flow $\int \mathcal{T}_A^U dt$ and in the red diamonds the contribution due the flow fluctuations $\int \mathcal{T}_A^{u'} dt$.

However, we would like to go further in order to compare the contributions of the small scales and the large scales in the angular momentum of different slices. In Fig.6.12 we present the same study as in the Fig.6.11, with the difference that here we report the contribution of the small (light blue inverse triangles) and the large scales (red diamonds) to the angular momentum. In both figures close to the shear layer the contribution of the mean flow is almost zero ($U_\theta \simeq U_z \simeq 0$), therefore the contribution of the angular momentum flux are in charge by the fluctuations. This fluctuation can now be splitted in two terms, the part that corresponds to the fast frequencies ($\mathcal{T}_A^{u>}$) and to the slow frequencies ($\mathcal{T}_A^{u<}$). In Fig.6.12 we show the amount of the contributions of the fast and slow frequencies. What we conclude, is that most of the angular momentum transferred at the center of our vessel was done by the fluctuations of the slow frequencies that correspond to the large scales (a detailed description can be seen in [48]). The fast fluctuations have not effect for the angular momentum transport in any position.

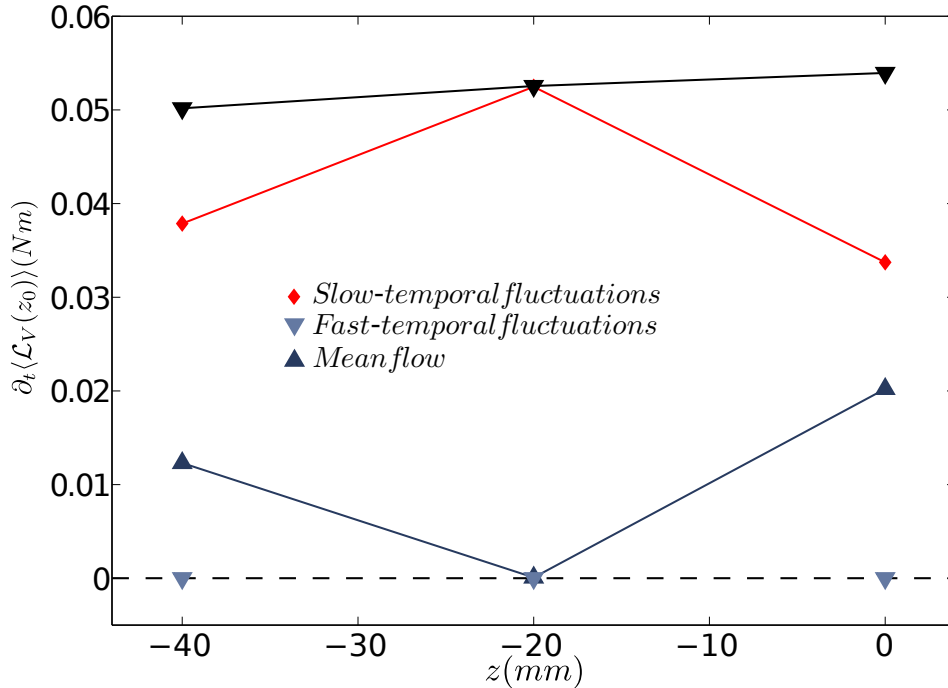


Figure 6.12: Angular momentum flux for different slices along the axial direction. In black inverse triangles we present the total angular momentum flux($\partial_t \langle \mathcal{L} \rangle$), in dark blue triangles the contribution of the mean flow $\int \mathcal{T}_A^U dt$, in light blue inverse triangles the contribution of the fast frequencies ($\mathcal{T}_A^{u>}$) and in red diamonds the contributions of the slow frequencies ($\mathcal{T}_A^{u<}$).

6.6 Dimensional analysis

Up to here we have presented how the angular momentum is a conserved magnitude along the z axis and the large scales are the principal responsible for the transfer of this magnitude across the shear layer. Based on this we now can defined the evolution of the axial component of the angular momentum \mathcal{L} at a given position as:

$$\partial_t \mathcal{L}_V^2 \sim \int_V 2r^2 u_\theta u_z \partial_z u_\theta dV \quad (6.5)$$

Using this expression we can infer that the transfer rate of the angular momentum will evolve dimensionally as:

$$\varepsilon_L = L^2 \cdot \frac{L^3}{T^3} \cdot \frac{1}{L} = \frac{L^4}{T^3} \quad (6.6)$$

where L and T correspond to the spatial and temporal scales. From here we can do a dimensional analysis of the angular momentum contained in a given volume, assuming isotropic and homogeneous fluctuations, then we obtain for its Fourier transform:

$$\mathcal{L}_V^2 = \int \mathcal{L}_F^2(\kappa) d\kappa \quad (6.7)$$

where $\mathcal{L}_F^2(k)$ is the Fourier transform of $\mathcal{L}_V^2(r)$. If the angular momentum is a conserved magnitude and only depends on the transfer rate of angular momentum and on the wave number, we would expect a power law:

$$\mathcal{L}_F^2(\kappa) \propto \varepsilon_L^{\alpha_1} \kappa^{\alpha_2} \quad (6.8)$$

To determine the coefficients α_1 and α_2 , we will use a dimensional analysis in order to obtain these values, then we set:

$$\begin{aligned} \mathcal{L}_V^2 &\propto \varepsilon_L^{\alpha_1} \kappa^{\alpha_2} \kappa \\ \frac{L^4}{T^2} &= \frac{L^{4\alpha_1}}{T^{3\alpha_1}} \cdot \frac{L^{-\alpha_2-1}}{1} \end{aligned} \quad (6.9)$$

From here we obtain the values to $\alpha_1 = 2/3$ and $\alpha_2 = -7/3$, obtaining a power law:

$$\mathcal{L}_F^2(\kappa) \propto \varepsilon_L^{2/3} \kappa^{-7/3} \quad (6.10)$$

If we do the same for the kinetic energy defined as:

$$\mathcal{E}_V = \frac{\mathcal{L}_V^2}{\mathcal{I}_V} \quad (6.11)$$

where \mathcal{I}_V is the moment of inertia of the corresponding fluid layer around the axis. This dimensional analysis shows the same scaling for the kinetic energy as:

$$\begin{aligned} \mathcal{E}_V \mathcal{I}_V &\propto \varepsilon_L^{\alpha_1} \kappa^{\alpha_2} \kappa \\ \frac{L^2}{T^2} \cdot \frac{L^2}{1} &= \frac{L^{4\alpha_1}}{T^{3\alpha_1}} \cdot \frac{L^{-\alpha_2-1}}{1} \\ \mathcal{E}(\kappa) &\propto \mathcal{R}^{-2} \varepsilon_L^{2/3} \kappa^{-7/3} \end{aligned} \quad (6.12)$$

We can do the same approach for the temporal behavior in a given position. As this evolution should depend on some way on the advection of the spatial distribution of the flow, we can expect that in this case the spectra would depend on the advection velocity U . As $\mathcal{L}_F^2(\omega)$ (where \mathcal{L}_F^2 is the Fourier transform of \mathcal{L}_V^2 in the temporal domain) will also depend on the rate of transfer of the angular momentum and the frequency, this function should go through a law :

$$\begin{aligned} \mathcal{E}(\omega) &\propto U^{\alpha_1} \varepsilon_L^{2/3} \omega^{\alpha_2} \omega \\ \frac{L^2}{T^2} &= \frac{L^{\alpha_1}}{T^{\alpha_1}} \cdot \frac{L^{8/3}}{T^2} \cdot \frac{1}{T^{\alpha_2}} \cdot \frac{1}{T} \\ \mathcal{E}(\omega) &\propto U^{-2/3} \varepsilon_L^{2/3} \omega^{-1/3} \end{aligned} \quad (6.13)$$

This simple theoretical dimensional analysis on how should evolve the kinetic energy in the temporal and space domains, corresponds at least with the power laws measured along of the zone where the fluid is sheared.

6.7 Large scale structures at the slow scales

The existence of coherent structures generated by a fluid in a turbulent regime is well known since many years, but their origin still does not have a solid explanation. The manner that people faces these questions are via phenomenological observations and experimental measurements. A good description about coherent structures can be found in [11] where the example of the Kelvin-Helmholtz instability could be assimilated to our case.

In the relationship that we gave above[48], where we showed that the angular momentum is a magnitude preserved in this setup, we proposed that if the angular momentum is conserved, we would expect a power law for the kinetic energy:

$$\mathcal{E}(\kappa) \sim \kappa^{-7/3} \quad (6.14)$$

Also, we have proposed that this behavior should be correlated to the temporal dynamics:

$$\mathcal{E}(\omega) \sim \omega^{-1/3} \quad (6.15)$$

All these arguments lack of a solid theory, nevertheless, the experimental facts have demonstrated that large scales are appearing in this VK flow. If this approach is correct, the slow dynamics should be associated to the existence of large structures. As a mode of visualization of such scales, we averaged the turbulent fluctuations in a period larger than the injection. The results are showed in Fig.6.13. In these examples of an average of 40 images, that correspond to a period of 2.7 sec, it is possible to observe how for these slow temporal scales, recirculations much larger than the integral length are created.

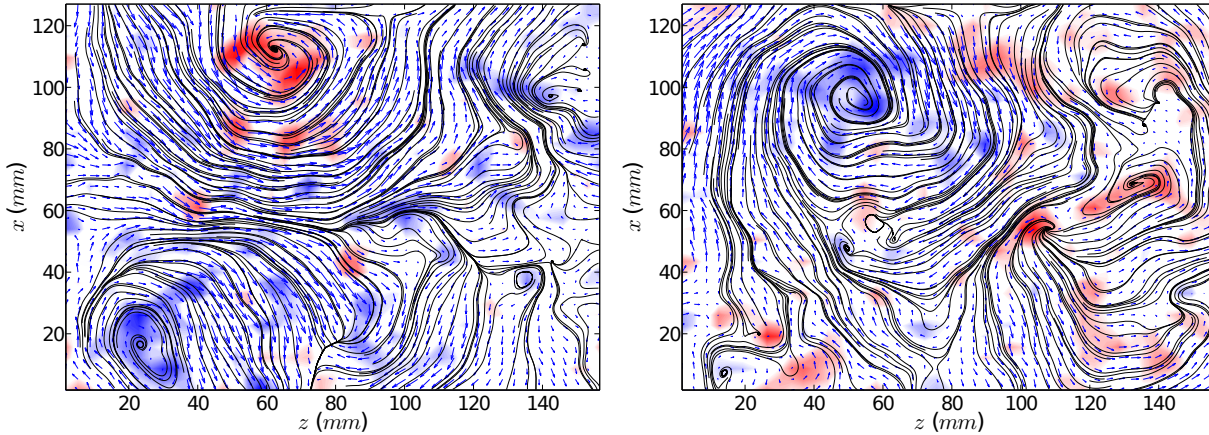


Figure 6.13: Examples of averaged vector fields of the turbulent fluctuations during a period of 2.7 sec, here we can observe large scales compared with the integral length.

6.8 Inertia and impeller stability

The inertia of a body is the capability to be unperturbed by the external forces and in the case of generate turbulence as we see is a key parameter. This parameter will be crucial when there is a sudden demand of kinetic energy into the fluid because of a turbulent flow fluctuation.

In the presented set-up we have found a lot of results similar to those of other devices, but some of them, as the appearance of slows behaviors, seemed to be characteristic of our device. Later, some of these behaviours (as the reversals) have been observed in other setups, but nevertheless we still missed the reason of the difference.

We believe that the reason is because of the impeller stability and the inertia. In our case the standard deviation of the instantaneous impeller frequency is of the order of 0.1%, compared to the mean value of the impeller rotation velocity[85] and the high inertia comes from the inertia of the rotor of the motor, increased by the gear system combined with the axis and impeller inertia. These features of this set-up are quite different from other von Kármán used for the study of turbulence. Since in our system the moment of inertia of the gear system is ($I_{tot} \sim 2.65I_{H_2O}$) more than twice the moment of inertia of the fluid, we can expect that any kinetic energy demand by the fluid will not affect the stability of the propeller and the flow can evolve freely. If the inertia of the impeller is low, any kinetic energy demand will result in a decrease of the angular momentum (and frequency) of the impeller itself, so this creates a feedback that can affect the dynamics as it happens in other configurations.

Moreover, if we remove the lids and let the fluid inside the cylinder interact with the unenclosed fluid tank, what would expect, is to reduce the difference between the moment of inertia of the injection and the moment of inertia of the fluid (this last is increased by a factor ~ 10). In Fig.6.14.a, we compare the PSD with (blue line) and without covers (black line), as we expected, a difference appears in the inverse cascade. For the case without covers, the long slope reported in the previous sections reduces its length considerably, while for the case with covers it's clear the appearance of the inverse cascade. Finally, a similar result can be obtained in the closed cylindrical cavity when an artificial random fluctuation of 1% is introduced on the impellers frequency.

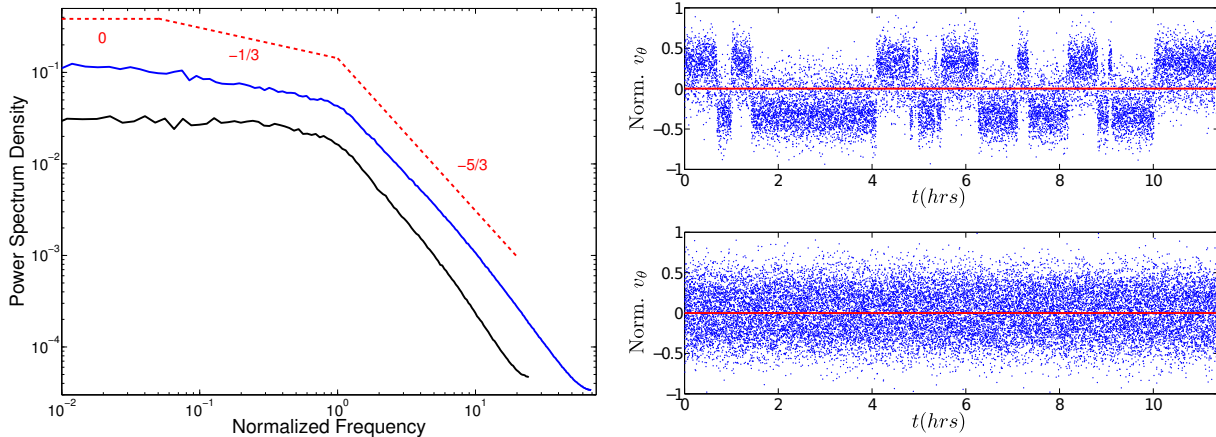


Figure 6.14: a)Power spectrum density in the temporal domain for the case with and without covers, measure at the center of the vessel for the azimuthal component. b) Azimuthal velocity signals measured close to the wall for the cases with and without covers.

Other possible cause of this difference in the slope could be the pressure gradients generated inside the tank, in some way the pressure gradients may alter the flow producing slow movements related to large scales. But certainly these are only speculations about the nature of this difference and a rigorous research is needed to elucidate this uncertainty.

Also if we plotted the normalized velocity signals – see Fig.6.14.b– measured at the wall of the cylinder, what we see clearly is that also the reversals vanished, meaning that the shear layer for the case without caps is placed at the middle of the cavity as was reported in chapter 4.

7 Lagrangian Particle

Resumen

En este capítulo se presenta el seguimiento lagrangiano de esferas de diferentes tamaños arrastradas por un flujo turbulento. Si bien la idea original era utilizar este estudio como una herramienta para analizar las inversiones que ocurren en el flujo medio, se obtuvo un comportamiento dinámico propio que puede ser descrito por un proceso estocástico. Aquí intentaremos describir el comportamiento lento que las partículas grandes (del orden de la escala integral) siguen en un flujo turbulento, la relación que estos movimientos lentos tienen con las mediciones eulerianas de velocidad y cómo estas dinámicas pueden verse afectadas variando algunos parámetros.

Asumiendo que la densidad de las esferas utilizadas es homogénea y casi idéntica a la densidad del agua, hemos estudiado su evolución asemejándola a la de un volumen de fluido impenetrable. Se han caracterizado las diferentes escalas temporales del sistema, tal y como se han reportado en el capítulo 6: realizamos el seguimiento de este volumen durante un largo periodo de tiempo utilizando una proyección 2D en el plano (y, z), y luego hemos comparado los resultados para las diferentes escalas espaciales (diámetros) medidas. Si bien la mayoría de los tamaños elegidos fueron mayores a la escala integral, también incluimos una más pequeña para tener un punto de referencia basado en el tamaño. Igualmente, diferentes frecuencias de inyección fueron usadas con el objetivo de explorar otro parámetro, así como también exploramos diferentes valores de la longitud L tras los propulsores manteniendo una distancia H (altura del cilindro donde evolucionan las esferas) fija.

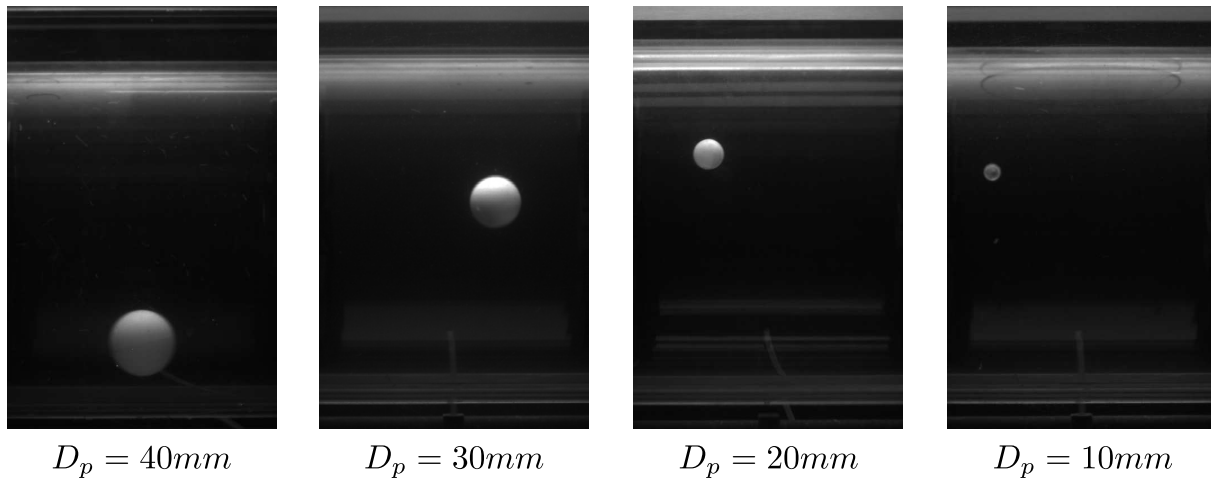


Figure 7.1: Quasi neutrally buoyant spheres of different diameters, inside of the von Kármán flow.

Abstract

In this chapter we report the Lagrangian tracking of different spheres dragged by a turbulent flow. Although the original aim was to use this study as a tool to analyze the reversals that occur on the average flow, we obtained a new dynamical behavior that could be described as a stochastic process. Here we will try to describe the slow behavior that large particles (bigger than the integral scale) present in turbulent flows, the relationship that these slow motions may have with the Eulerian velocity measurements and how their dynamics can be affected modifying some parameters.

Assuming that the density of the sphere is homogeneous and almost identical to the density of water, we have studied their evolution as if they were fluid volumes with impenetrable walls. Different time scales of the system have been characterized, as the ones reported in chapter 6: we recorded the evolution of this volume for a long period of time using a 2D projection on the (y, z) -plane, and then we compared the results for the different spatial scales (diameters) measured. Although most chosen sizes were larger than the integral length, we also included one smaller to have a reference point based on the sizes. Likewise, different injection frequencies were used in order to explore another parameter, as well as different lengths L (the space behind the propellers) for a fixed distance between the impellers H (that is, the height of the cylinder where the spheres evolve).

7.1 Slow dynamics

Using a FireWire (IEEE 1394) CCD camera we tracked the position of an inertial particle immersed in the fluid. The camera was placed perpendicular to the axis of the cylinder, so we recorded only the evolution in the (y, z) plane and the behavior on the x direction is completely lost. Although this could be very easily avoided using two cameras placed in orthogonal directions, we decided to record in a first experimental run the dynamics in that plane and the evolution in the whole 3D space will be postponed for a future experiment. Each experimental run was done with an image acquisition rate of 10 frames per second (fps) for a period of 1.8 hrs. We performed series of runs for different sizes ($D_p = 10, 20, 30$ and 40 mm) and rotation frequencies (only for specific cases these values were changed).

In Fig.7.2.a-d we present the evolution of the position of the particles along the z axis for the four different sizes, using the same rotation frequency in both propellers ($f_{prop} = 3.16\text{Hz}$). If the dynamics of the average flow or the average flow itself had no influence on the dynamics of the particle, these graphs should be symmetrical around the equator $z = 0$. If the dynamics of the spheres depends on some of these features of the average flow, a signature of this influence should appear on these plots. In this graph we can see how the smallest particle $D_p = 10\text{mm}$ (Fig.7.2.a) doesn't reveal the reversals that appear on the flow, but the evolution of the particles $D_p = 20\text{mm}$, $D_p = 30\text{mm}$ and $D_p = 40\text{mm}$ (Fig.7.2.b-d) shows the reversals (marked as a red line).

Our principal interest on the measurement of the dynamics of a large particle inside this fully developed turbulent flow was to give some answers about the origin of these reversals, or at least

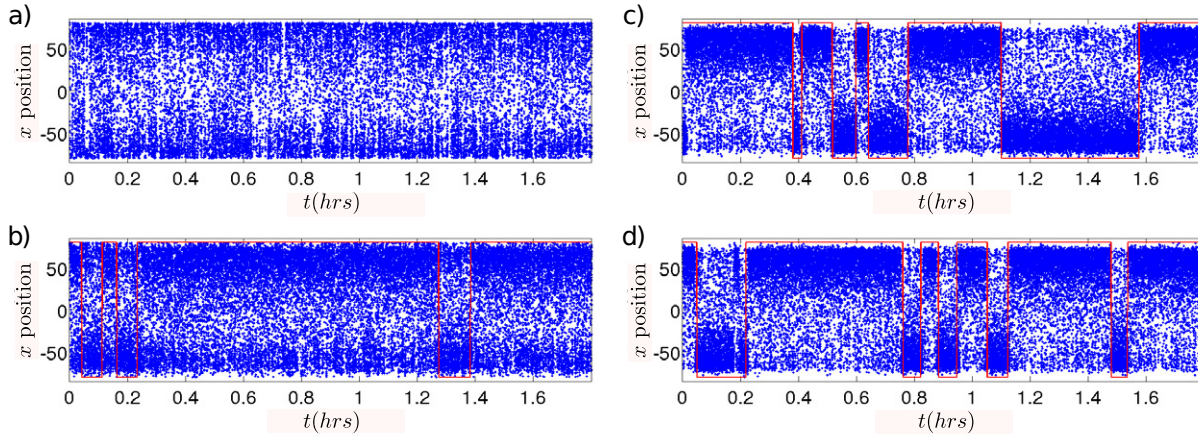


Figure 7.2: Tracking of the axial position of different particles along time. a) $D_p = 10\text{mm}$. b) $D_p = 20\text{mm}$. c) $D_p = 30\text{mm}$. d) $D_p = 40\text{mm}$. The red line represents the reversals of the average flow.

to give a qualitative measurement of the effect of this flow on the large particles. The first step to achieve this goal is to characterize the time that the particles remain close to each one of the propellers, inside one of the regions located at each side of the shear layer. If the spheres “feel” this asymmetry, the time they will remain in one of the toroidal circulations will be different from the other one. In order to differentiate the position of the particles (for particles larger than the integral scale) we will refer to these two locations as the preferential (when the particle remain statistically longer periods of time in one side of the vessel) and the non-preferential side (when the particle remain statistically small periods of time in one side of the vessel). This differentiation can be done for all the sizes, except the smallest one ($D_p = 10\text{mm}$); because in that case the particle is not sensitive to any asymmetry of the flow. For this configuration, the residence time in each one of these regions is the same, regardless what is the exact situation of the asymmetric average flow.

Before we start the analysis, a low pass filtering is applied to the data series to split the cases where the average flow is in the N and S states (see Fig.7.3.a, red line). Then, for each one of these states we compute the escape times in the preferential and in the non-preferential sides. Moreover, as we know that the N and S states are symmetric, a better statistics can be obtained from the signals if we reverse one of the states (as it is showed in Fig.7.3.b). Nevertheless, we present the results for both states (N, S) in order to compare their values and only for specific situations we will use the rectified series.

Although from these series we can ensure that the particles follow quite well the reversals of the average flow; we decided to verify this point directly. So we measured at the same time the azimuthal velocity close to the wall ($x = 0.9R, y = 0, z = 0$) using the LDV technique and the position of the particle along the axial direction using the FireWire camera. The result of these measurements is shown in Fig.7.4, where we can appreciate that the dynamics of the sphere is slaved to the average flow evolution (see Fig.7.4.b). Also, in both figures we can appreciate that the reversals that appear in the fully turbulent flow are not affected by the presence of a large neutrally buoyant particle, so the agreement between these measurements leads to asseverate that large neutrally buoyant particles follow perfectly the very slow temporal scales in the fully

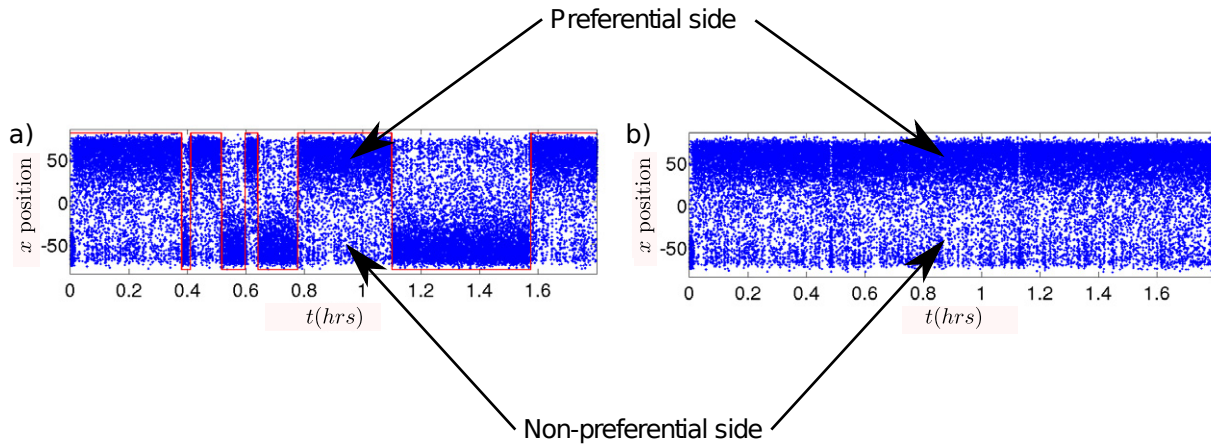


Figure 7.3: a) Axial position as a function of time for the 30mm sphere, using a frequency rotation of 3.16Hz. The preferential zones (respectively non-preferential) correspond to the areas with more data (respectively, with fewer data). b) The same signal as in a), rectified reversing the state S.

turbulent flows.

7.1.1 Escape times and preferential times

We have performed a study of the *residence times* of the particles along the axial coordinate, similar to the one presented in the previous chapter for the average flow. Just in this case, *escape time* refers to the short residence times that spheres remain in the non-preferential side of the cavity and *preferential time* when they are in the preferential side. We use the same expression for the residence times than the one introduced in the average flow reversals, defined as the probability of the sphere to remain in one side, until after some time spontaneously jumps to the other side; as it is defined in eq.6.2.

We present the results of a single case in Fig.7.5, where both the preferential (see Fig.7.5.a) and escape times (see Fig.7.5.b) are obtained through the slope of an adjusted exponential function (the red line drawn in the figures). We have characterized how the escape times of the non preferential zones depend on the parameters of the spheres (diameter) and flow (frequency or Re number), as a first step to understand why the particles shows this tendency to explore this region.

In Fig.7.6 we report the preferential (PT) and the escape times (ST) obtained varying the Re number for the four different sizes D_p of the particles. We also differentiate whether the flow was in the N or S state, although its effect is very small as it can be deduced from the computation of the residence times. For each parameter set (D_p, Re) both series (N, S) are presented. They share the same color but, as the difference is very small, we decided to let them unlabeled as these would make the graph very confusing (i.e., see the 30 mm case, PT: the two blue lines correspond to the N and S states). The main conclusion from this part is that, as it was envisaged, the spheres have a symmetrical behavior when the flow is reversed, without any other major effect. But also this result gives us certainty of the symmetrical properties of such N, S states.

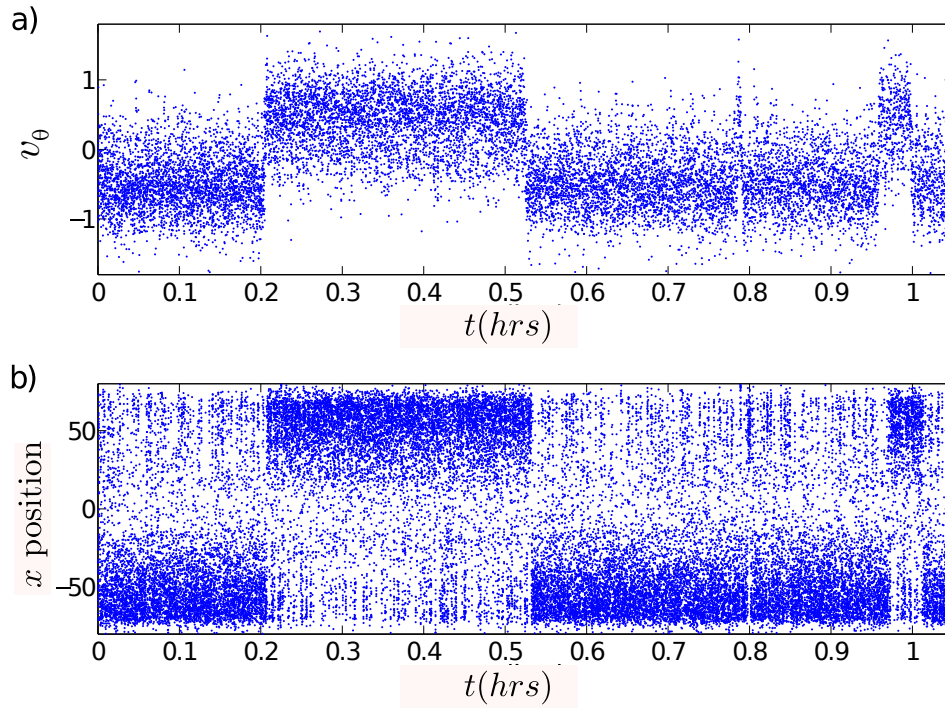


Figure 7.4: a) Azimuthal velocity measured close to the wall of the cylinder ($x = 0.9R, y = 0, z = 0$). b) Tracking of the axial position along the cylinder.

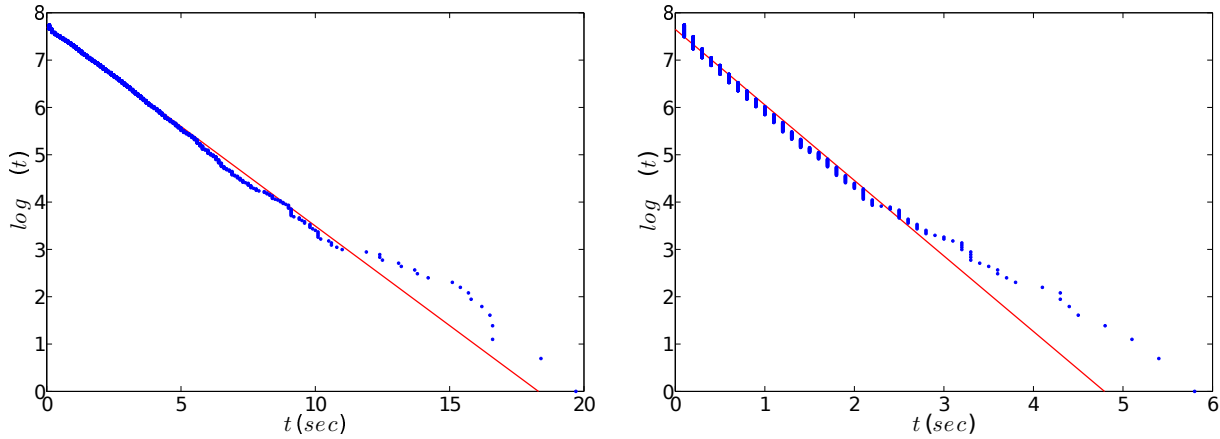


Figure 7.5: a) Experimental probability density function of the residence times for the preferential side of the cavity. b) Experimental probability density function of the residence times for the non-preferential side of the cavity

Also as it was expected while we increase the angular velocity in the propellers (Re) the escape times decrease for all the diameters. These results show a similar tendency as the one obtained for the reversals in the flow (where an increase of the Re shortens the residence times between reversals), except that here we are evaluating the effect of the velocity fluctuations integrated in a smaller control volume, instead of the whole fluid mass.

From this graph we can also conjecture that the residence times reach a plateau for large Re , where they will attain a stable value. Nevertheless this can only be asseverated by new experiments for larger values of the Reynolds number that cannot be reached with the current setup. Nevertheless it can be observed that for the preferential zones the decreasing of the escape times is more accentuated than for the cases of the non preferential zones.

Finally, for spheres smaller than the integral length ($D_p = 10\text{mm}$) we cannot distinguish between the preferential and the non-preferential zones (see Fig.7.3.a). In this situation both sides of the shear layer are visited with the same probability. This is the reason why there is only a set of two curves for $D_p = 10\text{mm}$ (one for each side of the shear layer) instead of the pair of preferential times and the pair of scape-times. This is an important observation for which we have no explanation, but the large particles “feel” the existence of an asymmetry in the average flow, whereas the small particles are “blind” to this large scale characteristic. We could suppose that the small spheres are more sensitive to the small scale fluctuations (smaller than the integral length) and the large ones integrate these fluctuations and are sensitive to larger scales dynamics. But this conjecture has not been demonstrated.

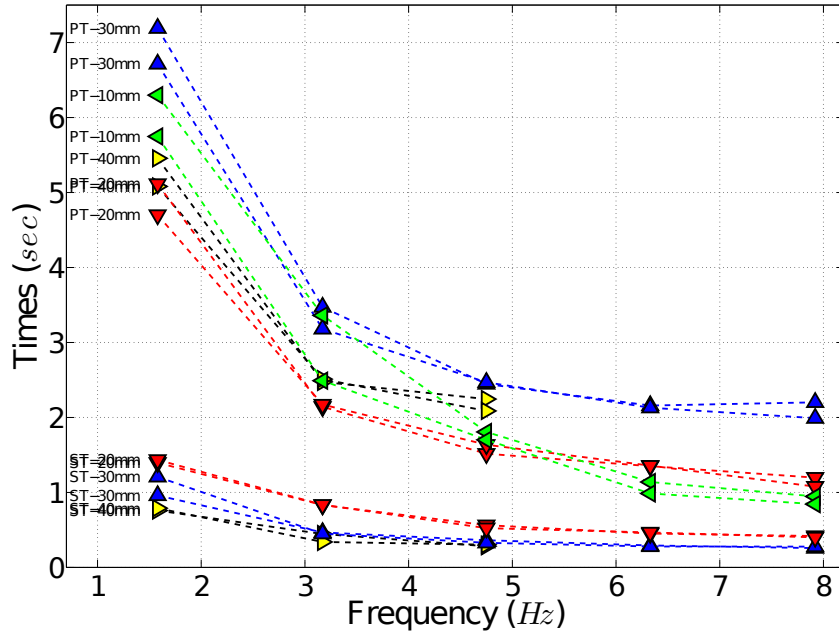


Figure 7.6: PT and ST as a function of different frequencies, for different sizes.

The next step to characterize the preferential and the escape times is to look for the effect of a change of the volume of the spheres (these results are plotted in the Fig.7.7). To interpret the influence of the diameter in the preferential time is quite ambiguous, since in this graph we can only appreciate a tendency for large particles and in our opinion this study needs a more extensive research. Also in this graph we can observe how if we increase the size of the spheres,

the time that the particle remains in the non-preferential zone decreases. This result probably means that if we increase the volume of fluid considered inside of a turbulent flow, the small scale fluctuations compensate and only sees the long time fluctuation, and will remain longer and longer time in the preferential zone. Nevertheless these results are difficult to interpret without the whole information of the dynamics of a large particle, with the analysis of the full data set of the 3D displacement with a fast acquisition rate.

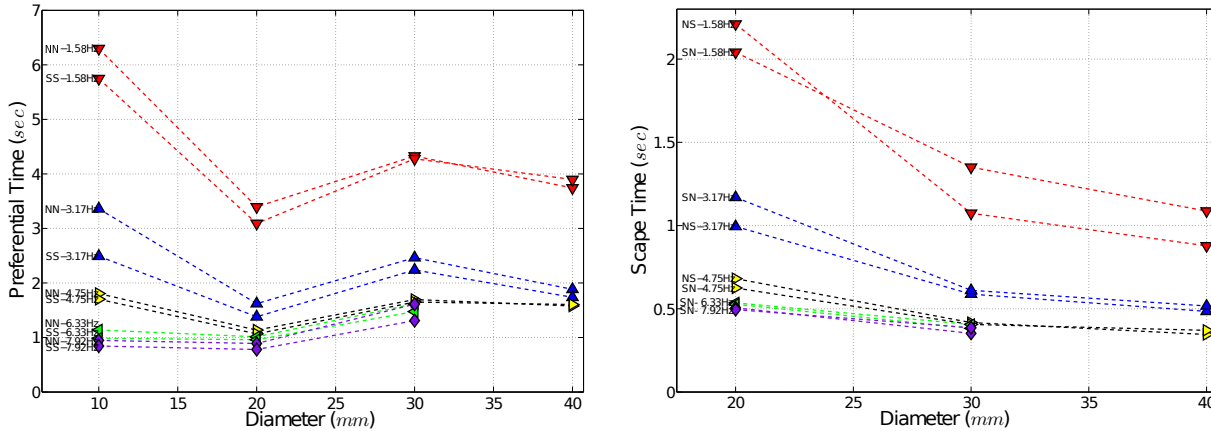


Figure 7.7: (a) Preferential times and (b) escape times as a function of different diameters. The labels indicate if the mean residence time is computed for the preferential zone (SS, NN) or for the non-preferential (NS, SN), depending the asymmetric state in which the average flow remains.

7.1.2 Propeller position independence

When the experimental setup was conceived, we wanted to have access to the control of the space behind the propellers. There has been a debate between the different experimental teams around the world to explain the different results obtained in different setups. One of the differences among these setups was the space behind the propellers: some experiments have cooling coils to stabilize the temperature, others have a different space behind one of the propellers, and so on. These regions may have a strong influence because there exist a recirculation of fluid and pressure gradients that could affect the flow dynamics between the impellers.

In our system we built the experimental cell as symmetric as possible, and this is one of the reasons of the choice of the horizontal orientation. If there were a temperature difference between the bulk and the space behind the propellers, a vertical orientation could induce a symmetry breaking because of gravity, and although this effect should be really small (actually, we believe is negligible) we preferred to avoid that. At the same time, the horizontal orientation had a lot of advantages from the point of view of the experimentalist.

As it was explained in chapter 3, we can control the position of the experimental volume, in such a way that $L_N + L_S + H = \text{constant} = 32\text{cm}$. We have performed different runs, with a constant distance between propellers $H = 20\text{cm}$. So, we can modify at will L_N , while L_S will vary accordingly. In order to analyze the effect of this asymmetry on the flow, we had a choice: either we could measure the evolution of the velocity field, that is quite slow because it means very long acquisitions, or we could measure how the preferential and residence times evolve as

a function of this asymmetry. This last approach is much faster, so we decided to evaluate this influence using the spheres.

To perform this characterization, we fixed the particle size and propeller rotation frequencies to $D_p = 20mm$ and $f_{N,S} = 3.17Hz$ respectively. Then we change the length L_N every millimeter for several positions in order to compare its preferential and escape times, with the objective to see if some difference appear in the statistical behavior of the times that the particles remain in one or in the other side of the vessel. In the Fig.7.8 we show that non difference were observed for the set of positions measured, also no difference appear for both the preferential and the escape times.

This result means that, at least for the slow dynamics of the flow, even a modification of this space L in as much as a 12% (1cm compared to a typical value of 6cm in the totally symmetric system $L_N = L_S$) has no significant effect, since no difference was observed in the mean residence times. In conclusion, the origin of the different results obtained in different experimental setups should be found in other aspects of the experimental setups, as the stability of the propellers frequency as it was explained in the previous chapter.

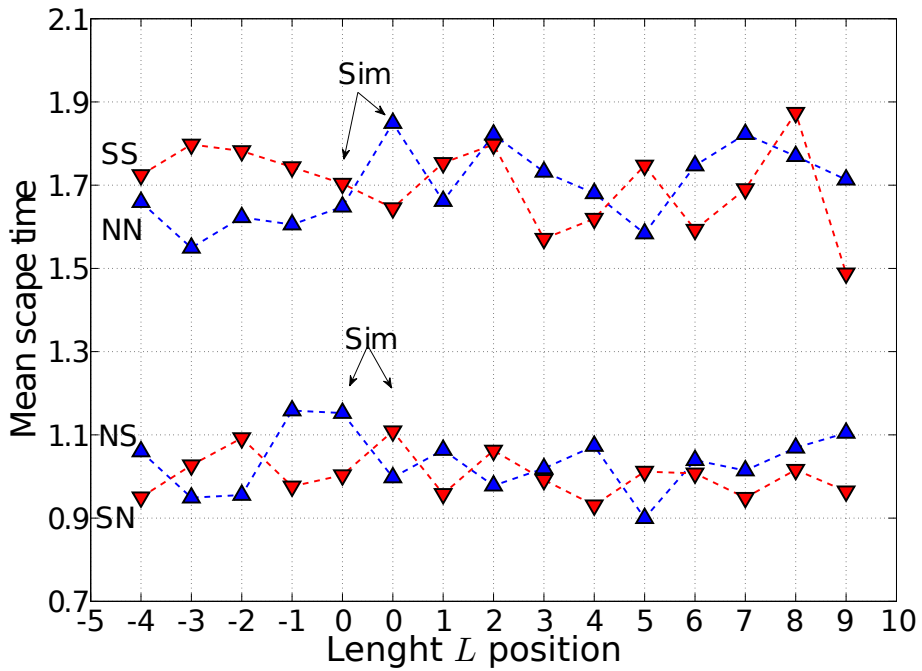


Figure 7.8: Preferential and escape times as a function of the position L_N of the north propeller (the south propeller is moved in such a way that H remains constant). The labels indicate whether the mean residence time for the preferential zone (SS, NN) and for the non-preferential (NS, SN) are computed, depending the asymmetric state where the average flow remains.

7.2 Stochastic behavior

Until now we have characterized how long the spheres stay in each side of the vessel, but in this section we will try to show that these residence times are related with an stochastic behavior. This part of the experiment is done in strong collaboration with the group of the Laboratoire

de Physique from the ENS-Lyon, France. We have analyzed the behavior of two vessels, the cylindrical vessel of Pamplona, and a container with square section that is analyzed in Lyon. The results that we will present here concerns only the experiment run in Pamplona.

In Fig. 7.9.a-d we present the statistical sampling that the sphere explore during its movement along the axial direction for the four diameters used in this experiment. For each set of graphs, we plot the evolution of the axial displacement in a small period of time (72 sec, left panel), then we show a long period (1 hour, middle panel) and finally we show the PDF in function of the axial displacement of the particle (right panel). Where we also split the symmetrical solutions represented in the black (N state) and red (S state) colors. It should be noted that when we differentiate the zones N/S, the particle remain long periods on the larger cell, since in this zone the fluctuations are low compared with the small one.

From this graph we can see how, as we have already presented, the smallest particle (10mm, black) has a dynamical behavior different from the three others. The smallest one jumps continuously between the regions close to both propellers, and a symmetric PDF is recovered. On the other hand, the dynamics is completely dominated by the large scale flow. This last point is very clear for the largest spheres (30 and 40mm), but is more ambiguous for the 20 mm particle (red). Noteworthy that all these dynamics are slower than the characteristic time of the experiment, making them an interesting object of study for the future.

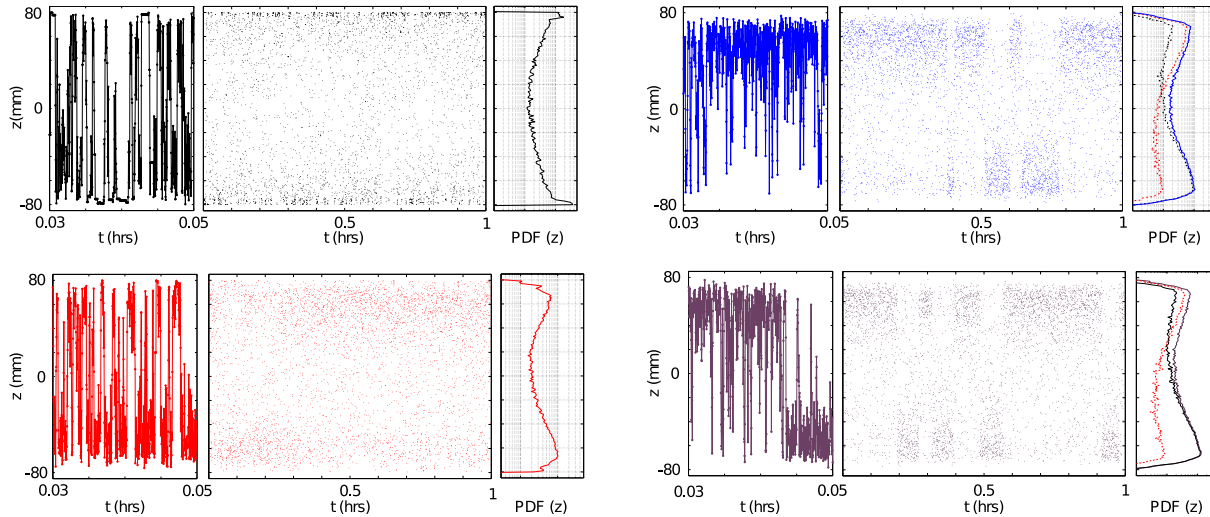


Figure 7.9: Dynamics of the spheres of $D_p = 10\text{mm}$ (black), $D_p = 20\text{mm}$ (red), $D_p = 30\text{mm}$ (blue) and $D_p = 40\text{mm}$ (violet). For each series, we have plotted the dynamics for a small period of time (left panel), for a long period of time (middle panel) and finally the PDF (right panel). The propeller frequency is fixed to $f_{prop} = 3.17\text{Hz}$.

From these graphs we can deduce that the particles explore statistically certain zones of the cylinder with a probability distribution that depends on the particle size but always the preferred regions are located close to the propellers and far from the shear layer. To verify this asseveration, we computed the 2D probability distribution using the projection of the position of the particles in y, z plane (see Fig. 7.10). In this plot we can verify the existence of these preferential zones. The dynamics inside these regions has a behavior close to random, and the same happens for the jumps between both regions. It seems appropriated to describe the problem using a model based

on the existence of potential wells located in the regions close to the propellers. This specific plot has been done with the conjoint computation of the 2D PDF of various experimental runs to improve the statistics.

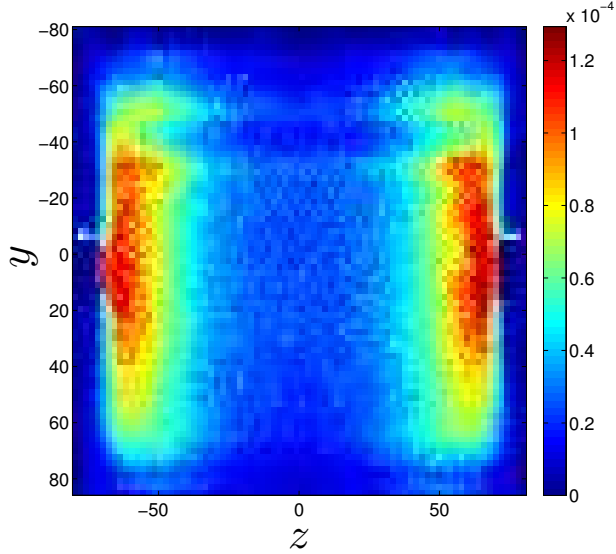


Figure 7.10: 2D PDF of the whole data series of the positions of the particle projected in the y, z plane. The particle used for this sampling was the 20mm at $f_{prop} = 3.17Hz$.

When the computation is done separately for the S and N states, we obtain a different picture (see Fig.7.11). In this situation the region that has a higher probability is the one close to the dominant propeller, as it was expected (case S in Fig.7.11), left; case N in Fig.7.11, right). Also we can see from these figures how the weight of the potential wells are different, and the symmetry between the states. If we combine these two plots, we will recover the one presented in Fig.7.10

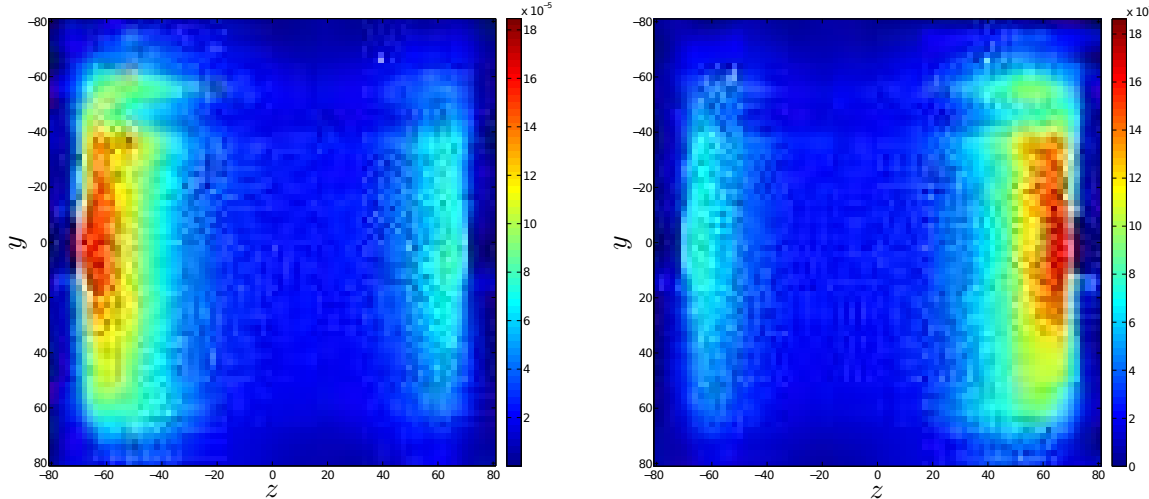


Figure 7.11: 2D PDF of the positions of the particle projected in the y, z plane, when the flow remains in the South (Left) and North (Right) state. Both are measured using particles of 20mm at $f_{prop} = 3.17Hz$.

Finally, we decided to make an spectral analysis of these series. In Fig.7.12, left, we show the power spectra of the axial position where the signature of the reversals is clearly visible (the -2 slope for frequencies below $f \sim 410^{-3}$). But the most interesting part of this graph comes when we normalize the spectra, since a clear slope appears from the injection frequency towards smallest frequencies, and stops one order of magnitude below. Although we have no explanation for this behavior, we have the impression that could be related to a stochastic behavior between two well potentials. Moreover, we have noted that the intermediate zone in this spectrum changes only for the particle of 20mm. We have also tried to test different Re for the same particle and the intermediate slope doesn't changes.

Another important aspect can be observed when we do the same but for the y component (see 7.12, right). There we can identify a well defined peak. This peak corresponds to the azimuthal movement that the particle follows linked to the rotation of the propeller. It is interesting to observe that for the cases of $D_p = 30$ and 40mm , the peak has almost the same rotation frequency of the propeller, however for the case of 20mm the rotation of the particle presents an slower movement.

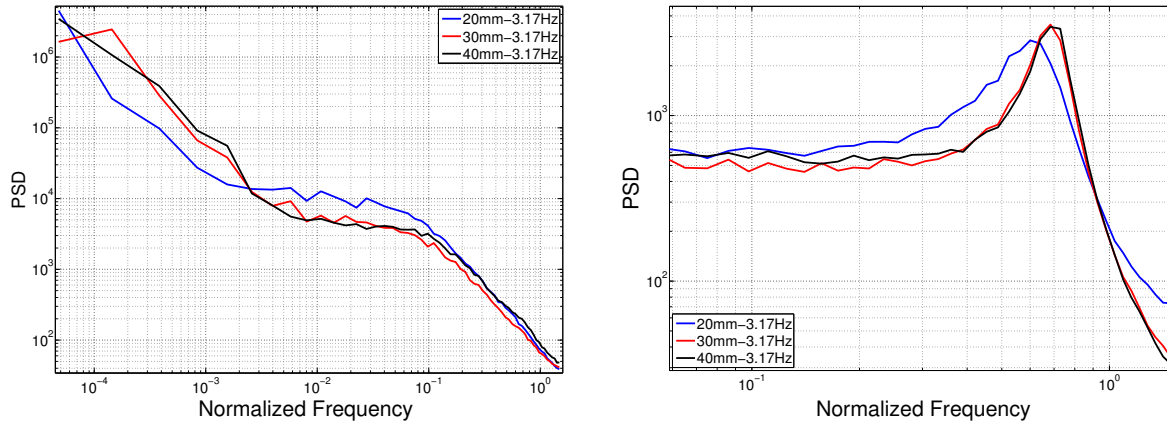


Figure 7.12: Power spectra of the (left) axial position z and (right) vertical position y of different sizes of spheres, for a fixed rotation frequency $f_{N,S} = 3.17\text{Hz}$.

As a result of the collaboration between Pamplona and Lyon, we have built a stochastic model that can reproduce many of the features of the Pamplona and Lyon experiments. This conjoint research has been included in a manuscript that will be sent soon for publication.

Conclusions and Outlook

Conclusions

Turbulent flows have been analyzed during the last century, with the objective of enhancing the understanding of classical physics and improve the actual technology. Although many generic characteristics have been obtained and is surprising how many new features appear in different experimental setups, like the appearance of vortical filaments, coherent structures instabilities, effects of the anisotropy, etc. Here we have presented a cylindrical experimental setup, where a closed flow has shown a rich dynamics in the whole range of frequencies and scales.

For many years, the analysis of turbulent flows has been focused on the fast scales and its characterization, both temporal and spatial. Nevertheless, one of the key points of turbulence is the creation of coherent structures that can live for times hundreds or thousands times bigger than any other temporal scale. This in some way similar to what happen in the atmosphere: the turbulent flows that are created due to convection and Coriolis forces, together with the interaction with the surrounding earth and humidity from the oceans, produce large structures that appear as hurricanes or tornadoes.

This setup has been studied in different configurations (co-rotation, counter-rotation, flat disks, using blades, rings around the cylinder, etc.) all around the world. The present vessel was built in the University of Navarra eight years ago and during this time a large effort has been put to understand the dynamics that appeared in this configuration. The very long time dynamics was obtained in a previous work, here we have presented what was missing to understand and the new results concerning the behaviour of the whole spectra, both for the long scales and for the inertial range.

The different wide range of scales involved in this flow has been analysed for several Reynolds and no difference have been encountered. Even we have done several test using different techniques or methods and the results always present the same scaling values. So these results provide certainty to our measurements, since yield to the same results that have been reported from similar experimental setups.

A mapping of the spatial fluctuation (\mathbf{v}') was reported using two different velocimetry techniques and the same statistical results have been obtained. In these maps we can detect where the large structures appear and also serve as a guide for future measurements.

Following the same approach of the fluctuations maps, we compute the mean flow for the two possible symmetrical solutions that appear in our system identifying the position where the shear layer is situated. Based on the measurements done in this research we conclude that this layer will never stay on the middle of the vessel, even using the most symmetrical configuration possible. This situation is only reached in a statistical sense, when a time average is computed for periods thousands of times bigger than the injection scale. However we realized that if we increase the Re number, we can decrease the time that the flow remains in one state, and so, the period of

time needed to place the average position of the shear layer in the middle is also decreased.

In addition, interesting observations were made, like the stabilization of the shear layer at the middle of the vessel just removing the caps of the cavity. Nevertheless, we still don't have an answer to the question of the origin of this stabilization. However, we thought that the pressure gradients generated by the turbulence, applied torque forces to the vortices and to the conservation of angular momentum are at the origin of the instabilities. Even more interesting, it was already presented that a random forcing of the impellers' forcing with an amplitude of 1% produces a similar result, so the fluctuations of the mean flow are key to stabilize that layer.

We have deeply characterized the spatial and temporal behavior of the VK flow in the inertial range using the classical theory for an homogeneous and isotropic flow. In order to check to what extent our flow follows the Kolmogorov predictions, we have computed the spatial and temporal spectra, and in both cases we recovered the classical exponent $-5/3$ in the inertial range. The anisotropy of the flow has been presented for the large scales, and also we reported the range where the isotropy appears for the small scales. The transition between isotropy and anisotropy is at the beginning of the inertial range, close to the integral scale. These characteristics of turbulent flows were computed using the structure function of the second and third order both in space (the correct approach) and using high resolution time series (using a Taylor hypothesis approach), and both approaches produce the same values, within the error bars. We have parametrized our turbulent flows, through the values of parameters like, Re_λ , L_{int} , etc. These magnitudes allows us to compare this flow with other turbulent flows.

The main result of this work is the identification of a conserved magnitude that is transferred between the different scales through an inverse cascade, and that is at the origin of large vortices observed on the flow. This magnitude is the angular momentum, so the torque that is applied on one side of any of the different slices of the flow is balanced by the torque on the other side of the slice. This behaviour appears only for a system where the impellers have a large inertia and the frequency of the propellers is very stable. Without these features wouldn't be possible to obtain these scales because the fluctuations on the energy injection kill this dynamics.

We can conclude saying that, even in the simplest configuration, the large scales (temporal and spatial) are crucial to understand the dynamics of turbulent flows. These scales are at the origin of the coherent structures. Any flow where there is a collision layer between two fluid circulations, where some magnitude as the angular momentum has to be transferred and where the average flow is negligible and this magnitude must be transported by fluctuations, is susceptible to develop a similar behavior.

Outlook

This work provides an important ingredient to the understanding of turbulent flows, since until now it was a conjecture the existence of a mechanism that can transfer energy backwards in the spectral domain in 3D flows. This novel result could provide more information about how the fluids behave when they are in the turbulent regime and also could open other research lines.

A larger version of this experimental setup is being built and will allow to extend the analysis of this inverse cascade. We will characterize this dynamics to have a better comprehension of the large vortices that appear close to the wall of the cylinder. Since these equatorial vortices have a very complex dynamics, for example, we cannot identify a simple azimuthal wavenumber and

they time-life fluctuates depending on the vortex size, a deeper study is necessary.

Another perspective could be to analyze the “ultimate” regime of the VK flow using flat discs. As we have demonstrated, there is a transfer of torque between the top and bottom plates –using the fluid as a medium of transport. This is similar to the transfer of angular momentum in Taylor-Couette flows in the radial direction and the heat transfer in Rayleigh-Benard convection on the vertical direction. Using flat discs will be possible to quantify the length of the “viscous layer” and recover the scalings for really high Reynolds numbers.

This setup can be easily extended to other rotating configurations. Each one of these setups present different behaviours in the turbulent regime, and it would be interesting to verify if the present dynamics appears in those systems.

Bibliography

- [1] S. Pope. *Turbulent Flows*. Cambridge University Press, Cambridge, England, 2000.
- [2] A.N. Kolmogorov. The local structure of turbulence in incompressible viscous fluid for very large reynolds numbers. *Proc. R. Soc. Lond. A*, 434(1890):9–13, 1991.
- [3] A.N. Kolmogorov. Dissipation of energy in the locally isotropic turbulence. *Proc. R. Soc. Lond. A*, 434(1890):15–17, 1991.
- [4] P.A. Davidson. *Turbulence an introduction for scientists and engineers*. Oxford, 2004.
- [5] A. de la Torre and J.Burguete. Slow dynamics in a turbulent von Kármán swirling flow. *Phys. Rev. Lett.*, 99:054101, 2007.
- [6] Richard W. Johnson. *The Handbook of Fluid Dynamics*. CRC, 1998.
- [7] G.K. Batchelor. *An Introduction to Fluid Dynamics*. Cambridge, 1967.
- [8] G. Thomas Mase and George E. Mase. *Continuum mechanics for engineers*. CRC Press, 1999.
- [9] I.G. Currie. *Fundamental Mechanics of Fluids*. McGraw-Hill, 1993.
- [10] D.J. Tritton. *Physical Fluid Dynamics*. Oxford University Press, 1988.
- [11] P. Holmes, J.L. Lumley, and G. Berkooz. *Turbulence, Coherent Structures, Dynamical Systems and Symmetry*. Cambridge U. Press, 1996.
- [12] U. Frisch. *Turbulence*. Cambridge U. Press, 1995.
- [13] C.R. Doering and J.D. Gibbon. *Applied analysis of the Navier-Stokes equations*. Cambridge U. Press, 1995.
- [14] P.A. Davidson, Y. Kaneda, K. Moffat, and K.R. Sreenivasan. *A Voyage Through Turbulence*. Cambridge U. Press, 2011.
- [15] A. S. Monin and A. M. Yaglom. *Statistical Fluid Mechanics: Mechanics of Turbulence*. The MIT Press, 1971.
- [16] H. Tennekes and J.L. Lumley. *A First Course in Turbulence*. The MIT Press, 1972.
- [17] O. Reynolds. An experimental investigation of the circumstances which determine whether the motion of water shall be direct or sinuous, and of the law of resistance in parallel channels. *The Royal Society*, 174:935–982, 1883.
- [18] N. Rott. Note on the history of the reynolds number. *Annu. Rev. Fluid Mech.*, 22, 1990.

- [19] M. Van Dyke. *An album of fluid motion*, volume 46. Parabolic Press Stanford, 1982.
- [20] M. Samimy, K.S. Breuer, L.G. Leal, and P.H. Steen. *A Gallery of Fluid Motion*. Cambridge University Press, 2003.
- [21] Arkady Tsinober. *An Informal Introduction to Turbulence*. Kluwer Academic, 2004.
- [22] L.F. Richardson. *Weather Prediction by Numerical Process*. Cambridge University Press, 1922.
- [23] G.I. Taylor. Statistical theory of turbulence. *Proc. R. Soc. A.*, 151, 1935.
- [24] G.I. Taylor. The spectrum of turbulence. *Proc. R. Soc. A.*, 164, 1938.
- [25] G.K. Batchelor. Pressure fluctuations in isotropic turbulence. *Camb. Phil. Soc.*, 47:359–374, 1951.
- [26] G.I. Taylor. The mean value of the fluctuations in pressure and pressure gradient in a turbulent fluid. *Proc. Camb. Phil. Soc.*, 32:580–584, 1936.
- [27] J. M. McDonough. Introductory lectures on turbulence physics, mathematics and modeling, 2004.
- [28] A.M Obukhov. Energy distribution in the spectrum of a turbulent flow. *Ser. geogr. geofiz.*, (4-5):453–466, 1941.
- [29] J.-F. Pinton and R. Labb  . Correction to the Taylor hypothesis in swirling flows. *J. Phys. II France*, 4:1461–1468, 1994.
- [30] G.L. Brown and A. Roshko. On density effects and large structure in turbulent mixing layers. *J. Fluid Mech.*, 64:775–816, 1974.
- [31] D.B. Blum, G.P. Bewley, E. Bodenschatz, M. Gibert, A. Gyldason, L. Mydlarski, G.A. Voth, H. Xu, and P.K. Yeung. Signatures of non-universal large scales in conditional structure functions from various turbulent flows. *New J. Phys.*, 13, 2011.
- [32] J. Fontane, L. Joly, and J.N. Reinaud. Fractal Kelvin-Helmholtz breakups. *Phys. Fluids*, 20, 2008.
- [33] Robert H. Kraichnan. Inertial ranges in two-dimensional turbulence. *Phys. Fluids*, 10(7):1417, 1967.
- [34] U. Frisch and P.-L. Sulem. Numerical simulation of the inverse cascade in two-dimensional turbulence. *Physc. Fluids*, 27(8), 1984.
- [35] C.V. Tran and J.C. Bowman. Robustness of the inverse cascade in two-dimensional turbulence. *Phys. Rev. E*, 69(3), 2004.
- [36] C.-H. Bruneau, P. Fisher, and H. Kellay. The structures responsible for the inverse energy and the forward enstrophy cascades in two-dimensional turbulence. *EPL*, 78(34002), 2007.
- [37] J. Paret and P. Tabeling. Experimental observation of the two-dimensional inverse energy cascade. *Phys. Rev. Lett.*, 79(21), 1997.

- [38] P. Tabeling. Two-dimensional turbulence: a physicist approach. *Physics Reports*, 362:1–62, 2002.
- [39] J Salort and et al. Turbulent velocity spectra in superfluid flows. *Phys Fluids*, 22, 2010.
- [40] V E Zakharov, V S L'vov, and G Falkovich. *Kolmogorov Spectra of Turbulence I - Wave Turbulence*. Springer-Verlag, Berlin, 1992.
- [41] V E Zakharov, F Dias, and A Pushkarev. One-dimensional wave turbulence. *Physics Reports*, 398:1–65, 2004.
- [42] L. Deike, C. Laroche, and E. Falcon. Experimental study of the inverse cascade in gravity wave turbulence. *EPL*, 2011.
- [43] D. Byrne, H. Xia, and M. Shats. Robust inverse energy cascade and turbulence structure in three-dimensional layers of fluid. *Phys. Fluids*, 23, 2011.
- [44] A Hasegawa, Y Kodama, and K Watanabe. Self organization in korteweg- de vries turbulence. *Phys Rev Lett*, 47:1525, 1981.
- [45] E Levich and E Tzvetkov. Helical inverse cascade in three dimensional turbulence as a fundamental dominant mechanism in mesoscale atmospheric phenomena. *Phys Reports*, 128:1–37, 1985.
- [46] E Levich and A Tsinober. On the role of helical structures in three-dimensional turbulent flow. *Phys Lett*, 93A:293, 1983.
- [47] H.K. Moffatt. *Magnetic Field Generation in Electrically Conductive Fluids*. Cambridge U. Press, 1978.
- [48] M. López-Caballero and J. Burguete. Inverse cascades sustained by the transfer rate of angular momentum in a 3d turbulent flow. *Phys. Rev. Lett.*, 110(12), 2013.
- [49] T. von Kármán. On laminar and turbulent friction. *NACA*, (1092), 1946.
- [50] P.J. Zandbergen and D. Dijkstra. von Kármán swirling flows. *Ann. Rev. Fluid Mech.*, 1987.
- [51] D. Dijkstra and G.J.F. van Heijst. The flow between two finite rotating disks enclosed by a cylinder. *J. Fluid Mech.*, 128:123–154, 1983.
- [52] S. Douady, Y. Couder, and M.E. Brachet. Direct observation of the intermittency of intense vorticity filaments in turbulence. *Phys. Rev. Lett.*, 67(8), 1991.
- [53] R. Labb  , J.-F. Pinton, and S. Fauve. Study of the von K  rm  n flow between coaxial corotating disks. *Phys. Fluids*, 8:914–922, 1996.
- [54] M.L. Dudley and R.W. James. Time-dependent kinematic dynamos with stationary flows. *Proc. R. Soc. Lond. A*, 425:407–429, 1989.
- [55] L. Mari   and F. Daviaud. Experimental measurements of the scale-by-scale momentum transport budget in a turbulent shear flow. *Phys. Fluids*, 16(2):457, 2004.

- [56] F. Ravelet, A. Chiffaudel, and F. Daviaud. Supercritical transition to turbulence in an inertially driven von Kármán closed flow. *J. Fluid Mech.*, 601:339–364, 2008.
- [57] N. Mordant, J.-F. Pinton, and F. Chilla. Characterization of turbulence in a closed flow. *J. Phys. II*, 7:1729–1742, 1997.
- [58] J.-F. Pinton, F. Chilla, and N. Mordant. Intermittency in the closed flow between coaxial corotating disks. *Eur. J. Mech. B/Fluids*, 17(4), 1998.
- [59] S.T. Bramwell, P.C. Holdsworth, and J.-F. Pinton. Universality of rare fluctuations in turbulence and critical phenomena. *Nature*, 396:552–554, 1998.
- [60] J.-F. Pinton, P.C.W. Holdsworth, and R. Labbé. Power fluctuations in a closed turbulent shear flow. *Phys. Rev. E*, 60(3), 1999.
- [61] F. Ravelet, A. Chiffaudel, and F. Daviaud. Toward an experimental von Kármán dynamo: Numerical studies for an optimized design. *Phys. Fluids*, 17, 2005.
- [62] L. Marie. *Transport de moment cinétique et de champ magnétique par un écoulement tourbillonnaire turbulent: influence de la rotation*. PhD thesis, Université Paris, 2003.
- [63] M. Bourgoin, N.T. Ouellette, H. Xu, J. Berg, and E. Bodenschatz. The role of pair dispersion in turbulent flow. *Science*, 311:835–838, 2006.
- [64] R. Monchaux. *Mécanique statistique et effect dynamo dans un écoulement de von Kármán turbulent*. PhD thesis, Université Paris Diderot, 2007.
- [65] P.-P. Cortet, A. Chiffaudel, F. Daviaud, and B. Dubrulle. Experimental evidence of a phase transition in a closed turbulent flow. *Phys. Rev. Lett.*, 105(214501), 2010.
- [66] E. Herbert, F. Daviaud, B. Dubrulle, S. Nazarenko, and A. Naso. Dual non-Kolmogorov cascades in a von Kármán flow. *EPL*, 100, 2012.
- [67] R. Volk, E. Calzavarini, E. Leveque, and J.-F. Pinton. Dynamics of inertial particles in a turbulent von Kármán flow. *J. Fluid Mech.*, 668:223–235, 2010.
- [68] R. Zimmermann, Y. Gasteuil, M. Bourgoin, R. Volk, A. Pumir, and J.-F. Pinton. Rotational intermittency and turbulence induced lift experienced by large particles in a turbulent flow. *Phys. Rev. Lett.*, (106), 2011.
- [69] F. Toschi and E. Bodenschatz. Lagrangian properties of particles in turbulence. *Annu. Rev. Fluid Mech.*, 41:375–404, 2009.
- [70] H. Xu, A. Pumir, and E. Bodenschatz. The pirouette effect in turbulent flows. *Nature Phys.*, (7):709–712, 2011.
- [71] F. Ravelet. *Bifurcations globales hydrodynamiques et magnétohydrodynamiques dans un écoulement de von Kármán turbulent*. PhD thesis, École doctorale de l'école Polytechnique, 2005.
- [72] J. Burguete and A. de la Torre. Hysteresis and vortices dynamics in a turbulent flow. *IJBC*, 19(8):2695–2703, 2009.

- [73] P.-P. Cortet, E. Herbert, A. Chiffaudel, F. Daviaud, B. Dubrulle, and V. Padilla. Susceptibility divergence, phase transition and multistability of a highly turbulent closed flow. *J. Stat. Mech.*, 2011.
- [74] H.-E. Albrecht, M. Borys, N. Damaschke, and C. Tropea. *Laser Doppler and Phase Doppler Measurement Techniques*. Springer, 2002.
- [75] Z. Zhang. *LDA Application Methods*. Springer, 2010.
- [76] D.K. McLaughlin and W.G. Tiederman. Biasing correction for individual realization of laser anemometer measurements in turbulent flows. *Phys. Fluids*, 16(12), 1973.
- [77] R.J. Adrian and C.S. Yao. Power spectra of fluid velocities measured by laser doppler velocimetry. *Exp. in Fluids*, 5:17–28, 1987.
- [78] R.J. Adrian. Twenty years of particle image velocimetry. *Exp. in Fluids*, 39:159–169, 2005.
- [79] M. Raffel, C.E. Willert, S.T. Wereley, and J. Kompenhans. *Particle Image Velocimetry*. Springer, 1998.
- [80] N.M. Qureshi, M. Bourgoin, C. Baudet, A. Cartellier, and Y. Gagne. Turbulent transport of material particles: An experimental study of finite size effects. *Phys. Rev. Lett.*, 99(18):184502, 2007.
- [81] N.M. Qureshi, U. Arrieta, C. Baudet, A. Cartellier, Y. Gagne, and M. Bourgoin. Acceleration statistics of inertial particles in turbulent flow. *EPJ B*, 66:531–536, 2008.
- [82] L. Fiabane, R. Zimmermann, R. Volk, J.-F. Pinton, and M. Bourgoin. On the clustering of finite-size particles in turbulence. *Phys. Rev. E*, 86(035301(R)), 2012.
- [83] C. Poelma, J. Westerweel, and G. Ooms. Turbulence statistics from optical whole-field measurements in particle-laden turbulence. *Experiments in Fluids*, 40:347–363, 2006.
- [84] J.M. Foucaut, J Carlier, and M Stanislas. Piv optimization for the study of turbulent flow using spectral analysis. *Meas. Sci. Technol.*, 15, 2004.
- [85] A. de la Torre. *Sobre los efectos de las escalas lentas en la magnetohidrodinámica de un flujo de von Kármán*. PhD thesis, Universidad de Navarra, 2009.
- [86] A.A. Townsend. *The structure of turbulent shear flow*. Cambridge University Pres, 1976.
- [87] R. Labb  , J.-F. Pinton, and S. Fauve. Power fluctuations in turbulent swirling flows. *J. Phys. II France*, 6:1099–1110, 1996.
- [88] Fr  d  ric Moisy. pivmat. <http://www.fast.u-psud.fr/pivmat/>.
- [89] Q. Nie and S. Tanveer. A note on third-order structure functions in turbulence. *Proc. R. Soc. Lond. A*, 455:1615–1635, 1997.
- [90] C. Poelma, J. Westerweel, and G. Ooms. Particle-fluid interactions in grid-generated turbulence. *J. Fluid Mech.*, 589:315–351, 2007.

- [91] N. Ouellette, H. Xu, M. Bourgoin, and E Bodenschatz. Small-scale anisotropy in lagrangian turbulence. *New Journal of Physics*, 8, 2006.
- [92] K. R. Sreenivasan. On the universality of the Kolmogorov constant. *Phys. Fluids*, 7(2778), 1995.
- [93] G. Zocchi, P. Tabeling, J. Maurer, and H. Willaime. Measurement of the scaling of the dissipation at high reynolds numbers. *Phys. Rev. E*, (5):3693–3700, 1994.
- [94] J.K. Eaton and J.R. Fessler. Preferential concentration of particles by turbulence. *Int. J. Multiphase Flow*, 20:169–209, 1994.
- [95] O. Cadot, Y. Couder, A. Daerr, S. Douady, and A. Tsinober. Energy injection in closed turbulent floes: Stirring through boundary layers versus inertial stirring. *Phys. Rev. E*, 56, 1997.
- [96] L.D. Landau and E.M. Lifshitz. *Fluid Mechanics*. Pergamon Press, 1987.

Summary

In this experimental work, we have presented the causes of the slow dynamics (large scales) that appears in a fully developed turbulent flow. The appearance of this type of phenomena is very common in the atmosphere and they are often viewed as large vortices such as hurricanes, tornadoes, waves in the clouds, vortices in the rear of the aircraft, etc. Also we have included a partial rebuild of the large vortices that appear inside of the experimental system, to understand in a better way their behavior. As well we have added a complete characterization of the various parameters of the turbulence, which will serve to compare this device with current experimental systems.

The main merit of this work is that it has been proved that the angular momentum of the fluid is a conserved quantity and if you inject enough energy, you can even develop a transfer mechanism of this magnitude. This was reflected in the appearance of an inverse cascade in the spatial and temporal domain of the Fourier space, it is important to note that although it had been proposed previously, it has never been proved. In order to explain the power law that appears, we have included a dimensional analysis which predicts the exponents found in this investigation, giving it strength to this study.

We hope that this work could help to understand a little better how fluids behave, as we believe that the coupling between small scales and large scales, is key to the complete understanding of turbulence.

Resumen

En este trabajo experimental, se ha intentado explicar las causas de por que aparecen dinámicas lentas (escalas grandes) en un flujo turbulento totalmente desarrollado. La aparición de este tipo de fenómenos es muy común en la atmósfera y suelen visualizarse en forma de grandes vórtices como huracanes, tornados, olas en las nubes, vórtices en la parte trasera de los aviones, etc. También se ha incluido una reconstrucción parcial de los grandes vórtices que aparecen dentro del sistema experimental, para tratar de comprender de una mejor manera su comportamiento. Igualmente se incluye una completa caracterización de los distintos parámetros de la turbulencia, que servirán para poder comparar este dispositivo con sistemas experimentales actuales.

El principal merito de este trabajo es que se ha logrado comprobar que el momento angular del fluido es una magnitud que se conserva y si se inyecta la suficiente energía, puede incluso llegar a desarrollar un mecanismo no intuitivo de transferencia de esta magnitud. Esto se vio reflejado en la aparición de una cascada inversa en el dominio espacial y temporal del espacio de Fourier. Es importante decir que aunque anteriormente se había propuesto, nunca se había podido comprobar. Para poder explicar esta ley de potencias que aparece, se ha incluido un análisis dimensional el cual predice los exponentes encontrados en esta investigación, dándole solidez a este estudio.

Esperamos que este trabajo pueda ayudar a comprender un poco mejor la manera en que los fluidos se comportan, ya que creemos que el acoplamiento entre las pequeñas escalas y las grandes escalas, podrá dar lugar al completo entendimiento de la turbulencia.

